Measurement of Time Dependent B_d^0 $\bar{B}_d^0$ Mixing Parameter Using Opposite Side Lepton and $D^{*\pm}$ Meson in $p\bar{p}$ Collisions at $\sqrt{s} = 1.8\ TeV$.

by

Stephan Christopher Vandenbrink

B.S., University of Indonesia, 1988
M.S., University of Pittsburgh, 1991

Submitted to the Graduate Faculty
of the Department of Physics and Astronomy
in partial fulfillment of
the requirements for the degree of
Doctor
of
Philosophy

University of Pittsburgh
January 13, 1998

University of Pittsburgh
Faculty of Arts and Sciences

This thesis was presented and defended by
Stephan Christopher Vandenbrink
on October 20, 1997

and approved by

Dr. Eugene Engels, Dept. of Physics and Astronomy

Dr. Paul Shepard, Dept. of Physics and Astronomy

Dr. Raymond Willey, Dept. of Physics and Astronomy

Dr. Frank Tabakin, Dept. of Physics and Astronomy

Dr. Joel Falk, Dept. of Electrical Engineering

Measurement of Time Dependent $B_d^0\,\bar{B}_d^0$ Mixing Parameter Using Opposite Side Lepton and D* Meson in $p\bar{p}$ Collisions at $\sqrt{s} = 1.8\ TeV$.

Stephan Christopher Vandenbrink, Ph.D.
University of Pittsburgh

This thesis presents the results from the investigation of time dependent $B_d^0\,\bar{B}_d^0$ mixing in $B \to lepton\ X$, $B_d^0 \to D^{*-}\ X$, $D^{*-} \to \bar{D}^0\ \pi^-$, $\bar{D}^0 \to K^+\ \pi^-$ channel in $p\bar{p}$ collisions at $\sqrt{s} = 1.8\ TeV$ using 110 pb^{-1} data collected with the CDF detector at the Fermilab Tevatron Collider. The $\bar{D}^0$ vertex is reconstructed. The B_d^0 decay length is estimated using the distance from the primary vertex to the measured position of the D^0 vertex. The B^0 momentum is estimated using the D^0 momentum and a kinematic correction factor from Monte Carlo. With the dilution floating, $\Delta M_d = 0.55 \pm^{0.15}_{0.16}\ (stat) \pm 0.06\ (syst)\ ps^{-1}$ is measured.

ACKNOWLEDGEMENTS

Thank God and His power of Goodness that I have succesfully finished this thesis. My dearest mother, father and sister, thank you, again and again, for your unconditional love, support and encouragement throughout my academic career. Dearest Jeff and little Keri, thank you for also being there when I needed my family the most. My spiritual parents, Tante Elizabeth and Oom Daniel Hadinata, I thank you so much for introducing me to your powerful Church and for your telephone prayers. Aunt Lily, Aunt Beng, my late Oom Frans, my cousin Henny, Patricia, Tante Mien, Ronny and all other relatives many thanks for your moral support and help I received during my student days.

I would also like to use this opportunity to express my sincerest gratitude to my two dear advisors Gene Engels and Paul Shepard for their kindest support and guidance during the period of my research assistantship in their group. Gene, mein Kaffee trinkender Freund, danke schön for the many philosophical conversations and unsolicited advices. Paul, thanks for the memorable story about your evangelism at 30,000 feet with Gene. I really enjoy working in your group. I think it is the best and coolest group in the whole physics department.

I still remember the day when Joe Boudreau, a new assistant professor then, walked confidently into the ground floor lab of Allen Hall where I was working with the newly bought Multi Channel Analyzer. He handed me an ALEPH paper on B Mixing and encouraged me to consider the possibility of choosing B Mixing as my thesis project. I thank him very much for attracting my attention to this very interesting phenomenon and for supporting me through this analysis with his keen insights and discussions.

Manfred Paulini, in his capacity as a B Mixing convener provided technical and physics analysis support to many graduate students in CDF including myself. For his expert help, I express my special thanks. Furthermore, I would also like to thank the whole B physics group, including Regina Demina, Joe Kroll, Fritz Dejongh, Marjorie Shapiro, Fumi Ukegawa and Colin Gay for sharing their professional opinions and expertise with me.

My undergraduate physics professors Dr.Na Peng Bo, Dr.Darmadi Kusno, Dr.Muliawati Siswanto, Dr.Parangtopo and Dr.B.E.F.da Silva; I thank them

so much for sharing their knowledge with me. I especially thank Pater Na for attracting my interest to the field of experimental physics and Dr.Darmadi for attracting my interest to the field of particle physics.

All the Physics and Astronomy Departement staff, thanks a lot for all you have done for me. Joan Lucas, thank you very much for all the help the Office of International Services provided for me. My many good friends, too many to mention here, at Fermilab, in Pittsburgh and in many other places all over the world thank you for sharing some moments of your lives doing things together with me.

I would like to specially thank the Indonesian Consul General in Chicago, Mr.Soejono Soerjoatmodjo and his wife for inviting me to the many celebrational banquets in their residence. My many thanks to the Vice Consul Mr.Utomo and all the Consulate staff for their help with my passport related issues.

Last but not the least, I would like to greatly thank my thesis committee members for their cooperation in working out the meeting time and for their patience in listening to my presentation.

TABLE OF CONTENTS

LIST OF TABLES

LIST OF FIGURES

CHAPTER 1.

Introduction

A. The fundamental structure of matter

The limited capacity of the human brain requires us to simplify the intractable complexity of nature and the universe by introducing models that can describe the world around us satisfactorily to the human mind. It is common knowledge that small simple quantities of materials are always easier to handle than large complicated ones. Naturally, the most successful models for us are the ones that attempt to explain nature by dividing objects into smaller and smaller parts, in the hope of dealing with simpler and simpler entities. This led ancient philosophers to the concept of the basic building block of matter or fundamental particle. Even among the unsatisfactory models, like the ancient Chinese belief that the physical world consists of water, fire, wood, iron and soil, there is still an element of constituency.

In our daily life, we observe that material exists in solid, liquid and gaseous forms. Ice, water, and water vapor are different manifestations of the same large clusters of molecules each with the same chemical formula H_2O. Each water molecule itself consists of three atoms: two hydrogen atoms and one oxygen atom held together by chemical bonds originating from the residual electromagnetic forces between the atoms. In turn, an atom consists of a positively charged heavy nucleus surrounded by negatively charged electrons. The heavy nucleus of an atom is composed of nucleons which are of two types: the positively charged proton and the neutral neutron. In the last 3 decades it has become increasingly clear that proton, neutron and other hadronic particles are by no means the ultimate building blocks of matter, instead they are composed of assemblies of objects of nearly point-like dimensions called 'quarks', bound together by

the 'strong' nuclear force. A series of experimental results has established the existence of subnuclear particles called quarks and leptons.

The structure of matter can be studied using a microscope only down to a certain scale. The result is limited by the wavelength of the light used. We cannot see any structures of dimensions less than one wavelength of the probing light. The shorter the wavelength, which means the higher the frequency, the smaller the scale we can probe. High frequency implies high energy. This is why we need high energy to probe short distances. The electron microscope which employs relatively high-energy electrons can be used as the probe for structures which can be as small as one large molecule. The corresponding De Broglie wavelength $\lambda = h/p$ is short enough to study molecular level structures. To explore deep into the sub-nuclear and sub-nucleonic structures of matter, extremely high-energy probes, usually electrons or protons, are required.

B. High Energy Physics

Particle physicists use huge particle accelerators like the Tevatron at Fermi National Accelerator Lab (Fermilab) in Batavia, Illinois, to produce these extremely high-energy particles. Another useful feature of high-energy particle probes besides access to ultra small structures is that they enable the production of new particles. Higher energy accelerators make possible the production of heavier and rarer particles. Some of the most interesting aspects of particle physics are the rules which regulate such production processes. We must understand which properties must be conserved and what new features can appear. Fermilab Tevatron, which is the most powerful accelerator on earth today, accelerates protons and antiprotons in a giant underground ring of four mile circumference. Large quadrupole magnets located at specific points around the ring focus the counter-rotating proton and antiproton beams into collision. When a proton and an antiproton collide at a speed close to that of light, the collision produces a tiny fireball of pure energy as intense as that during the big bang, when the universe was a trillionth of a second old. Some of the energy is converted into matter, according to Einstein's famous equation, $E = mc^2$, giving showers of particles that may unlock the secret concerning the laws and origin

of the universe. In the fixed target mode, the proton beam is extracted and sent down the fixed target beamline to the experimental areas to be slammed into the target material.

Two hundred and fifty thousand times a second, colliding protons and antiprotons create showers of secondary particles which include electrons, muons, neutrinos, B mesons and W bosons, etc. The collisions happen inside each of the two giant collider detectors which are positioned at different locations around the accelerator ring. The detectors are designed to recognize and record the secondary particles from the collisions. By analyzing the stored data from the detectors, high energy physicists make discoveries about the fundamental nature of matter and energy. Experimenters on CDF (the Collider Detector at Fermilab) announced the first evidence for the observation of the top quark on April 26, 1994. On March 2, 1995, experimenters at both CDF and DZero (the second detector) announced the discovery of the top quark. This very important historical event was welcomed with great joy and enthusiasm by physicists around the world, especially by those who support the Standard Model theory.

C. The history of Mixing

The mixing phenomenon between particle and antiparticle was first predicted for the $K^0\,\bar{K}^0$ system in 1955 [5] and observed in 1956 [6]. Since weak interactions (WI) need not conserve the flavor quantum number, transitions between $K^0 = (\bar{s}\,d)$ and $\bar{K}^0 = (\bar{d}\,s)$ with opposite strangeness[1] are permitted. K^0 and $\bar{K}^0$ are not the mass eigenstates; they do not have definite masses and definite lifetimes since WI do not conserve strangeness. Their linear combinations K_S^0 and K_L^0 are associated with particles of definite and distinct mass M_S and M_L and mean lifetimes γ_S^{-1} and γ_L^{-1}. The mass difference between these states ΔM results in a time-dependent phase difference between the K_S^0 and K_L^0 wave functions and a consequent periodic variation of the K^0 and $\bar{K}^0$ components. Thus the K^0 and $\bar{K}^0$ oscillations are observed with a period given by $2\pi/\Delta M$. The short-lived K_S^0 only decays significantly to $\pi^+\pi^-$ and $\pi^0\pi^0$, each with CP eigenvalue equal to $+1$. The K_L^0 particle decays into many modes including

[1] $S = +1$ and $S = -1$

$\pi^+\pi^-\pi^0$, all of which are eigenstates of CP with eigenvalue equal to -1. If CP invariance were valid, K_S^0 and K_L^0 would be eigenstates of CP with eigenvalues +1 and -1 respectively. Choosing a phase of 1 we have :

$$CP \mid K^0 > \;=\; - \mid \bar{K^0} > \tag{1-1}$$

$$CP \mid \bar{K^0} > \;=\; - \mid K^0 > \tag{1-2}$$

and thus the following linear combinations are eigeinstates of CP.

$$\mid K_1^0 >= \frac{1}{\sqrt{2}}[\mid K^0 > + \mid \bar{K^0} >] \;\; ; \;\; CP = -1 \tag{1-3}$$

$$\mid K_2^0 >= \frac{1}{\sqrt{2}}[\mid K^0 > - \mid \bar{K^0} >] \;\; ; \;\; CP = +1 \tag{1-4}$$

CP invariance would imply that $\mid K_S^0 >= \mid K_2^0 >$ and $\mid K_L^0 >= \mid K_1^0 >$. In 1964, Cronin and Fitch observed that there is a small finite probability for the decay

$$K_L^0 \rightarrow \;\; \pi^+\pi^- \tag{1-5}$$

where the final state has CP=+1. The branching ratio of this decay is small.

$$\Gamma(K_L^0 \rightarrow \;\; \pi^+\pi^-)/\Gamma(K_L^0 \rightarrow \;\; all) = 0.002$$

This means that we can't identify $\mid K_S^0 >$ with $\mid K_2^0 >$ or $\mid K_L^0 >$ with $\mid K_1^0 >$. Instead we must write

$$\mid K_L^0 > \;=\; \frac{1}{\sqrt{1+ \mid \epsilon_1 \mid^2}}(\mid K_1^0 > + \; \epsilon_1 \mid K_2^0 >) \tag{1-6}$$

$$\mid K_S^0 > \;=\; \frac{1}{\sqrt{1+ \mid \epsilon_2 \mid^2}}(\mid K_2^0 > + \; \epsilon_2 \mid K_1^0 >) \tag{1-7}$$

where ϵ_1 and ϵ_2 are small complex numbers [7].

Ignoring CP violation, we assume that $\mid K^0 >$ is the state at $t = 0$. The wave function is thus :

$$\begin{aligned} \mid \psi(0) > \;&=\; \mid K^0 > \\ &=\; \frac{1}{\sqrt{2}}[\mid K_S^0 > + \mid K_L^0 >] \end{aligned} \tag{1-8}$$

Downstream of the kaon beam, we would have a wave function at time t,

$$\mid \psi(t) > \;=\; \frac{1}{\sqrt{2}}[\mid K_S^0 > e^{-\lambda_S t} + \mid K_L^0 > e^{-\lambda_L t}] \tag{1-9}$$

where t is the time interval between production and decay in the kaon rest frame and is given by

$$t = \frac{d}{\beta\gamma}. \tag{1-10}$$

β is the velocity of the particle and $\gamma = 1/\sqrt{1-\beta^2}$. The distance between production and decay is given by d. The decay constants are λ_S and λ_L, given by the expressions

$$\lambda_S = \frac{1}{2}\gamma_S + im_S \tag{1-11}$$

and

$$\lambda_L = \frac{1}{2}\gamma_L + im_L. \tag{1-12}$$

The fraction of K^0 in the beam at time t is

$$\begin{aligned} I(K^0) &= |< K^0 \mid \psi(t) >|^2 \\ &= \frac{1}{4}[e^{-\gamma_S t} + e^{-\gamma_L t} + 2e^{-(\gamma_S+\gamma_L)t/2}\cos\Delta m t] \end{aligned} \tag{1-13}$$

where $\Delta m = m_L - m_S$. The fraction of $\bar{K}^0$ is

$$\begin{aligned} I(\bar{K}^0) &= |< \bar{K}^0 \mid \psi(t) >|^2 \\ &= \frac{1}{4}[e^{-\gamma_S t} + e^{-\gamma_L t} - 2e^{-(\gamma_S+\gamma_L)t/2}\cos\Delta m t]. \end{aligned} \tag{1-14}$$

The quantity defined as the beam strangeness,

$$< S >= \frac{I(K^0) - I(\bar{K}^0)}{I(K^0) + I(\bar{K}^0)} \tag{1-15}$$

oscillates with a frequency $\Delta m/2\pi$.

Since we have other quark flavors, it is natural to expect the possibility of oscillations in other neutral meson systems like $D^0\bar{D}^0$, $B^0\bar{B}^0$ and $B_s\bar{B}_s$. It is easy to observe mixing in the K^0 system since the lifetime of the particle is comparable to the oscillation period. D^0 meson decay is Cabibbo favored, thus it has a short lifetime. Mixing between the D^0 and $\bar{D}^0$ is expected to be very small because of the close cancellation of the s and d quark masses. The degree

of mixing can be expressed as the probability that a particle oscillates into its antiparticle relative to the probability that it remains as itself :

$$r = \frac{Prob(B^0 \to \bar{B}^0)}{Prob(B^0 \to B^0)} = \frac{x^2}{2+x^2} \tag{1-16}$$

$$x \equiv \frac{\Delta M}{\Gamma} \tag{1-17}$$

where CP conservation and $\Delta\Gamma \ll \Delta M$ have been assumed. $\Delta\Gamma$ is the difference between the decay widths and ΔM is the mass difference of the CP eigenstates of the mesons. The x values for kaon, D-meson[8] and B-meson[9] are given below.

$$\begin{aligned} \frac{\Delta M_K}{\Gamma_K} &= 1.0 \\ \frac{\Delta M_D}{\Gamma_D} &= 1.6 \times 10^{-5} \\ \frac{\Delta M_{B^0}}{\Gamma_{B^0}} &= 0.71 \end{aligned}$$

D. $B\bar{B}$ Mixing

B^0 Mixing is described in the same way as the K^0 system. The $B^0\bar{B}^0$ system is described by the Hamiltonian matrix H.

$$H \begin{pmatrix} B^0 \\ \bar{B}^0 \end{pmatrix} = \begin{pmatrix} M - \frac{1}{2}i\Gamma & M_{12} - \frac{1}{2}i\Gamma_{12} \\ M_{12}^\star - \frac{1}{2}i\Gamma_{12}^\star & M - \frac{1}{2}i\Gamma \end{pmatrix} \begin{pmatrix} B^0 \\ \bar{B}^0 \end{pmatrix} \tag{1-18}$$

The diagonal terms describe the decay of the neutral B mesons. M is the mass and Γ is the decay width of the flavor eigenstates B^0 and $\bar{B}^0$. The off-diagonal terms describe the $B^0\bar{B}^0$ transition through the second order WI. M_{12} corresponds to virtual $B^0\bar{B}^0$ transitions while Γ_{12} describes real transitions due to decay modes which are common to B^0 and $\bar{B}^0$, such as $B^0, \bar{B}^0 \to u\bar{d}d\bar{u}, u\bar{d}d\bar{c}$ or $c\bar{d}d\bar{c}$. The term Γ_{12} in the $B^0\bar{B}^0$ system can be neglected because these common decay modes are Cabibbo supressed.

According to the Standard Model, $B^0\bar{B}^0$ transitions occur through a second order WI described by the box diagrams[10]. These diagrams involve the dominant $t \to d$ quark transition, thus the mixing parameters are sensitive to

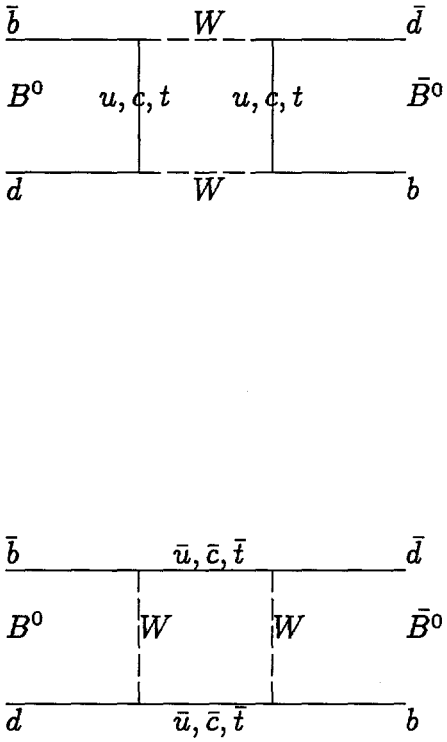

Figure 1-1. Second order WI box diagrams for $B^0\bar{B}^0$ transitions. $B^0 = (d\bar{b})$ and $\bar{B}^0 = (\bar{d}b)$.

the Cabibbo-Kobayashi-Maskawa (CKM) mixing matrix element V_{td} which at present is difficult to access experimentally in other ways. The CKM matrix describes weak couplings between quarks of different flavors. Using Wolfenstein's parametization[11], the CKM matrix can be rewritten as follows :

$$V = \begin{bmatrix} V_{ud} & V_{us} & V_{ub} \\ V_{cd} & V_{cs} & V_{cb} \\ V_{td} & V_{ts} & V_{tb} \end{bmatrix} \tag{1-19}$$

$$= \begin{bmatrix} 1-\frac{\lambda^2}{2} & \lambda & A\lambda^3(\rho - i\rho) \\ -\lambda & 1-\frac{\lambda^2}{2} & A\lambda^2 \\ A\lambda^3(\rho - i\rho) & -A\lambda^2 & 1 \end{bmatrix}$$

Diagonalization of the Hamiltonian matrix in Equation 1-18 results in the CP eigenstates B_1 and B_2 which are linear combinations of the flavor eigenstates. Neglecting CP violation we get :

$$\mid B_1 > = \frac{1}{\sqrt{2}} \left[\mid B^0 > + \mid \bar{B}^0 > \right] \tag{1-20}$$

$$\mid B_2 > = \frac{1}{\sqrt{2}} \left[\mid B^0 > - \mid \bar{B}^0 > \right] \tag{1-21}$$

These two states have masses $M_{1,2}$ and width $\Gamma_{1,2}$:

$$M_{1,2} = M \pm \frac{\Delta M}{2} \tag{1-22}$$

$$\Gamma_{1,2} = \Gamma \pm \frac{\Delta \Gamma}{2} \tag{1-23}$$

$\mid B_1 >$ and $\mid B_2 >$ are both the CP eigenstates and $M - \frac{1}{2}i\Gamma$ eigenstates :

$$CP \mid B_1 > = - \mid B_1 > \tag{1-24}$$

$$CP \mid B_2 > = + \mid B_2 > \tag{1-25}$$

since by definition

$$CP \mid B^0 > = - \mid B^0 > \tag{1-26}$$

The mass difference between the two mass eigenstates :

$$\Delta M = M_2 - M_1 \tag{1-27}$$

gives a measure of the oscillation frequency between B^0 and $\bar{B}^0$. Consider the evolution of a state which starts as pure $\mid B^0 >$ at $t = 0$:

$$\mid B(t) >= \frac{1}{2}\left[e^{-i(M_1-\frac{1}{2}i\Gamma_1)t} \mid B_1 > + e^{-i(M_2-\frac{1}{2}i\Gamma_2)t} \mid B_2 >\right] \tag{1-28}$$

Since $\Delta\Gamma \ll \Delta M$ and $\Gamma_1 \approx \Gamma_2$, we have :

$$\mid B(t) >= e^{-iMt}e^{-\frac{1}{2}\Gamma t}\left[\cos(\frac{\Delta M}{2}t) \mid B^0 > \; - \; i \; \sin(\frac{\Delta M}{2}t) \mid \bar{B}^0 >\right] \tag{1-29}$$

As it decays the system oscillates back and forth between $\mid B^0 >$ and $\mid \bar{B}^0 >$ with a period proportional to $1/\Delta M$. The probability of observing $\mid B^0 >$ at time t is :

$$\begin{aligned} P(B^0 \to B^0, t) &= |< B^0 \mid B(t) >|^2 = e^{-\Gamma t}\cos^2(\frac{\Delta M}{2}t) \\ &= e^{-t/\tau}\left[\frac{1+\cos(\Delta M t)}{2}\right] \end{aligned} \tag{1-30}$$

For appreciable mixing to be seen, the system must not decay away too fast, so the size of ΔM relative to Γ is crucial. It is easier to see the time integrated effect. The integrated transition probability is :

$$\begin{aligned} r &\equiv \frac{mixed}{unmixed} = \frac{\int_0^\infty P(B^0 \to \bar{B}^0, t)\, dt}{\int_0^\infty P(B^0 \to B^0, t)\, dt} \\ &= \frac{\left(\frac{\Delta\Gamma}{2\Gamma}\right)^2 + \left(\frac{\Delta M}{\Gamma}\right)^2}{\left(\frac{\Delta\Gamma}{2\Gamma}\right)^2 + \left(\frac{\Delta M}{\Gamma}\right)^2 + 2} = \frac{y^2+x^2}{y^2+x^2+2} \\ &\approx \frac{x^2}{x^2+2} \end{aligned} \tag{1-31}$$

as y is expected to be small. The mixing parameters are defined as follows :

$$x = \frac{\Delta M}{\Gamma} \tag{1-32}$$

$$y = \frac{\Delta\Gamma}{2\Gamma} \tag{1-33}$$

$$\frac{\Delta\Gamma}{\Delta M} \propto O\left(\frac{m_b^2}{m_t^2}\right) \tag{1-34}$$

Sometimes the time integrated parameter is defined as :

$$\chi = \frac{mixed}{mixed + unmixed} \approx \frac{x^2}{2(x^2+1)} \tag{1-35}$$

The mixing parameter for B^0 is theoretically[12] estimated to be :

$$\begin{aligned} x &= \frac{\Delta M}{\Gamma} = \Delta M \tau_{B_d^0} \\ &= \frac{G_F^2}{6\pi^2} \tau_{B_d} B_{B_d} 2 f_{B_d}^2 M_{B_d} \mid V_{tb} V_{td}^{\star} \mid^2 A\left(\frac{m_t^2}{m_W^2}\right) m_t^2 \end{aligned} \tag{1-36}$$

where τ_{B_d} is the B_d meson lifetime, $B_{B_d} \approx 1$ is the bag parameter of B_d and f_{B_d} is the decay constant of B_d, while A is given by :

$$A(x) = \left[1 - \frac{3(x+x^2)}{4(1-x)^2} - \frac{3x^2}{2(1-x)^3}\, log\, x\right] \tag{1-37}$$

CHAPTER 2.

The Accelerator and the Detector

The experimental data analyzed in this thesis is the product of the CDF detector to observe the $p\bar{p}$ collisions at the Fermilab final stage accelerator, the Tevatron. The Tevatron is at present the highest energy particle accelerator in the world. This chapter gives a brief description of the accelerator[14] and detector.

A. The Accelerator

At Fermilab, the Tevatron is the final stage of a series of particle accelerators. It is the world's highest-energy particle accelerator. The Tevatron provides beam for experiments in 3 modes :

- the fixed target mode
- the antiproton mode
- the collider mode

In the fixed-target mode, the Tevatron accelerates protons up to 800 GeV, then directs them at targets in the experimental halls. A second mode uses antiprotons stored and cooled in the Antiproton Storage Ring for experiments with a gas jet target. In the collider mode, the Tevatron accelerates proton and antiproton bunches up to 900 GeV, in opposite directions, and brings the counter-rotating beams into collision. To sort and analyze the multitude of particles originating from the collisions at 1.8 TeV center-of-mass energy, collider detectors (CDF and D0) operate at two sites around the Fermilab ring.

The diagram in Figure 2-1 shows the paths taken by protons and antiprotons in Fermilab's five accelerators. The first stage of acceleration starts at the Cockcroft-Walton apparatus, where electrons are added to hydrogen atoms. A positive voltage attracts and accelerates the resulting negative hydrogen ions, each consisting of two electrons and one proton, to an energy of 750,000 electron volts which is about thirty times the energy of the electron beam in a television's picture tube. Leaving the Cockcroft-Walton, the negative hydrogen ions enter a 500 foot long linear accelerator (Linac) consisting of drift tubes, spaced further and further apart. Before entering the third stage, the Booster, the ions pass through a carbon foil which removes the electrons, leaving only the protons with an energy of 200 MeV. The Booster is a rapid cycling synchrotron 500 feet in diameter. The protons travel around the Booster about 20,000 times and their energy is raised to 8 GeV before being injected into the Main Ring. In the Main Ring, which is a 4 mile proton synchroton, protons are accelerated to 120 GeV. They are then extracted and channeled to a target area and focused onto a tungsten target. The collisions in the target produce a wide range of secondary particles including antiprotons. These are selected and transported to the debuncher ring where the transverse dimension of the antiproton beam is reduced in size by a process known as stochastic cooling. The antiprotons are then transferred to the accumulator ring for storage. Finally, when a sufficient number has been produced and stored, the antiprotons are reinjected into the Main Ring and passed down into the Tevatron where they are accelerated simultaneously with a counter-rotating beam of protons to an energy of 900 GeV. Six proton bunches and six antiproton bunches are injected into the Tevatron. There are four interaction regions (B0, C0, D0 and E0) around the ring to accomodate experimental halls with their accompanying detectors The CDF experiment is located at the B0 interaction region.

B. The CDF Detector

CDF[15] was built to study 1.8 TeV center-of-mass collisions. The basic goal for CDF is to measure the energy, momentum and where possible the identity of particles produced over as large a fraction of the solid angle as practical. It

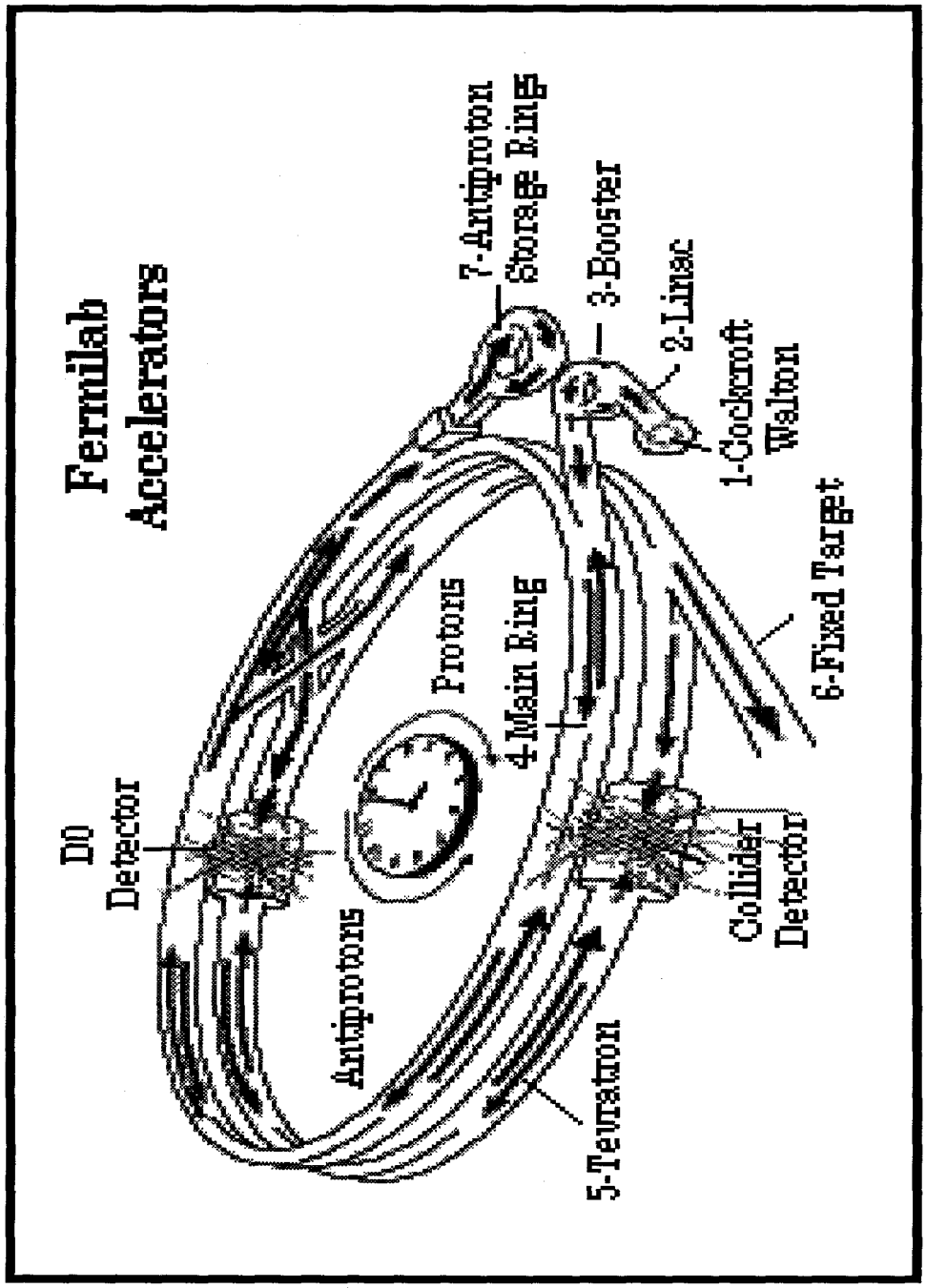

Figure 2-1. Fermilab accelerator system components : 1.Cockcroft-Walton, 2.Linac, 3.Booster, 4.Main Ring, 5.Tevatron, 6.Fixed Target Area, 7.Antiproton Storage Rings.

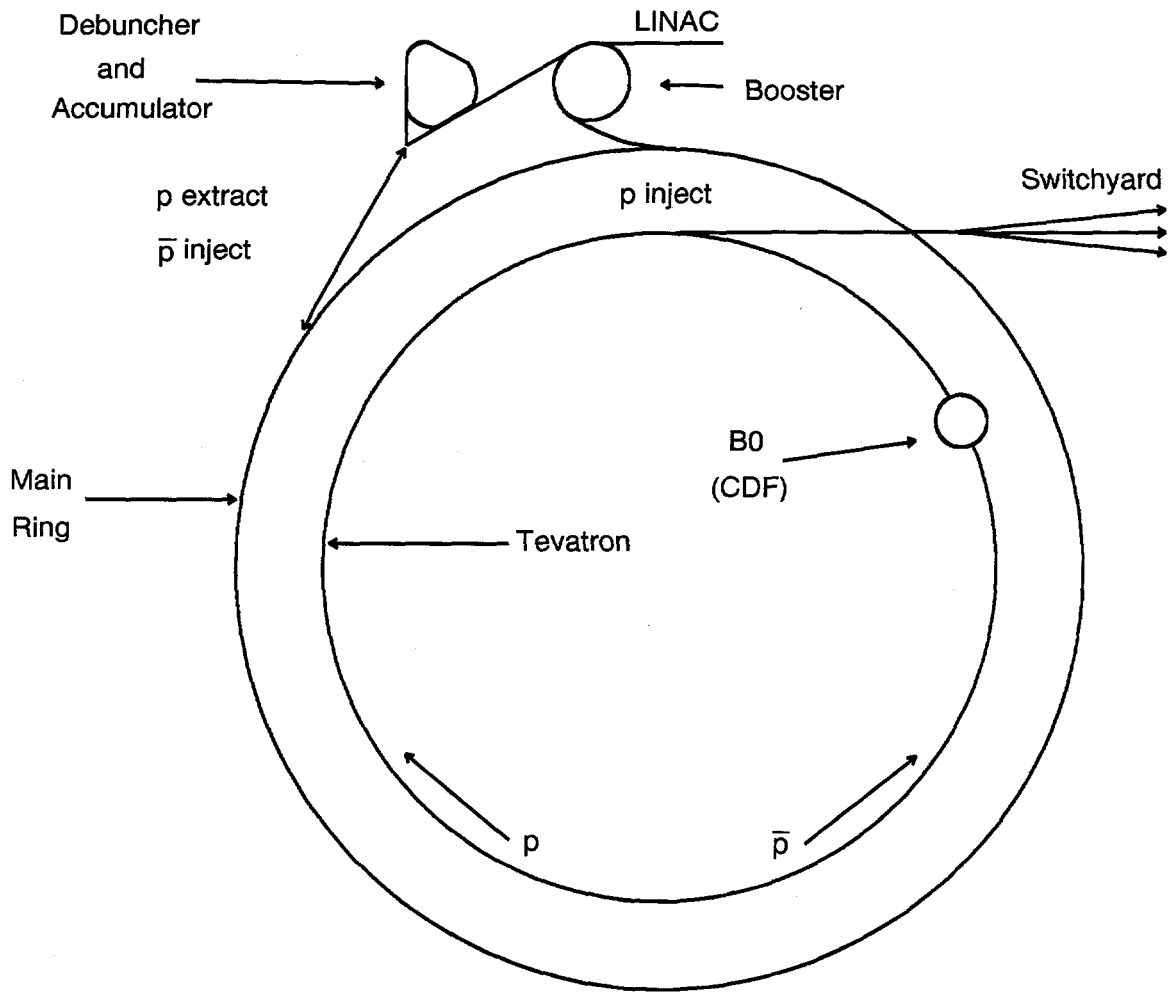

Figure 2-2. Bird's eye schematic drawing of the beamlines. The figure shows the Linac, Booster, Main Ring, Tevatron and the Anti-proton storage ring

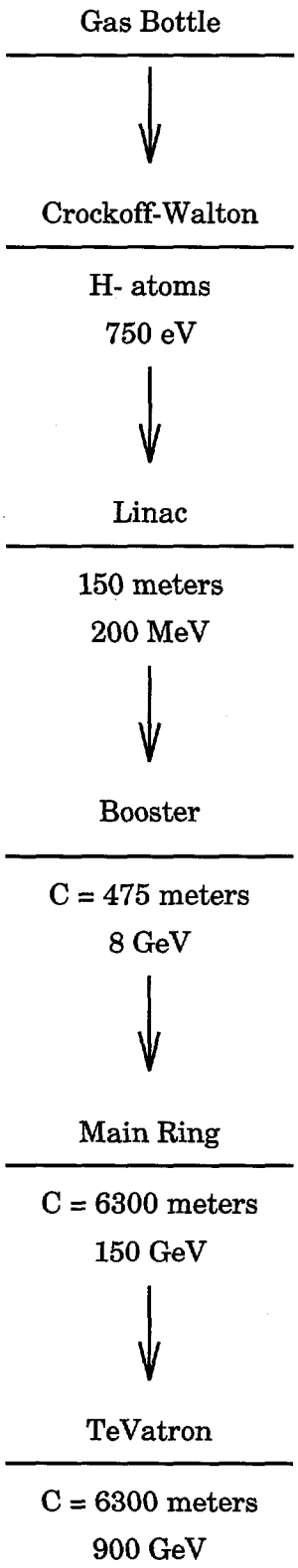

Figure 2-3. Flowchart of the protons acceleration up to 900 GeV/c^2

is a solenoidal detector with azimuthal symmetry and forward and backward symmetry around the collision center, finely segmented in both pseudorapidity and ϕ angle around the beampipe. A magnetic field of 1.4 Tesla is produced by the superconducting solenoid. This field is useful for the determination of the charge sign and the momentum of charged particles.

Proton beams enter the B0 collision hall from the West and antiproton beams from the East. The direction of the proton beam is taken to be the direction of the z axis (positive z is eastward). The vertical is the y axis and the x axis is then fixed by a right-handed coordinate system requirement. The azimuthal angle ϕ is measured from the x axis counterclockwise around the z *axis*, and θ from the positive z axis. The natural phase space for energetic hadron collisions is a function of rapidity, transverse momentum and azimuthal angle. Pseudorapidity is defined in Equation 2-1.

$$\eta = -\log\left(\tan\frac{\theta}{2}\right) \tag{2-1}$$

CDF is grouped into three sections, the central section, the plug and the forward chambers. The central section surrounds the nominal center of collision. Starting at the interaction point, particles encounter sequentially, a thin wall beryllium vacuum chamber, charged particle tracking chambers, the superconducting solenoidal magnet, calorimeters and muon detectors. The tracking chambers are used to detect charged particles and measure their momenta. The central tracker, covering the central region in the pseudorapidity range of ± 0.6, consists of a Silicon Vertex Detector (SVX') closest to the beampipe, a Vertex Tracking Chamber (VTX) which surrounds the SVX, and a Central Tracking Chamber (CTC) which surrounds the VTX. Calorimeters sum up the electromagnetic and hadronic energies of the jets of particles. The muon drift chambers are used to detect muons. Particles emerging out of the central range are covered by the plug and forward region detectors.

1. SVX' Detector

SVX' consists of two independent cylindrical modules of equal length. These modules, aligned along the beam line (z-axis of the CDF detector) are placed

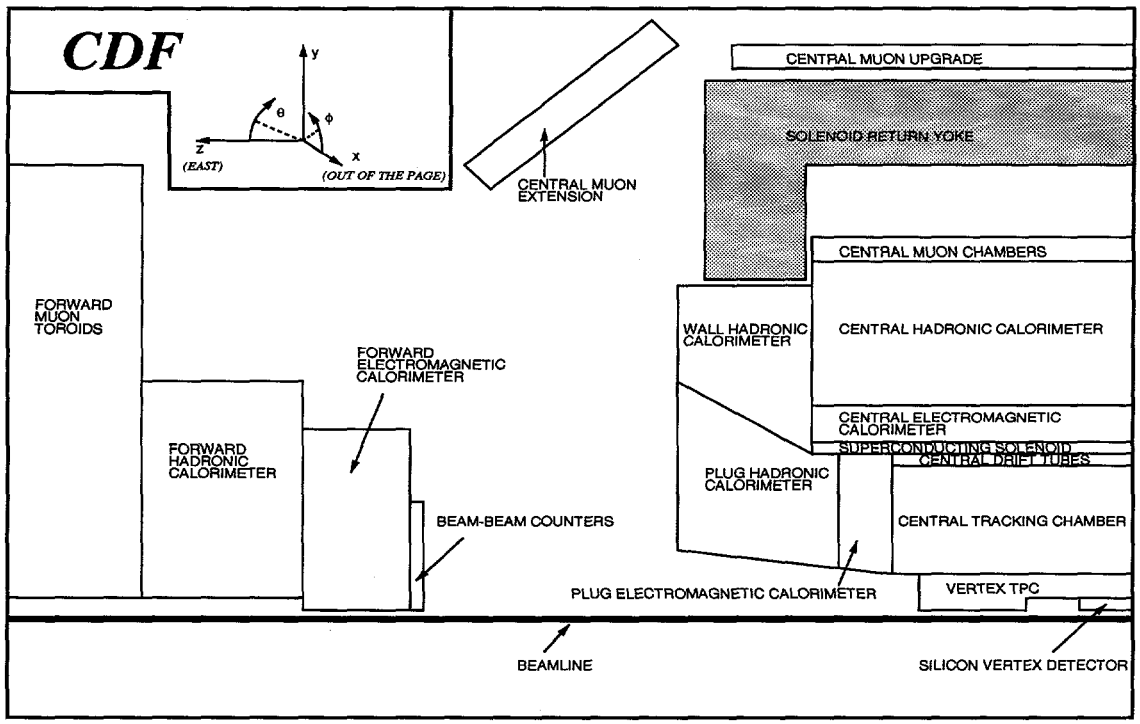

Figure 2-4. A side view cross section of the CDF detector. The detector has forward and backward symmetry around the interaction region in addition to azimuthal symmetry.

on both sides of the center of the CDF detector (z=0) with a gap of about 2.15 cm at z=0. The active length of SVX' is 51 cm which has an acceptance of $\sim$ 60% of the $p\bar{p}$ collision vertices. Each module (also referred to as barrel) consists of four concentric layers, numbered from 0 to 3 in increasing radius (see Fig.2-5). The inner and the outer radii of the barrel are 2.8612 and 7.8658 cm respectively. Shown in Fig.2-6, the basic building block of the layers is a ladder which has three AC coupled, single sided silicon strip sensors. The sensors are made up from 300 μm thick silicon wafers micro-bonded to one another. Each SVX′ barrel is divided into 12 wedges of 30° in ϕ and the wedges are read out independently. To reduce the amount of raw data, only signals above a certain threshold are read out from the detectors. Since SVX′ is AC coupled, the DC leakage current will not be seen by the readout electronics, thus SVX′ operates in a double sample and hold mode, where the charge integration is done during "beam on". The characteristics of each channel of SVX′ was monitored by taking calibration runs between the Tevatron stores when there was no beam activity. Calibration studies included measuring the pedestal, gain and the threshold of each channel of the device. Of the total 46080 channels of SVX′, about 1.7% had a shorted coupling capacitor. These channels were not bonded to the readout chip, instead they were grounded through a capacitor on the dummy (non readout) end. The first step in the offline reconstruction of tracks in SVX′ is the conversion of the charge on individual strips to clusters followed by matching of these clusters to tracks found by the Central Tracking Chamber(CTC). The conversion from the charge levels on an individual strip starts with the offline subtraction of the pedestals. The pedestal subtraction is carried out on a strip by strip basis and the pedestal values are taken from a pedestal calibration run. After the pedestal subtraction the strips are clustered using a clustering algorithm that requires that there be a group of contiguous strips which have a charge greater than 'M' times the noise, where 'M' is 4, 2.5, and 2 for 1 strip, 2 strip and $\geq$ 3 strip clusters, respectively. The values of 'M' were optimized for good hit efficiency and noise rejection using cosmic ray and collision data. Cluster positions were calculated as the charge weighted centroid using individual strip charges and strip positions. The hit efficiency for SVX′ is affected by S/N, pedestals, clustering, pattern recognition, dead strips and

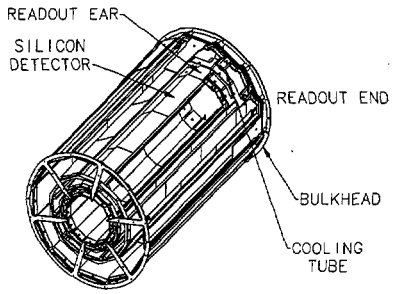

Figure 2-5. Schematic drawing of one of the SVX' barrel

geometrical acceptance. Since the detector has some ϕ gaps and dead strips the hit efficiency can never be 100%.

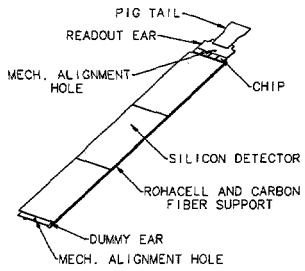

Figure 2-6. Schematic drawing of an SVX' ladder.

2. VTX - Vertex Tracking Chamber

The VTX is a proportional wire chamber consisting of eight octagonal modules, which are arranged to form a barrel surrounding the SVX'. Each wedge of the octagonal module has wires parallel to the base of the wedge. This arrangement accomodates an accurate measurement of the the primary vertex in z. The chamber is filled with a gaseous mixture of 50% argon and 50% ethane bubbled

through alcohol at -7^{o}C. A charged track passing through the chamber makes an ionization trail in the gas mixture. The electron from the ionization trail is attracted to the wires. The resulting avalanche causes a drop in the wire voltage. The VTX can measure the z position of the primary vertex to an accuracy of 2 mm.

3. CTC - Central Tracking Chamber

Surrounding the VTX, the CTC drift chamber is the principal tracking device of the CDF detector. It is inside a 1.4 T solenoidal magnet. The barrel of the drift chamber has a diameter of 2.76 m and a length of 3.2 m. There are 36,504 sense and field shaping wires extending along the length of the CTC. The chamber is filled with argon-ethane gas mixture. The wires are arranged into 84 layers which are divided into 9 superlayers, five axial and four stereo (3^{o} tilt) layers. The axial superlayers have twelve layers of wires and are alternated with the stereo superlayers each of which have six layers of wire. The wires within a superlayer are grouped in measurement cells so that the maximum drift distance is less than 40 mm, corresponding to 800 ns of drift time. Figure 2-7 shows the diagram of the CTC endplate depicting the arrangement of the blocks which hold the 84 sense wires. The detector resolution is

$$\frac{\delta P_t}{P_t} = 0.0011 \times P_t \tag{2-2}$$

$$\delta(r\phi) = 0.2\ mm \tag{2-3}$$

$$\delta z = 4\ mm \tag{2-4}$$

4. Calorimetry

The calorimeters consist of central, plug and forward calorimetry regions which are segmented in azimuthal and pseudorapidity increments to form a projective tower geometry pointing back to the interaction point. Each region has an electromagnetic calorimeter and behind it a hadronic calorimeter. The central electromagnetic calorimeter is labeled CEM, the plug calorimeter is labeled

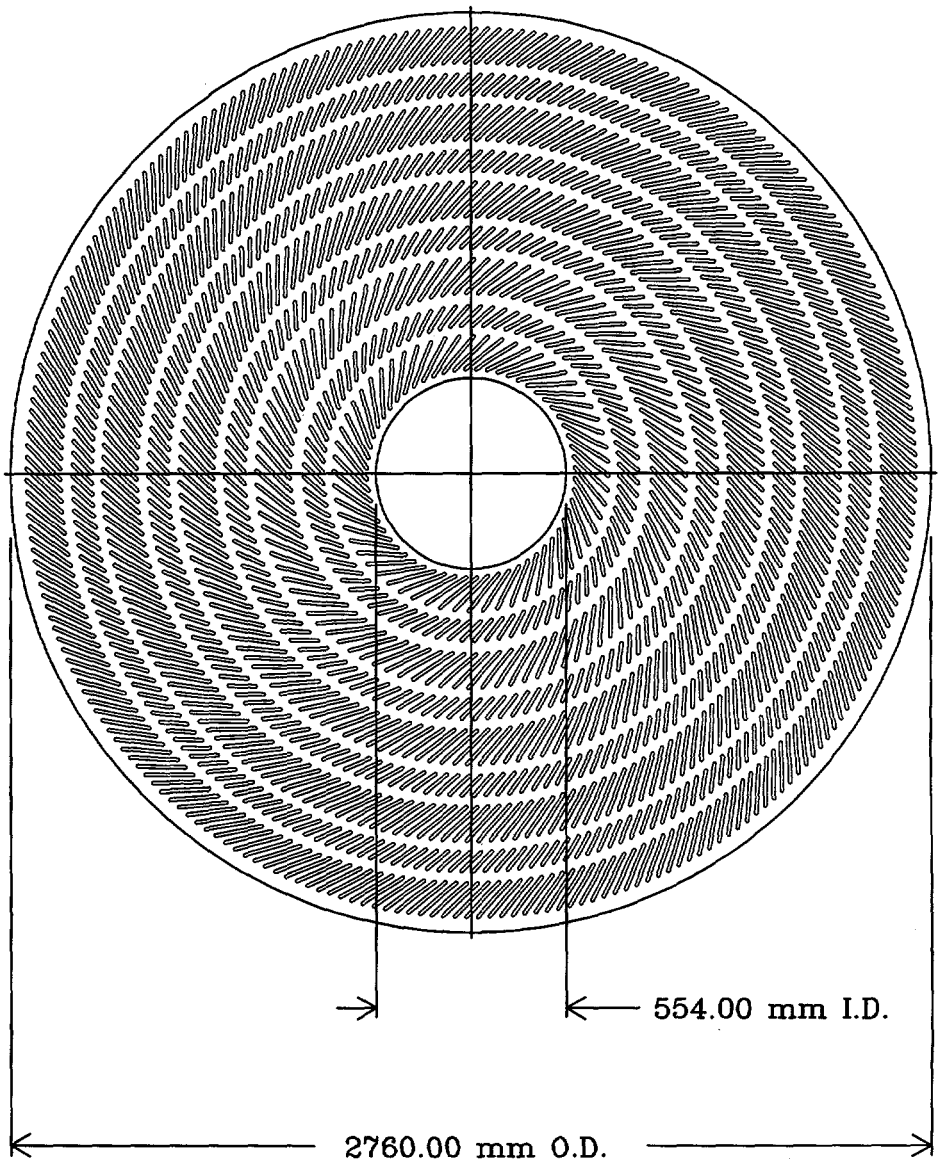

Figure 2-7. The CTC endplate showing the arrangement of the blocks which hold the 84 sense wires.

PEM and the forward calorimeter is labeled FEM. The hadronic calorimeter overlapping the CEM is divided into two parts, the central part (CHA) and the wall part (WHA). The PEM is overlapped by the PHA and the FEM is overlapped by the FHA. The absorber in the hadron calorimeter is made of iron and the electromagnetic calorimeters of lead. Figure 2-4 shows the locations of the various calorimeters. Table 2-1 shows the coverage, thickness and resolution of these calorimeters and Fig.2-8 shows the coverage in η and ϕ schematically.

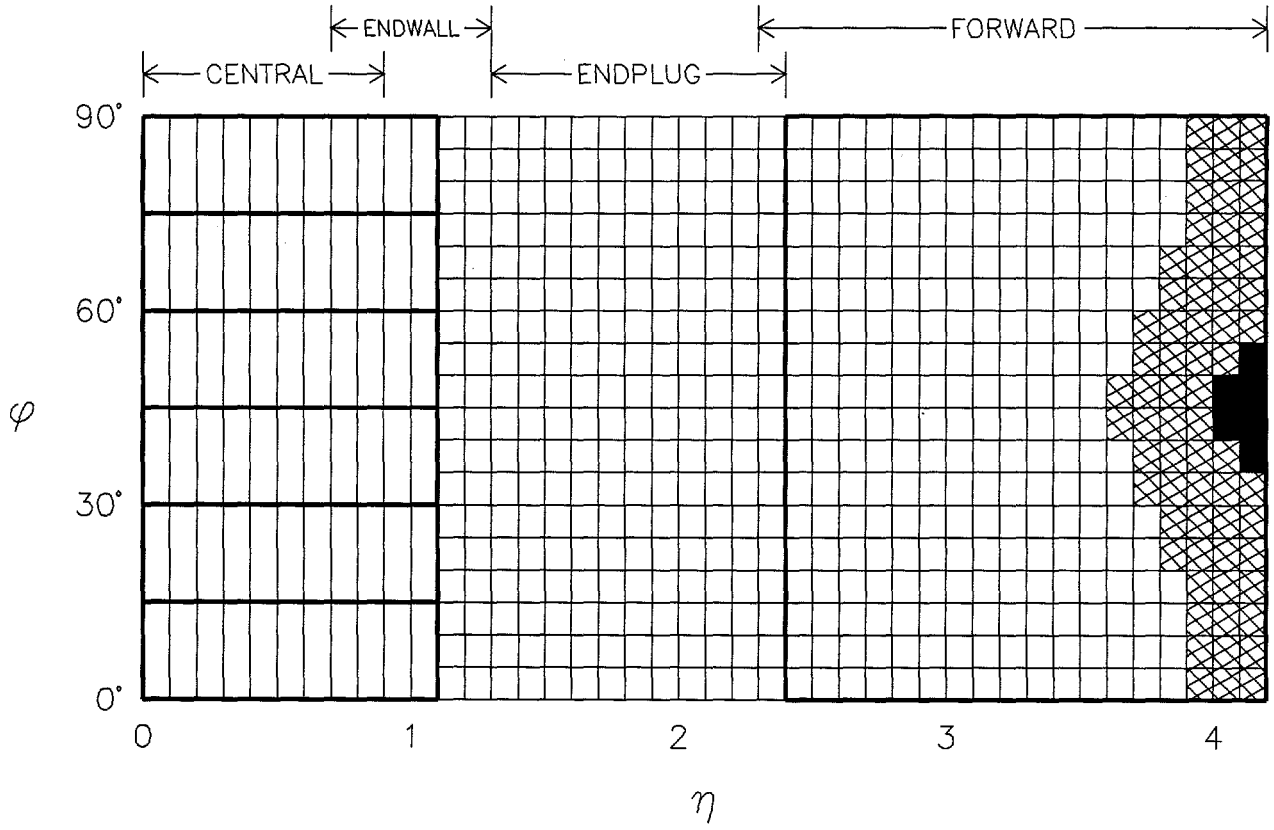

Figure 2-8. The η and ϕ coverage of the various calorimeters at CDF.

Calorimeter	Coverage in η	Energy Resolution	Thickness
CEM	$\|\eta\| < 1.1$	$13.7\%/\sqrt{E_t} \bigoplus 2\%$	$18X_0$
PEM	$1.1 < \|\eta\| < 2.4$	$22\%/\sqrt{E_t} \bigoplus 2\%$	18-21X_0
FEM	$2.2\|\eta\| < 4.2$	$26\%/\sqrt{E_t} \bigoplus 2\%$	$25X_0$
CHA	$\|\eta\| < 0.9$	$50\%/\sqrt{E_t} \bigoplus 2\%$	$4.5\lambda_0$
WHA	$0.7 < \|\eta\| < 1.3$	$75\%/\sqrt{E_t} \bigoplus 2\%$	$4.5\lambda_0$
PHA	$1.3 < \|\eta\| < 2.4$	$106\%/\sqrt{E_t} \bigoplus 2\%$	$5.7\lambda_0$
FHA	$2.4 < \|\eta\| < 4.2$	$137\%/\sqrt{E_t} \bigoplus 2\%$	$7.7\lambda_0$

Table 2-1. Summary of the CDF calorimeter properties. The symbol $\bigoplus$ implies that the constant term is added in quadrature in the resolution. The energy resolutions for the electromagnetic calorimeters are for incident electron and photons and for the hadron calorimeters are for incident isolated pions. The unit of energy is GeV. The thickness for the electromagnetic calorimeters is given in radiation lengths (X_0) and for hadronic calorimeters it is given in interaction lengths (λ_0)

The central calorimeter towers are 15^o wide in ϕ and 0.1 unit wide in η. They use scintillating polystyrene as active material. In the presence of ionizing radiation it emits blue light which is collected in acrylic doped wave length shifter and is directed to a photomultiplier tube through clear acrylic light guides. At six radiation lengths into the CEM calorimeter there are central proportional chambers with strip and wire readout called the central electromagnetic strip detector (CES). CES provides shower position measurements in both the z and the $r - \phi$ views. The proportional chamber located between the solenoid and the CEM constitutes the central pre-radiator (CPR) detector. CPR samples the early development of the electromagnetic shower in the material of the solenoidal coil. It provides only the $r - \phi$ information. In the plug and the forward region the active medium consists of proportional chambers with argon-ethane gas mixture. Each PEM detector is a torus, 2.8 m in diameter and 50 cm deep. It consists of 34 layers of conductive plastic proportional tube arrays interleaved

with 2.7 mm lead absorbers. The cathode readout consists of pads and strips etched out on printed circuit boards. This results in a finely segmented projective geometry. The PHA lies just outside the PEM. It is shaped like a cone and is made up of 20 layers of proportional tubes alternated with 5.1 cm thickness iron plates. The FEM detector is composed of 30 layers of proportional tubes alternated with 0.48 cm lead-antimony alloy plates. The FHA has 27 layers of proportional tubes alternated with 5.1 cm iron plates.

5. CMU - Central Muon Chambers.

The central calorimeters act as hadron absorbers for the central muon (C M U) detection systems. CMU consists of four layers of drift chambers located outside the central hadronic calorimeters. Each drift chamber measures 6 cm by 2.7 cm by 2.2 mm and has one stainless steel resistive 50 μm sense wire in its center (see Fig. 2-9). The CMU covers $|\eta| < 0.6$ and can be reached by muons with a P_t in excess of 1.4 GeV/c. In the 1992 CDF upgrade, 0.6 m of steel was added behind the CMU for additional hadron absorbtion and four more layers of drift chambers were added behind the additional steel for muon detection. This system is called the CMP (Central Muon Upgrade.) CMU covers about 84% of the solid angle for $|\eta| < 0.6$, CMP covers 63% of the solid angle and the overlap of the two covers 53% of the solid angle. The coverage in the central region is extended to the pseudorapidity $0.6 < |\eta| < 1.0$ through the addition of four free standing conical arches which hold the drift chambers for muon detection. The drift chambers are sandwiched between scintillator counters which are used for triggering. This extension is called CMX and it covers about 71% of the solid angle for $0.6 < |\eta| < 1.0$. Figure 2-10 shows the η and ϕ coverage schematically.

The forward muon chambers (FMU) consist of three sets of drift chambers. Large cast steel toroids are placed in front of the FMU to produce a 1.4 T magnetic field at 2.0 m. This field helps determine the momenta of the charged muon tracks. The FMU has a diameter of 7.6 m which matches the diameter of the toroids. It is segmented in r and ϕ so that the three dimensional momenta of the muons can be measured.

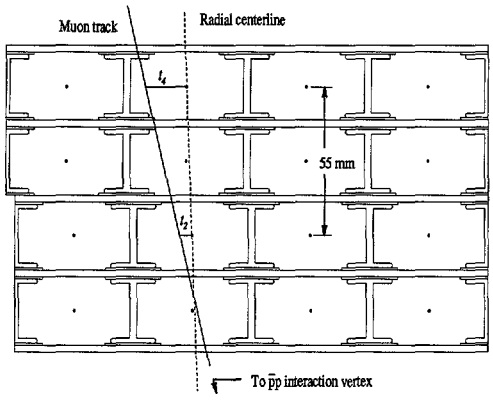

Figure 2-9. The cross sectional view of the muon chambers

6. BBC - Beam-Beam Counter.

The Beam-Beam counter (BBC) is located just in front of the forward calorimeter at 5.8 m from the interaction point and ranges from 0.32 to 4.47 degrees in θ. The BBC's are small scintillating detectors. Having a crucial role in the experiment they are used for the level 0 triggering and the luminosity measurements. If tracks do not leave a signal in the both the BBC's within a 15 ns window, the detector is not read out. The luminosity is measured by counting the number of collisions when the BBC has allowed the detector readout.

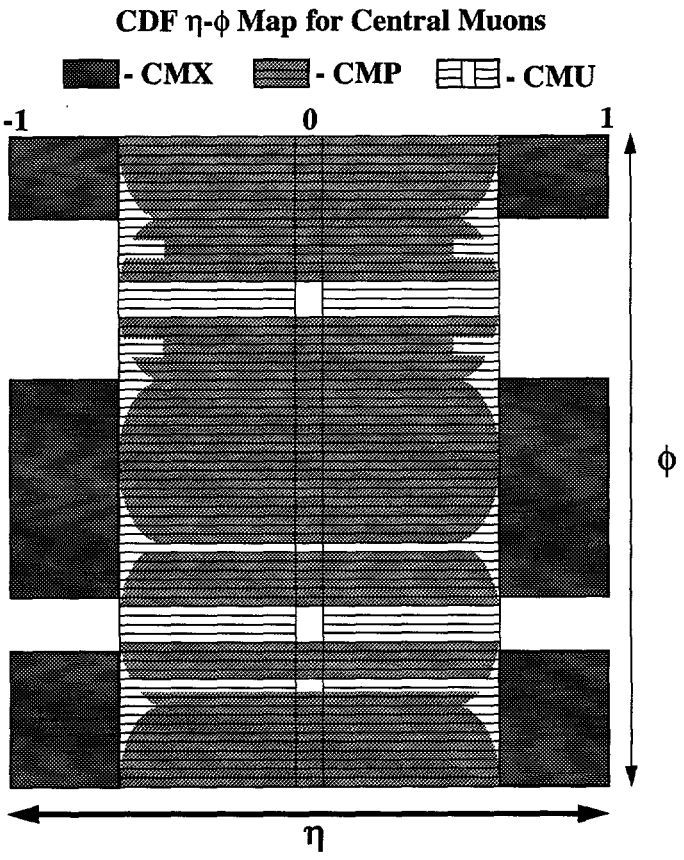

Figure 2-10. The η and ϕ coverage of the various muon chambers at CDF.

CHAPTER 3.

Data Acquisition System

A. Trigger

CDF was built to study the physics resulting from $p\bar{p}$ interactions at a center of mass energy of 1.8 TeV. The visible cross section for $p\bar{p} \rightarrow X$ at the design luminosity $\mathcal{L} \sim 10^{31}\ cm^{-2}\ s^{-1}$ is $\sigma_{vis} \sim 46mb$, thus the expected interaction rate is $R = \sigma_{vis} \times \mathcal{L} \sim 500$ kHz. But there are actually only 6 bunches of protons and 6 bunches of antiprotons instead of a continuous beam. The beam crossing occurs only every 3.5 μs. So if we expect at least one interaction per crossing, then we expect to have an interaction rate of about 286 kHz. The rate of data taking is limited mostly by two factors, the rate at which events can be written to tape and the rate at which physicists can analyze the data. The rate at which events can be written to tape is about 10 Hz. So 1 event must be selected out of every 20 - 30 events. This is accomplished with the trigger system. The CDF trigger[16] consists of 3 levels. Level 1 and Level 2 are made of specially designed hardware which makes the decision to initiate the full detector readout. Level 3 is a software trigger. The purpose of a multi-level trigger system is to introduce as little bias as possible at the lower levels, with the goal of reducing the rate to a point where the next level can do a more complex analysis without incurring significant deadtime. The readout of the detector components is the most time consuming process at CDF, which is of order 1 ms. So to keep the deadtime due to readout below 10%, the detector readout should begin after the Level 2 trigger has cut the rate down to 100 Hz or less.

In designing the trigger for CDF, three factors were considered. First, the system must be capable of triggering on the signatures of known physics, such as $Z^0 \rightarrow \mu^+\ \mu^-$ or $e^+\ e^-$, $W \rightarrow e\ \nu$ or $\mu\ \nu$, jets, etc. The trigger should

also be able to include signatures of as yet unknown physics. And finally, the trigger electronics should be able to exploit the various strengths of the detector as much as possible. The strengths of CDF detector are finely segmented, projective electromagnetic and hadronic calorimeter, accurate tracking, and a strong magnetic field. To allow a trigger decision based on the topology of transverse energy flow and on the identification of electrons, muons and jets in the event, the segmentation of calorimeters should be preserved at the trigger level. Information about high P_t tracks and muon candidates should be included at both Level 1 and Level 2.

Level 1 has no deadtime since the decision is made in the 3.5 μs before the next beam crossing. Both hadronic and electromagnetic calorimeter towers are summed into trigger towers with a width in psedorapidity of $\Delta\eta = 0.2$ and a width in ϕ of $\Delta\phi = 15°$. Both electromagnetic and hadronic calorimeters constitute an array of 42 by 24 (in η and ϕ). Output from all photomultipliers are sent to the counting room individually and summed into the $\Delta\phi = 15°$ and $\Delta\eta = 0.2$ trigger towers. The signals are weighted by $sin\ \theta$ to obtain the transverse energy E_t deposited in the tower. Level 1 decision is based on the following requirements :

1. The presence of a single tower with the sum of E_t in that tower above a preset threshold. The thresholds are set separately for CEM, CHA, PEM, PHA, FEM and FHA.

2. Prescaled calorimetry where one out of every 40 (this number changes) crossings will have a lower threshold.

3. The existence of high P_t single muons or low P_t dimuons in CMU and CMX.

4. The existence of single and dimuons in FMU.

5. The presence of a beam-beam interaction reported by the beam-beam counters.

The rate of acceptance for Level 1 is about 1000 Hz.

The Level 2 trigger[17] starts after an event is accepted by The Level 1 trigger. The same hardware is used by Level 2 to find clusters of total energy in the $\eta - \phi$ array of towers. Towers below a programmable threshold are ignored. Clusters of energies are identified by a hardware cluster finder. The energies of all towers in a cluster are summed to get the total E_t. Hadronic and electromagnetic sums of E_t are kept separately, put in a list of clusters and digitized for the two Level 2 simultaneously running processors to analyze. Each cluster is matched to CTC tracks by CFT, a fast (10 μs) tracking processor. If a match is found, then a coarse P_t measurements appears in the list, with a precision of $\frac{\Delta P_t}{P_t} \sim 0.035 P_t$. Level 2 also extrapolates these CTC tracks out to the muon chambers; this way the momentum of muons in the event can be determined. Then a selection on muons, electrons, photons, jets and missing E_t is made by a preprogrammed Level 2 processor. Many combinations of the above can be programmed in parallel. Level 2 deadtime is about 20 μs. The rate of acceptance for Level 2 is 15-20 Hz.

The Level 3 trigger[18] system consists of a farm of UNIX computers which perform event reception, building, reconstruction, classification, and selection using a set of criteria given by consumers. So Level 3 executes a code to make final decision whether an event should be written to tape or not. The rate of acceptance for Level 3 is 5-10 Hz. Events are written to magnetic tape at a rate of about 10 Hz.

B. On-line Control Systems

Reading of events, detector calibrations, and hardware diagnostics is controlled by a computer process called RUN_CONTROL. Subsystems of detector can be grouped into separate DAQ (Data Acquisition) systems for calibration or diagnosis. The calibration or diagnosis is executed by multiple RUN_CONTROL processes running simultaneously on several of the VAX processors in the CDF computing cluster. A single RUN_CONTROL process controls the DAQ hardware and the flow of data during physics data taking.

The data being taken can be accessed by different monitoring programs, data diagnostics, physics analysis and event selection filters as independent

"consumer processes" on any of the VAX in the CDF cluster or remotely via a network. Programs to identify bad electronic channels, monitor trigger rates and accumulate luminosity information are examples of standard processes that access events during data acquisition. The status of the detector is monitored by a separate process called "ALARMS and LIMITS." Calibrations are performed between data runs to measure pedestal offsets and gains for the calorimeters, and to measure constants of other systems. The calibration result which is stored in large databases, can be extracted at the start of each data run to be downloaded into the detector subsystems.

C. Outline of CDF Data Acquisition Pipeline

Data from the front end electronics is read over the FASTBUS by FASTBUS Readout Controllers (FRC's)[19]. FASTBUS[20] is a standardized modular data-bus system for data acquisition, data processing and control applications. It is the result of a development by various labs to meet the needs of the High Energy Physics community. A FASTBUS system consists of Bus Segments operating independently but linked together dynamically as needed for operation passing. This parallel processing feature results in a high throughput of FASTBUS in multisegment systems. Master modules compete for single or multiple segment control through a bus arbitration scheme using assigned priorities. FRC is a single width FASTBUS module containing MIPS R3000 processor with VxWorks real time operating system and uses an ethernet/TCPIP connection. FRC is a front end scanner.

Scanner CPUs (SCPUs) read FRC data via Scanner Bus. Scanner CPUs are VME [1] based Synergy Corporation CPUs. SCPU then sends the data to Level 3 Silicon Graphics systems via Ultranet. The Ultranet network is a high speed, scalable, switched electronic network with a function similar to that of ethernet but much faster. Since it is switched, it is based upon a hub or central switch. It is a commercial high performance serial network with 256 MB/sec serial links.

[1] VME stands for Versa Module Eurocard. It is a crate based electronicspackage scheme

Events accepted by the Level 3 trigger are also sent to the Consumer Server via Ultranet. A Consumer Server is a process running on CDF Silicon Graphics Challenge L. The Consumer Server then distributes the events to various Consumer Processes over ethernet or FDDI (fiber optic ethernet). A process called the Data Logger in the Consumer Server system writes the events to disk and produces data output files for another program called the Tape Stager to copy to 8 mm tapes. The Data Logger separates events into 3 different streams of data, namely stream A, stream B and stream C. These different streams will be discussed in the next section.

Figure 3-1 shows the flow chart of the CDF DAQ system. A scenario of the system activity goes as follows :

1. The Level 1 trigger decision is completed within the 3.5 μs interval between beam crossings

2. When the event is accepted by Level 1, it is passed to Level 2. The dead time at Level 2 is about 20 μs.

3. If Level 2 rejects this event, then this event will be cleared. An acceptance of this event by Level 2 will cause this event to be readout. The deadtime during readout is about 3.5 ms.

4. When the Trigger Supervisor (TS) receives a Level 2 Accept signal, it will send a Start-Scan broadcast message over the FASTBUS indicating which FRC buffer is to be used. There are 4 buffers (0-3). The main function of TS is to coordinate the trigger system, the FRC's and the Scanner Manager. Currently there are 4 partitions of TS.

5. FRC's and MX's scan TDC's from different parts of the detector. MX performs a more complex process, while FRC just reads the events. The arrangement is such that the output of MX has to go through the FRC's to get to the Scanner Bus. Each FRC and MX lowers its DONE signal and starts its readout when it receives the Start-Scan message from TS.

6. A DONE signal is raised, when each FRC and MX finishes its readout. This DONE signal is sent to the different partitions of TS through a DONE

CROSS POINT (some sort of multiplexor). FRC's inform SCPU's that they have an event to be read out.

7. When all FRC's and MX's have returned DONE, the TS clears and re-enables the front-end and sends a Buffer-Full message to the Scanner Manager.

8. The Scanner Manager (SM) sends a Scramnet message telling the SCPU's to read out the appropriate FRC buffer. A Scanner Manager is a program running on a Synergy Corporation CPU with a VxWorks operating system and an ethernet connection. It controls flow of data from FRC's to Level 3, ensuring that all fragments of an event get to the same Level 3 system. It communicates with TS via Trigger Supervisor Interface (TSI). It also communicates with the SCPU's and Level 3 via the Scramnet fiber optic network. TSI is actually two FRC's connected to SM via a Scanner Bus. It is a bridge between TS and SM. A Scramnet is a reflective memory network. It consists of VME memories in separate crates connected in a ring topology by fiber optic cables. A write to a memory location on one module is automatically propagated to the same location on all modules in the network; this results in a very fast transfer of single words within the network. It is used for control messages only.

9. After reading out all of its FRC's, each SCPU sends a Scramnet message to the SM indicating that it has finished.

10. When all SCPU's have finished reading the event, the SM sends a Buffer-Free message to the TS.

11. The TS returns the freed buffer to its available list.

12. The Scanner Manager tells the SCPU's to send the event to an available Level 3 Event Receiver.

13. After sending its event fragment to Level 3, each SCPU tells SM that it has finished.

14. When all SCPU's have finished sending the event, the SM sends an Event-Complete message to the Level 3 Event Receiver.

15. The Receiver passes the event to the Level 3 Event Input processor and informs the SM that it is ready for another event.

16. The Level 3 Event Input processor reformats the event into YBOS banks and copies it to the Level 3 Global Buffer.

17. When an event appears in the Level 3 Global Buffer, it is analyzed by the Level 3 Executable (reconstruction program).

18. If the event satisfies one of the sets of requirements from the various consumers, the event is sent to the Consumer Server.

19. Events which pass stream A, B or C requirements are passed to the appropriate Data Logger running on the same computer as the Consumer Server and written to disk.

20. Events which pass non-VIP requirements are sent from the Consumer Server to consumers over the ethernet.

21. When a full tape's worth of Stream A, B or C data has been written to disk, it is copied to 8 mm tape by a process running on the Consumer Server computer.

D. The Run I Data System

In Run I CDF recorded 64 million events in the main data stream (Stream B) which were processed in real-time and made available to the physicists within about 2 weeks of the data being taken. In addition, 3.7 million events out of the total were also recorded in a separate "express line" stream (Stream A) and processed within hours. This stream contained the high-transverse momentum leptons necessary for the top quark search. It was also used to monitor data quality during the run. An additional 28 million events were recorded for processing after the data taking ended (referred to as Stream C). These events were mainly low-transverse momentum leptons intended for studies of b-quarks.

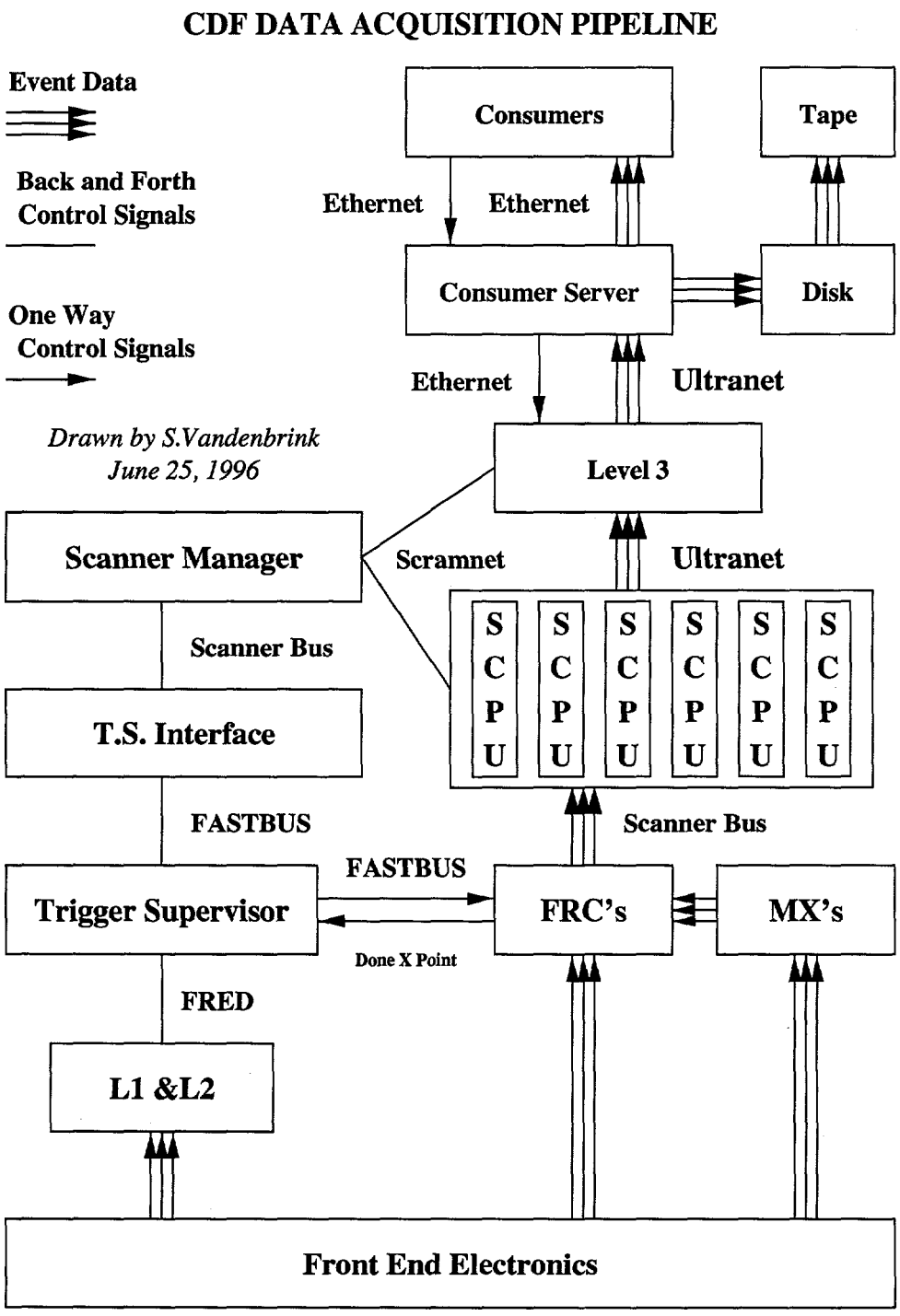

Figure 3-1. CDF data acquisition system flow chart.

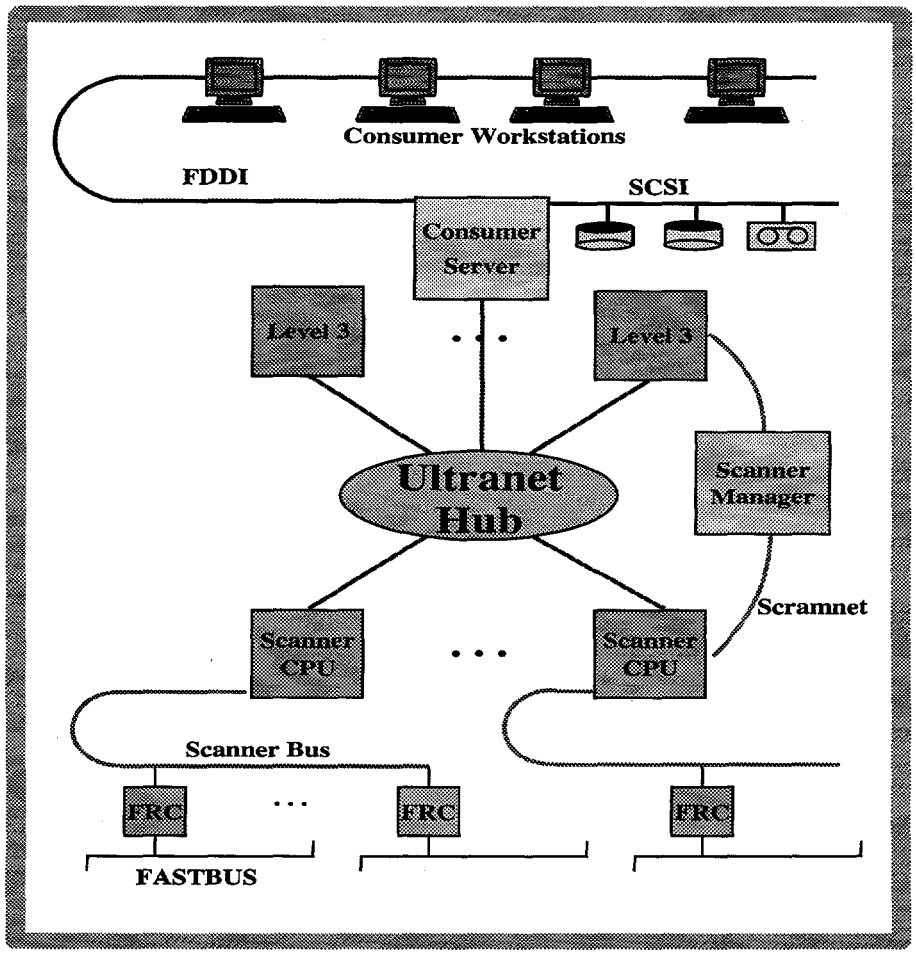

Figure 3-2. CDF data acquisition system

The analysis computing needs for Run I were provided by a mix of central and desktop systems. These systems were a combination of VAX/ALPHA machines running VMS and Silicon Graphics/IBM machines running UNIX. The central VMS system consisted of about 1200 MIPS of CPU (FNALD) and the central UNIX system (a SGI Challenge XL with 28 processors - CDFSGA) consisted of 2400 MIPS. In addition, the desktop systems add 3000 MIPS of VMS computing and 1600 MIPS of UNIX computing. The production computing needs were met by the centrally supported UNIX farms. CDF had an allocation of 3000 MIPS of farm computing in the form of 63 SGI 4D/35 nodes and 32 IBM 320H nodes. The data were processed on the farm nodes and then split up into physics datasets on the farm I/O nodes and then staged to 8mm tape. The data sizes and volumes are summarized in Table 3-1.

Data Type	Size (Kbytes)	Total Volume (Terabytes)	Comments
RAW	130	8.3	
Inclusive DST	190	12	DST includes RAW data
Split DST	190	16	There is a 30% overlap of events on the split DST
Inclusive PAD	32	2	
Split PAD	32	2.7	There is a 30% overlap of events on the split PAD

Table 3-1. Summary of the Run 1b data volume.

There were 27 DST datasets and 39 PAD (PAD - Physics Analysis DST) datasets in size. The DSTs from the main data stream are not heavily used in analysis. Each event is actually stored at least 5 times on permanent media yielding a total data volume for Run I of 41 Terabytes. The information about where a file is located is stored in a experiment specific database which uses FORTRAN indexed files and is kept on FNALD. The primary means of data

storage for Run I was 8mm tape (double density tapes with 5 Gbytes of storage and a maximum I/O rate of 450 Kbytes/second). Selected datasets were further reduced and stored in an STK tape robot which had an initial capacity of 1 Terabyte and has recently been upgraded to 3 Terabytes. This system is accessed via the FATMEN catalog system (a CERN product) and an automatic staging system - users do not need to know which tape the data is stored on, only the filename. The central UNIX and VMS systems also have about 500 Gbytes of disk devoted to physics datasets. There are over 200 Gbytes of disks in the staging pool for the STK robot. There are also significant disk resources (about 600 Gbytes) attached to desktop systems. Copies of selected datasets were made for distribution to remote institutions. In Run Ib about 17,000 8mm tape copies were made. About 3600 of these were kept onsite at Fermilab for use by physicists in the CDF Portakamp complex and the rest were sent offsite. The software environment uses FORTRAN as the primary programming language with limited use of C in system level applications. A mix of experiment developed applications, Fermilab Computing Division products and CERN products are used in the software development and analysis. The code is presently supported on VAX/ALPHA VMS, SGI UNIX and IBM AIX platforms.

CHAPTER 4.

Data Analysis

We start the analysis by looking into the single lepton trigger dataset. Here we reconstruct events according to standard cuts to enhance the presence of a D^* and an opposite side lepton for each event. There are several steps followed in this analysis, i.e. :

- Reconstructing the $c\tau_{B^0}$. This involves the reconstruction of
  1. the B^0 momentum
  2. the B^0 decay length
- Finding the backgrounds.
- Determining the sample composition.
- Comparing the $c\tau_B$ distribution of the data and Monte Carlo events.
- Making and testing the fitting function to extract the ΔM_d value from the asymmetry distribution.
- Fitting the asymmetry distribution

We will now discuss each of the above items in turn.

The decay channel is inclusive. The momenta and energy of the other tracks accompanying the reconstructed D^* are not considered so we do not have the exact values of the B^0 momentum and vertex position. We found a way to estimate the B^0 momentum and vertex position in order to reconstruct the $c\tau_B$. The B^0 momentum is estimated by using the measured D^0 momentum and a Monte Carlo - derived correction factor. The decay length of the B^0 is estimated using the measured decay length from the primary vertex to the D^0 vertex (L_{xy})

and the calculated average decay length of the D^0 ($< L_{xy_D} >$). The $c\tau_B$ can then be calculated from the estimated B^0 momentum and decay length.

The next step is to investigate the types of backgrounds with which we are dealing. There are several different backgrounds contaminating the sample. The most important backgrounds are the combinatoric, the $c\bar{c}$ and the charged B backgrounds. The combinatoric background comes from the random combinations of tracks which pass the D^* cuts. This background constitutes the fake D^*'s in the signal region. It contributes to both like sign and unlike sign events. A $c\bar{c}$ process could give rise to a D^* and a lepton on the opposite side. This background contributes to unlike sign events. A charged B might yield a D^{**} which then decays to a D^*. This contributes to like sign events. Electrons from photon conversions are handled by applying standard conversion rejection procedures.

A pion or kaon track that showers early in the calorimeter could fake an electron. A neutral pion in the proximity of a charged track could shower in the calorimeter, faking an electron. A proton could fake a positron. A pion or a kaon that reaches the muon chambers (CMU and CMP) could fake a muon, which is called punch through background. A muon could come from a kaon decay or a pion decay instead of coming from a B meson. This background is called decay-in-flight background. It is found that the rate of fake leptons accompanying a real D^* is very small. The lepton in our signal region could come from a sequential process instead of coming from a direct B decay process. The number of sequential background events can be estimated from Monte Carlo. The lepton could also come from a B^0 that has mixed. The rate of this occurence can be estimated using the average mixing rate from the particle data book. These backgrounds dilute the amplitude of the oscillation or the asymmetry distribution. Comparing the measured dilution with the expected dilution can also give an alternate estimate of these backgrounds.

Now that we know that the combinatoric, the $c\bar{c}$ and the charged B are the most important backgrounds, we proceed to the next step, i.e. the sample composition determination, where we determine the rate of these backgrounds in our signal region. The number of combinatoric backgrounds can be easily estimated from the mass plot fit. The number of $c\bar{c}$ background events can be

estimated by fitting the PTREL distribution. The number of D^*'s coming from charged B can be estimated from Monte Carlo. The fake lepton rate study leads us to believe that the rate of fake leptons associated with real D^*'s is negligible. The measured rate of the dilution ($0.64\pm^{0.15}_{0.14}$) compared to the expected dilution rate (0.67) due to sequential and mixing processes further indicates that the fake lepton rate is small.

As a cross check of our sample composition results, we can compare the $c\tau$ distribution of the data with the corresponding distribution from Monte Carlo. For the data, the like sign $c\tau$ distribution in the signal region is corrected by the estimated number of combinatoric background events. The unlike sign $c\tau$ distribution in the signal region is corrected by the estimated number of combinatoric and $c\bar{c}$ background events.

Knowing the composition of the sample, we can then proceed to construct the fitting function to extract the value of ΔM_d from the asymmetry distribution. The fitting function contains the shapes of the signal and background components. We tested the fitting function on tens of thousands of BGEN Monte Carlo events and on millions of toy Monte Carlo events with different fractions of each background. When we fit the data, the fractions of the background components in the fitting function are fixed to the values resulting from the sample composition determination.

This chapter is divided into several sections. The first section describes the experimental method used in the analysis. In the second section, we give the definition of the asymmetry distribution; the focus of our mixing observation. Here, we talk about the various backgrounds and their effects. In the third section, we discuss the kinematic cuts to obtain the data. In this section we also give the definition of MDIF and PTREL, the quantities that will be used in the sample composition determination (section five). The fourth section explains the problems associated with constructing the B life time ($c\tau_B$) and the techniques adopted to overcome these problems. We need the $c\tau_B$ distributions to construct the asymmetry function. The fifth section contains the details of the sample composition determination process; the crucial stage of the analysis. The results of this process are used to isolate the signal. As a consistency check, we show the comparison between the experimental data and Monte Carlo

generated distributions in the sixth section. In the seventh section, we show the details of the fitting function used to fit the asymmetry distribution. Here, we explain how we tested the fitting function with Monte Carlo generated events. The final section of this chapter describes how we handle the backgrounds.

A. D^* *lepton* Experimental Method

To observe a time dependent oscillation and to do a mixing measurement one needs to determine the flavor of the B_d^0 at production time and at decay time. For this purpose we use the D^* *lepton* channel. The decay channel of interest on one side (referred to as the near side) is

$$B_d^0 \rightarrow \ D^{*-} X \rightarrow \ \bar{D}^0 \ \pi^- \\ \hookrightarrow K^+ \ \pi^-$$

and the charge conjugate of this chain. On the other side, which we refer to as the away side, the decay of interest is

$$B \rightarrow \ lepton \ \ X$$

where X is inclusive. The away side lepton charge is used to tag the flavor of the B_d^0 at production while the sign of the D^* is used to tag the flavor of the B_d^0 at decay time. If there's no mixing and no cascade decay ($b \rightarrow c \rightarrow$ *lepton*), then the charge of the lepton on the away side and of the D^* will be of like sign. If the B^0 that decays into D^* mixes then the charge of the D^* and the lepton on the away side will be of unlike sign.

$$B^0 \ \rightarrow \ \bar{B}^0 \rightarrow D^{*+} X$$
$$\bar{B} \ \rightarrow \ l^- X$$

A $D^{*-}\ l^-$ or $D^{*+}\ l^+$ pair is called like-sign and tags an unmixed event. A $D^{*+}\ l^-$ or $D^{*-}\ l^+$ pair is called unlike sign and tags a mixed event.

B. Asymmetry and Backgrounds

If N^l is the number of like sign events and N^u is the number of unlike sign (opposite sign) events, then one can define a charge correlation function (asymmetry function) A(t) :

$$\begin{aligned} A(t) &= \frac{N^l(t) - N^u(t)}{N^l(t) + N^u(t)} \\ &= \frac{Prob(B^0 \to B^0) - Prob(B^0 \to \bar{B}^0)}{Prob(B^0 \to B^0) + Prob(B^0 \to \bar{B}^0)} \\ &= \cos\left(\frac{x\,t}{\tau}\right) \end{aligned} \tag{4-1}$$

In the ideal case of perfect charge tagging and no background present, this quantity would oscillate between +1 and -1 with a frequency $\Delta M = \frac{x}{\tau}$. In practice this behavior is modified due to several reasons. The B^0 momentum is not fully reconstructed and the proper decay time in general cannot be calculated from the decay length L. The $D^\star$ vertex in reality cannot be reconstructed with appropriate precision since the slow π (soft pion), from the decay $D^\star \to D^0\,\pi^+$ is almost parallel to D^0. In some fraction of the events, the lepton or $D^\star$ charge does not correctly tag the B^0 state. The lepton on the opposite side could come from a sequential (cascade) $B \to D \to lepton$ decay, which would make an unmixed case appear as a mixed case and vice versa. The lepton could also come from a B^0 which has mixed; in this case it has the same effect as a sequential decay. Some $D^\star$ can come from the virtual W in the B decay, in which case the sign of the $D^\star$ will be opposite to that of the $D^\star$ coming directly from the B. These mistags reduce the observable amplitude of the oscillations.

Some $D^\star$ can also come from $B^\pm$ instead of B^0. Most will come from the following decay chains :

$$B^+ \to D^{\star -} X \tag{4-2}$$

$$\begin{aligned} B^+ &\to \bar{D}^{\star\star 0} X \\ &\hookrightarrow D^{\star -} X \end{aligned} \tag{4-3}$$

which contribute to the fraction of unmixed events. B_s^0 can produce $D^\star$ as well,

through the following channels :

$$B_s^0 \rightarrow D^{\star -} X \tag{4-4}$$

$$B_s^0 \rightarrow D_s^{\star\star -} X \tag{4-5}$$
$$\hookrightarrow D^{\star -} X$$

In this case, since B_s^0 can also mix, it can then contribute to both mixed and unmixed fraction.

The most important background affecting the distribution at short life-times comes from $D^\star$ decaying directly from $c\bar{c}$ initial states, which contributes to mixed events. For example the c quark could combine with a $\bar{d}$ quark from $d\bar{d}$ out of vacuum, producing a D^+ or D^0 which then decays semileptonically giving a positively charged lepton. The $\bar{c}$ quark may combine with the d quark forming a $D^{\star -}$. The lepton $D^\star$ pair produced by this event will be of opposite sign, thus mimicking a mixed event.

$$\begin{aligned} c &\rightarrow D^+ \rightarrow l^+ X \\ \bar{c} &\rightarrow D^{\star -} \end{aligned} \tag{4-6}$$

This effect contaminates the B^0 distribution only at short life-times since the D life-time is short compared to the B life-time. Since, $c\bar{c}$ contributes to the unlike sign distribution, the effect on the asymmetry function can be seen as the distortion of the cosine function into something like a sine function depending on the amount of this background. The more $c\bar{c}$ we have, the deeper is the dip at short life times.

And finally we have contaminations arising from conversion electrons, fake leptons and combinatorial background of the $D^\star$ reconstruction. In these latter cases, there should be no significant charge correlation between the lepton and the $D^\star$ sides since they should in principle contribute equally to both like sign and unlike sign fractions. Some of these backgrounds can be efficiently reduced by cuts on the transverse momentum of the lepton and $D^\star$ and by cuts on impact parameter significance of the kaon and pion tracks coming from the D^0 decay.

C. Kinematic Quantities and Event Selection

We use standard lepton ID cuts on the single lepton trigger dataset for our signal in order to reduce the background due to fake leptons. We do not require the lepton tracks to have a hit in the SVX detector since we do not need the accuracy of vertexing. We only use the leptons for flavor tagging, thus we do not have to lose statistics by requiring SVX tracks for the leptons. However for the kaon and pion tracks, since we need the vertexing accuracy to measure the D^0 vertex, we impose SVX track requirement. We also use the most important standard MDIF cut to enhance the D^* peak and suppress the combinatoric background. MDIF is the difference between the reconstructed mass of the $K\pi\pi_{soft}$ system and the reconstructed mass of the $K\pi$ system subtracted by the Particle Data Group value of the difference between the mass of $D^{*\pm}$ and the mass of the D^0

$$MDIF \equiv (M_{K\pi\pi} - M_{K\pi}) - (M_{D^*} - M_{D^0}) \tag{4-7}$$

This is a very powerful cut to get rid of the combinatoric background, due to the fact that the decay $D^{*+} \rightarrow D^0\ \pi^+$ has a small available kinetic energy for its decay products. We expect the MDIF quantity distribution for the signal as defined above to center around zero.

PTREL is the component of the lepton momentum transverse to the B jet direction from which it comes. This quantity can be used to distinguish between a lepton coming from a $c\bar{c}$ event and a lepton coming from a $b\bar{b}$ event. In general, a lepton coming from a $b\bar{b}$ event tend to be stiffer (have a larger PTREL) than that coming from a $c\bar{c}$ event. However we are not using this quantity as a cut to suppress the $c\bar{c}$ background since the distribution of the $b\bar{b}$ lepton PTREL overlaps significantly with that of the $c\bar{c}$ lepton PTREL. We are using this PTREL quantity in a fitting procedure to find the fraction of $c\bar{c}$ events in our sample. This is possible since the PTREL distributions of leptons coming from direct $b\bar{b}$, sequential $b\bar{b}$ and $c\bar{c}$ events are distinguishable from each other.

Also the impact parameter significance cut on kaon and pion tracks cleans the sample from those underlying tracks close to the primary vertex. This reduces the combinatoric background significantly especially for the muon sample.

Those cuts leading to the final data sample are numerous and are tabulated in Appendix A.

D. B Decay Length Reconstruction Method

The asymmetry quantity $A(t)$ provides a convenient aid to observe and measure the time dependent mixing phenomena. Since this quantity is defined as a function of the $c\tau_B$, we have to be able to determine $c\tau_B$ for each event. $c\tau_B$ is related to L_{xy_B} as follow :

$$c\tau_B = L_{xy_B} * (M_B/P_{t_B}) \tag{4-8}$$

Figure 4-1 shows the relationship between the L_{xy}, the distance between the D^0 decay vertex and the primary vertex projected onto a plane transverse to the beam direction, and L_{xy_B} and L_{xy_D}, the projected decay length of the B^0 and the D^0 respectively. However, the decay channel of interest is inclusive and there are missing tracks involved. So the B^0 vertex and momentum cannot be reconstructed with great accuracy. Hence, the decay length of the B^0, i.e. the two dimensional distance from the primary vertex to the B^0 vertex and the transverse momentum of the B^0 have to be approximated. We can estimate P_{t_B} from the measured $P_{t_{D^0}}$ using a kinematical correction factor (CORRF). CORRF gives the ratio of $P_{t_{D^0}}/P_{t_{B^0}}$ as a function of the transverse momentum of the D^0. This function is obtained from a Monte Carlo study using the generated (GENP bank) information of the D^0 and B^0. The GENP bank contains the true kinematical information on the generated particles. Figure 4-2 shows CORRF (black triangles) and its error (white triangles) as a function of $P_{t_{D^0}}$. A best fit to the Monte Carlo data of CORRF as a function of $P_{t_{K\pi}}$is given by :

$$CORRF = 0.1630 + 0.03998\, P_{t_{K\pi}} - 0.1349 \times 10^{-2}({P_{t_{K\pi}}}^2) + 0.1922 \times 10^{-4}({P_{t_{K\pi}}}^3). \tag{4-9}$$

Using CORRF we can estimate P_{t_B}.

$$P_{t_B} = P_{t_D}/CORRF \tag{4-10}$$

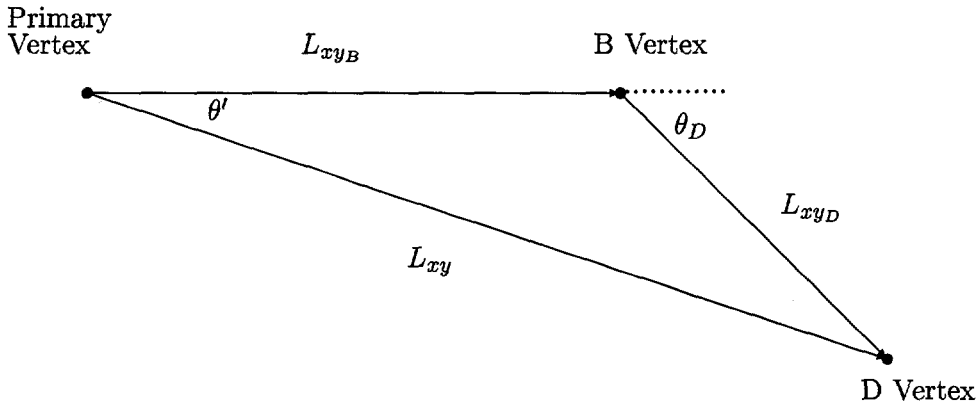

Figure 4-1. The primary vertex, B vertex and D vertex on the near side. L_{xy} is a measured quantity. L_{xy_B} is estimated from L_{xy} and the calculated average value of L_{xy_D}.

Three methods of approximating the B^0 decay length were considered :

- Using L_{xy}
- Using $L_{xy} - (0.01244 * P_{t_{K\pi}}/1.8646)$
- Using $L_{xy} - < L_{xy_D} >$

The first method is just using the measured total decay length, i.e. the 2 dimensional distance from the primary vertex to the D^0 decay vertex. The second method approximates the B^0 decay length by subtracting the total decay length with the average 2 dimensional decay length of the D^0 which is calculated using $P_{t_{K\pi}}$, the measured transverse momentum of the K and π tracks [1] and the Particle Data Group (PDG) value of $c\tau_{D^0} = 124.4\,\mu m$ and $M_{D^0} = 1.8646\,GeV/c^2$. The third method[21] uses $< L_{xy_D} >$, the calculated average 2 dimensional decay length of the reconstructed D^0. Here the calculation of the D^0 decay length uses the measured value of L_{xy} as a constraint, thereby guaranteeing the value of $< L_{xy_D} >$ to not exceed that of L_{xy}. It is mostly due to this feature, as Fig. 4-3 shows, that we decided to adopt method 3 for this analysis. Figure 4-3 shows the difference between generated and estimated L_{xy_B} for Method 3(a) and for Method 2(b) as a function of L_{xy_B}. This figure clearly shows the advantage of Method 3 having a constraint on L_{xy_D}. The L_{xy} resolution of method 3 is shown in Fig. 4-4. The derivation of $< L_{xy_D} >$ can be seen in Appendix B.

The corresponding $c\tau$ (the lifetime in cm) of method 3 for approximating the B^0 decay length is given by the following equation :

$$
\begin{aligned}
c\tau &= (L_{xy} - < L_{xy_D} >) * (5.279/P_{t_{K\pi}}) * CORRF && \text{(4-11)} \\
< L_{xy_D} > &= L_{xy}/(1 - exp(a * L_{xy}/P_{t_{K\pi}})) + P_{t_{K\pi}}/a && \text{(4-12)} \\
a &= 149.89 - 117.6 * CORRF
\end{aligned}
$$

In this $c\tau_B$ reconstruction method we have neglected the angle θ_D between the decay path of the B^0 and the decay path of the D^0 which is justifiable for the region of $P_{t_{K\pi}}$ we are dealing with, i.e. $P_{t_{K\pi}} > 2\,GeV/c$.

[1] Here we use $P_{t_{K\pi}}$ as P_{t_D}.

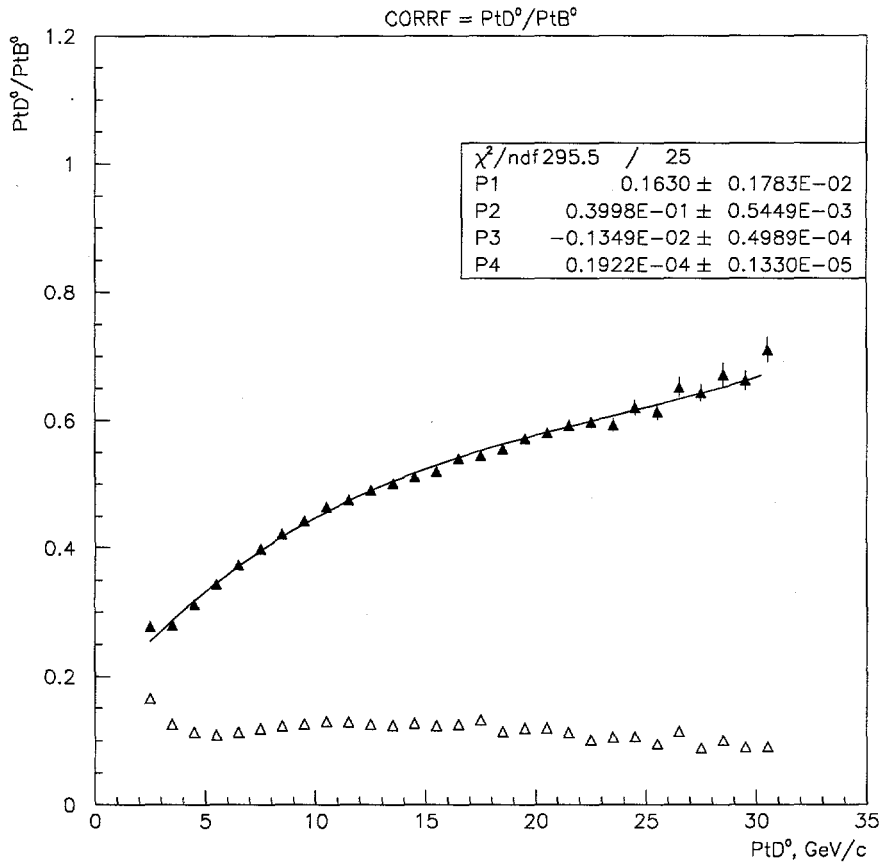

Figure 4-2. Kinematic correction factor P_{t_D}/P_{t_B} (CORRF) as a function of P_{t_D} and its error. Each black triangle represents the mean value of CORRF distribution in each bin of $P_{t_D^0}$, and the white triangle represents the error of the mean value of the distribution (RMS/$\sqrt{entries}$).

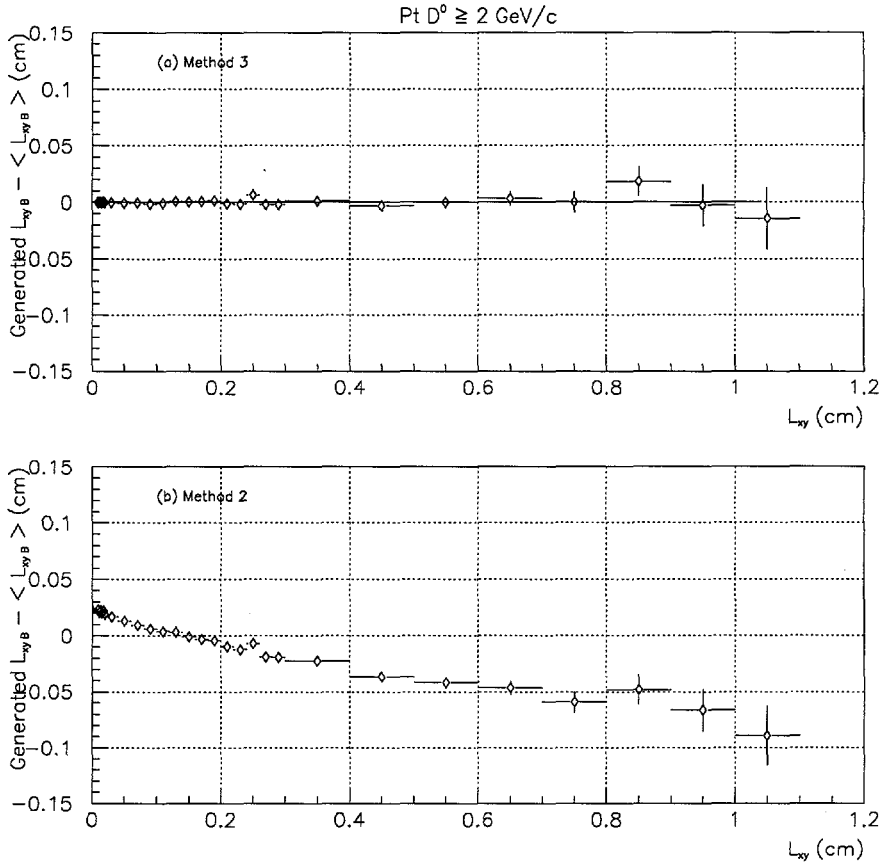

Figure 4-3. The difference between the generated and estimated L_{xy_B} and its RMS for Method 3 (a) and for Method 2 (b) as a function of L_{xy_B}.

Figure 4-5 and Fig. 4-6 show the result of the Monte Carlo study on the cosine of this angle, which is close to unity. Figure 4-7 and Fig. 4-8 show the Monte Carlo result for the cosine of the angle between L_{xy} and L_{xy_B}. Throughout this note, unless otherwise stated, we are using cm as the unit of length and GeV as the unit of energy in all the plots. Applying simple trigonometry on Fig. 4-1, we can see that

$$L_{xy_B} = L_{xy} \cos\theta' - L_{xy_D} \cos\theta_D \tag{4-13}$$

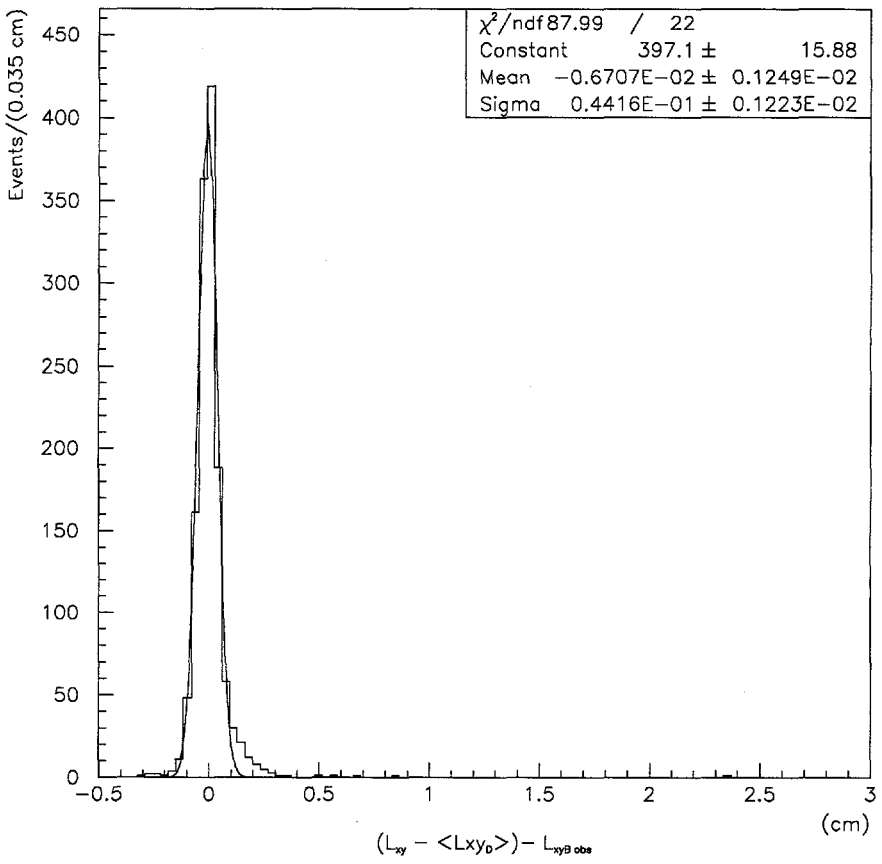

Figure 4-4. L_{xy} resolution of Method 3. The unit of X-axis is cm.

The Monte Carlo result justifies the following equation :

$$L_{xy_B} = L_{xy} - L_{xy_D} \tag{4-14}$$

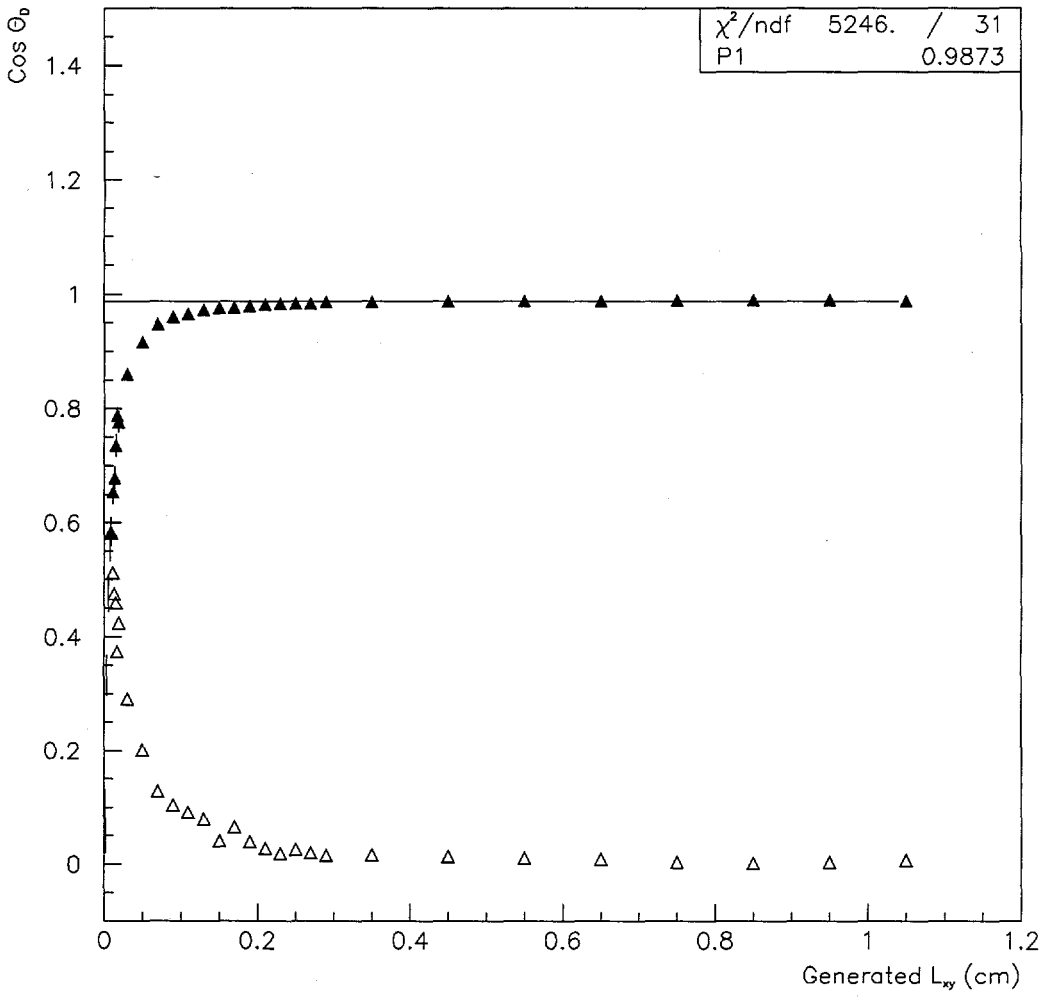

Figure 4-5. cos θ_D. Black triangles are the mean values and the white triangles are the errors of the mean.

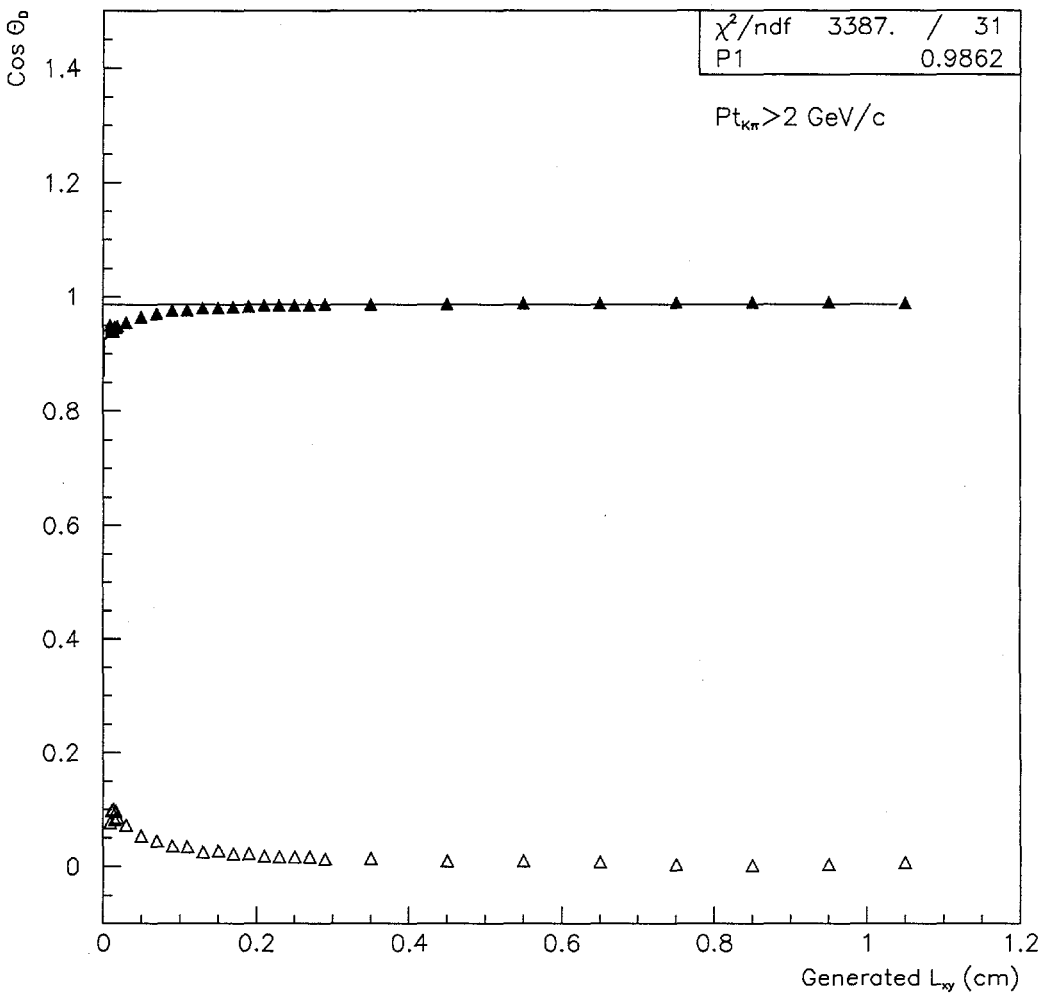

Figure 4-6. cos θ_D with $P_{t_{K\pi}} > 2GeV/c$. Black triangles are the mean values and the white triangles are the errors of the mean.

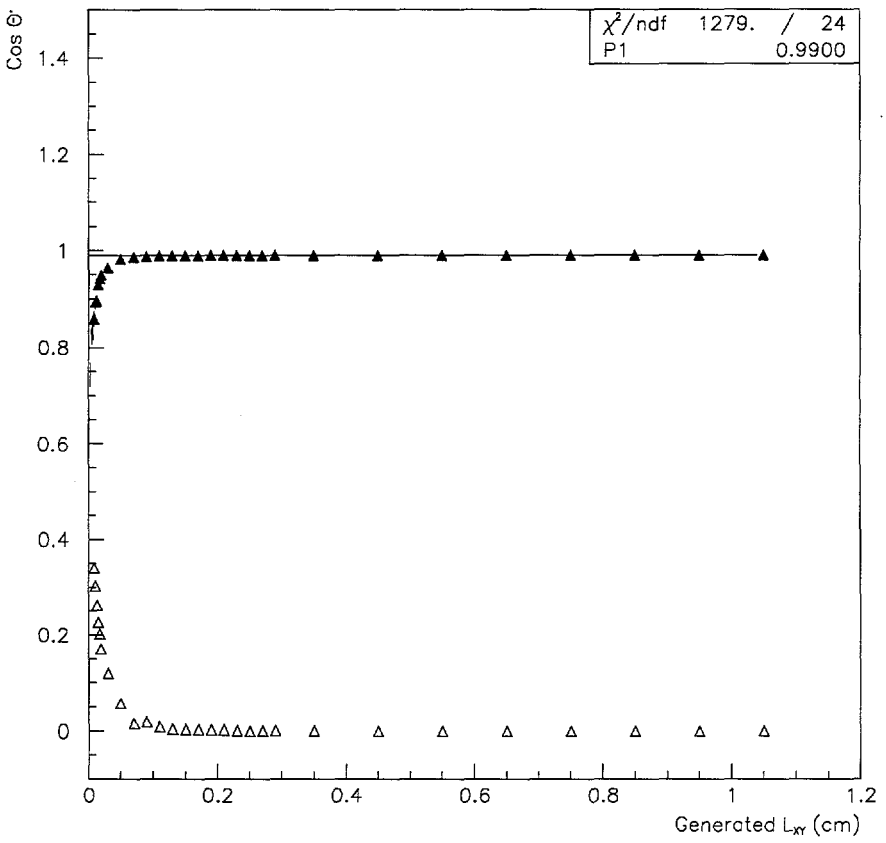

Figure 4-7. cos θ'. Black triangles are the mean values and the white triangles are the errors of the mean.

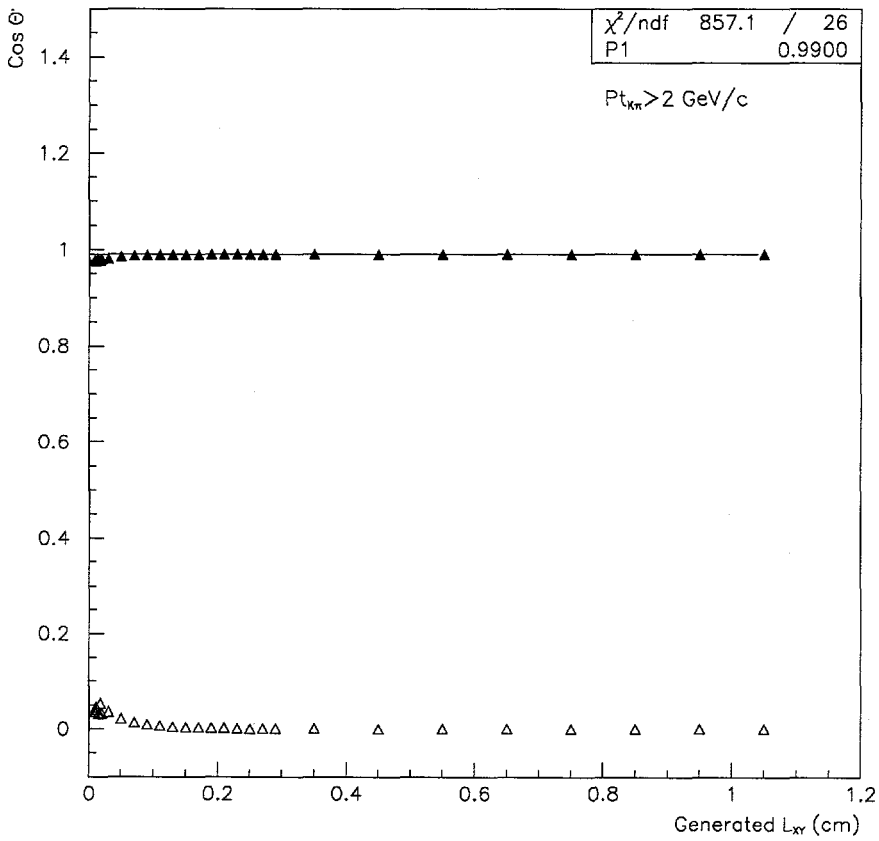

Figure 4-8. $\cos\theta'$ with $P_{t_{K\pi}} > 2GeV/c$. Black triangles are the mean values and the white triangles are the errors of the mean.

E. Sample Composition Determination

We investigate the various sources of lepton and $D^{\star}$ that contribute to the data sample in order to correct for various background contaminations. To achieve this goal, we make use of the MDIF distribution and the PTREL distribution of our sample.

1. MDIF Distribution

The fraction of combinatoric background (fake $D^{\star}$) in the signal region can be estimated using the MDIF plot. The MDIF distribution, taken in the region of $\mid MDIF \mid < 0.008\ GeV/c^2$, is fitted with a gaussian function for the signal and with a threshold function $N_0\ (x - x_0)^P$ to represent the background. N_0 is a normalization constant and x_0 is an offset. Figure 4-9 shows the MDIF distribution for the total like sign sample of Run 1A and Run 1B for both the e and μ. We use this plot to determine the width of the gaussian for the like sign MDIF signal. The MDIF distribution for the total unlike sign sample of Run 1A and Run 1B e and μ is shown in Fig. 4-10. This plot is used to determine the width of the gaussian for the unlike sign MDIF signal. The MDIF distribution for the like sign electron and unlike sign electron samples are shown separately in Fig. 4-11 a and b, respectively. The MDIF background distribution profile looks similar for like sign and unlike sign. So to increase statistic we combine the like sign and unlike sign distribution for the sideband region. The MDIF distribution for the lower sideband region of $M_{K\pi}$ mass, i.e. $1.80 < M_{K\pi} < 1.84\ GeV/c^2$ and for the upper sideband region, i.e. $1.89 < M_{K\pi} < 1.95\ GeV/c^2$ are shown respectively in Fig. 4-11 c and d. Since we do not see any signal in these sideband regions, we can conclude that we do not have real soft pion reconstructed with fake D^0 in the sideband region of $M_{K\pi}$ mass. Figure 4-12 presents plots identical to Fig. 4-11 except the data being presented are for muon sample.

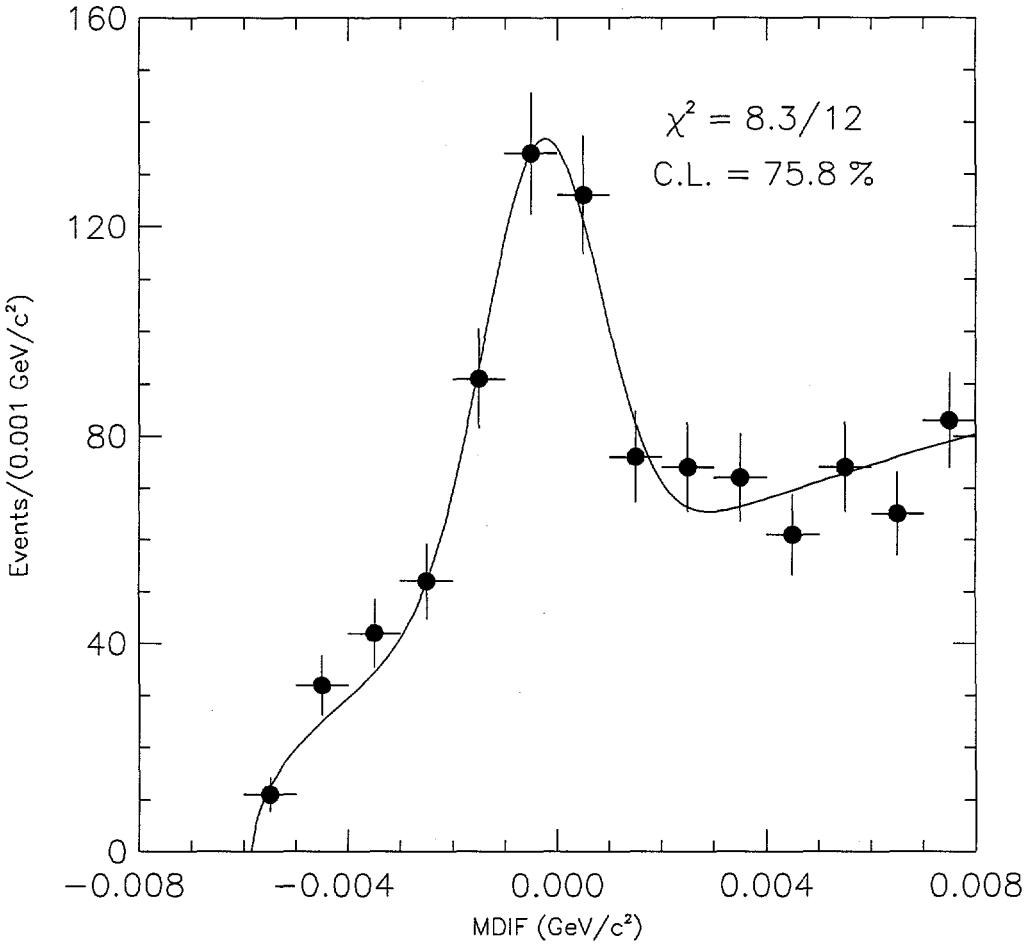

Figure 4-9. MDIF distribution for the like sign Run 1a and 1b e and μ sample fitted with a gaussian for the signal and threshold function for the background.

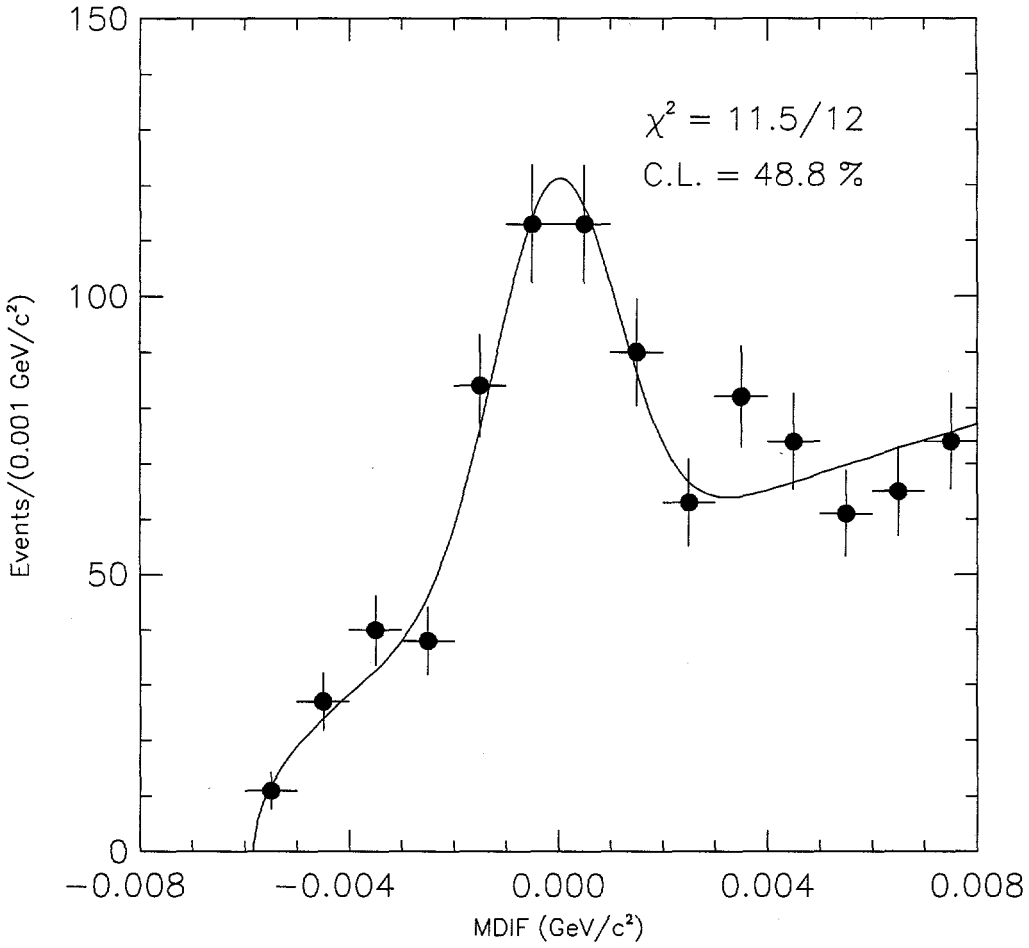

Figure 4-10. MDIF distribution for the unlike sign Run 1a and 1b e and μ sample fitted with a gaussian for the signal and threshold function for the background.

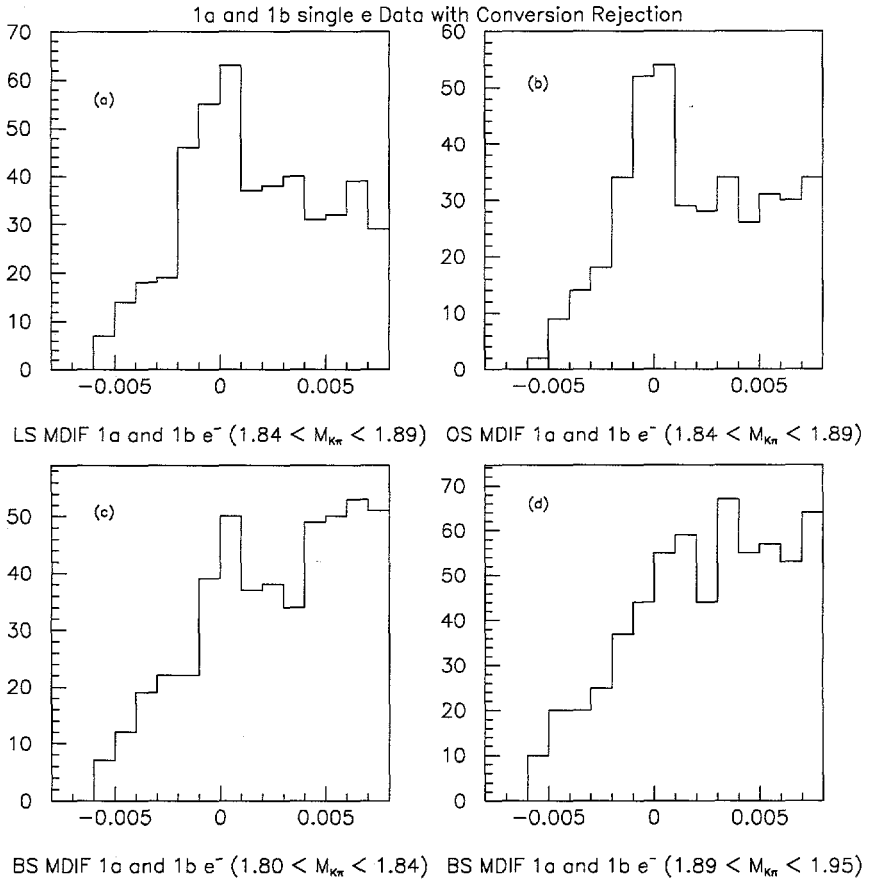

Figure 4-11. Run 1a and 1b e sample. (a)MDIF plot of the like sign sample, (b)MDIF plot of the unlike sign sample, (c)MDIF plot of the both sign sample in the lower sideband region of $M_{K\pi}$, (d)MDIF plot of the both sign sample in the upper sideband region of $M_{K\pi}$.

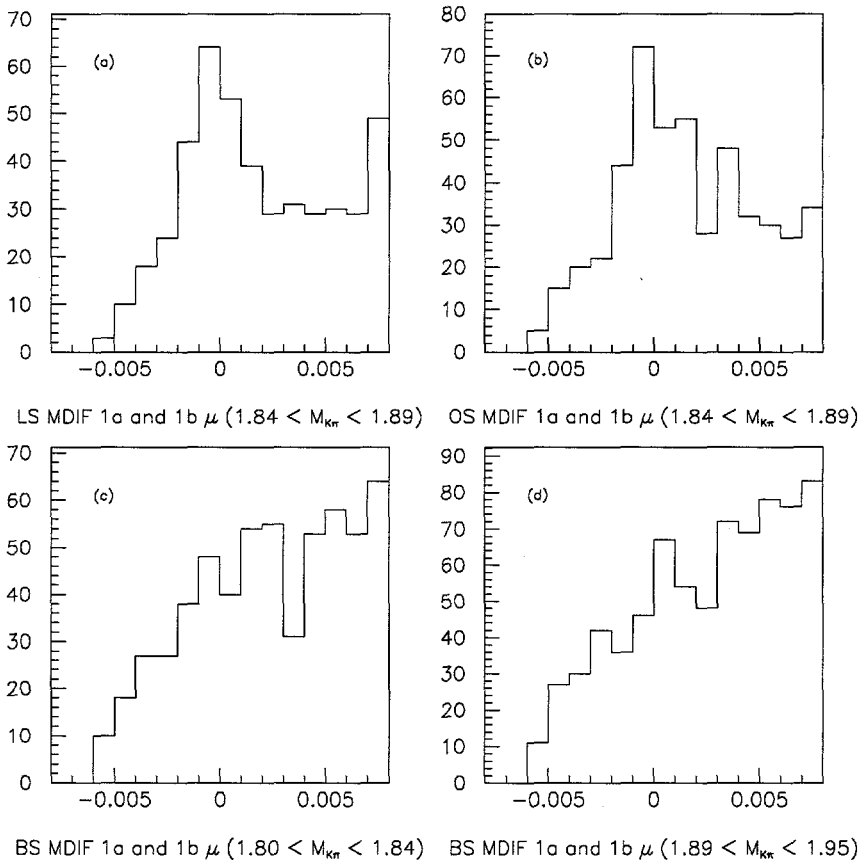

Figure 4-12. Run 1a and 1b μ sample. (a)MDIF plot of the like sign sample, (b)MDIF plot of the unlike sign sample, (c)MDIF plot of the both sign sample in the lower sideband region of $M_{K\pi}$, (d)MDIF plot of the both sign sample in the upper sideband region of $M_{K\pi}$.

2. Lepton PTREL Distribution

A method for studying the background function corresponding to $c\bar{c}$ production and decay to a lepton and $D^{\star}$ is to investigate the lepton PTREL distribution. The PTREL distribution of the unlike sign sample is fitted with the function for $b\bar{b}$ lepton, the function for $c\bar{c}$ lepton and the function for lepton in the sideband region of MDIF plot. In order to do this fit, we have to know the shape or parametrization of these functions.

To make a PTREL function template for the combinatoric background we take the normalized PTREL distribution in the MDIF sideband region, i.e. $-0.008 < MDIF < -0.002$ and $0.002 < MDIF < 0.008$. This normalized distribution is then fitted with a function $[P_4 + P_1(x - P_5) + P_2(x - P_5)^2]exp(P_3 x)$. The distribution is checked to be similar for like sign and for unlike sign. In order to improve our statistics, we combine the like sign and unlike sign data. The combinatoric PTREL function for electrons is shown in Fig. 4-13 while the same function for muons is shown in Fig. 4-14. The template for Run 1A direct $b\bar{b}$ electrons, sequential $b\bar{b}$ electrons and $c\bar{c}$ electrons can be seen in Figs. 4-16, 4-15 and 4-19 respectively. For Run 1B, they are shown in Figs. 4-18, 4-17 and 4-20. Similar distributions for Run 1A muons can be observed in Figs. 4-28, 4-27 and 4-25 while for Run 1B muons they are shown in Figs. 4-30, 4-29 and 4-26. From this MC study we determine the relative fraction of direct and sequential electrons, summarized in Table 4-1. This relative fraction is visually shown by the comparison between the PTREL profile for direct and for sequential electrons in Fig. 4-21. For muons it is shown in Fig. 4-23. A three dimensional scatter plot as a function of P_t of sequential electons versus P_t of direct electrons is shown in Fig. 4-22. The same plot for muon is shown in Fig. 4-24. From these 3 dimensional scatter plots it is clear that above the 6 GeV/c P_t^{lepton} cutoff, we have only a small fraction of sequentials remaining.

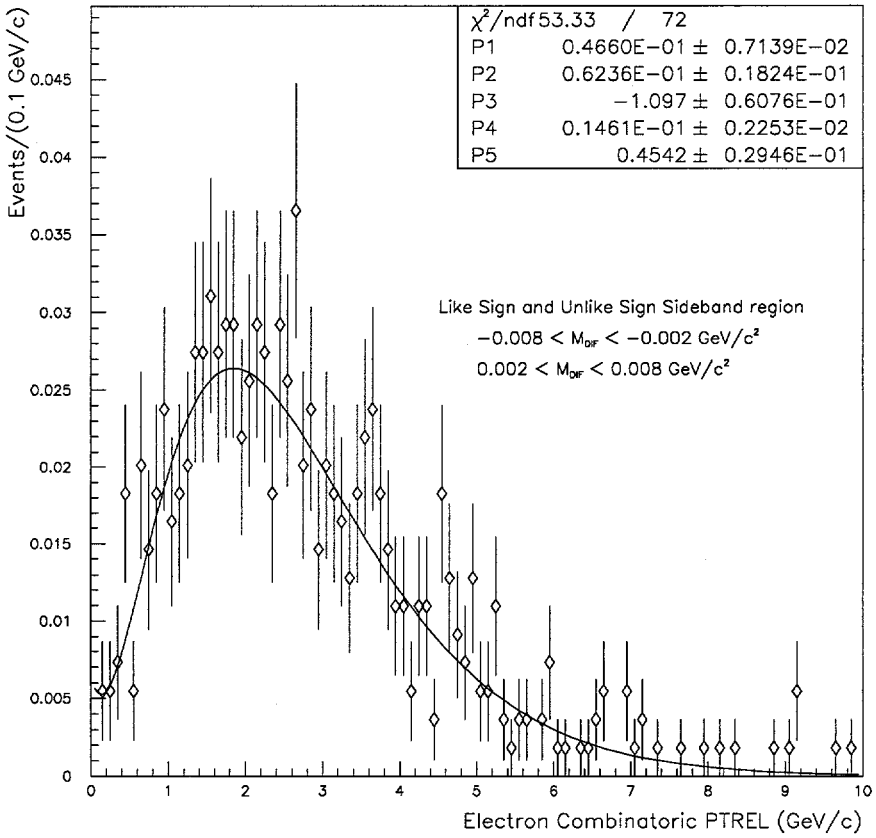

Figure 4-13. Normalized electron PTREL distribution in the MDIF sideband region fitted with a $[P_4 + P_1(x - P_5) + P_2(x - P_5)^2]exp(P_3 x)$ function. An SVX fit is required for each electron track.

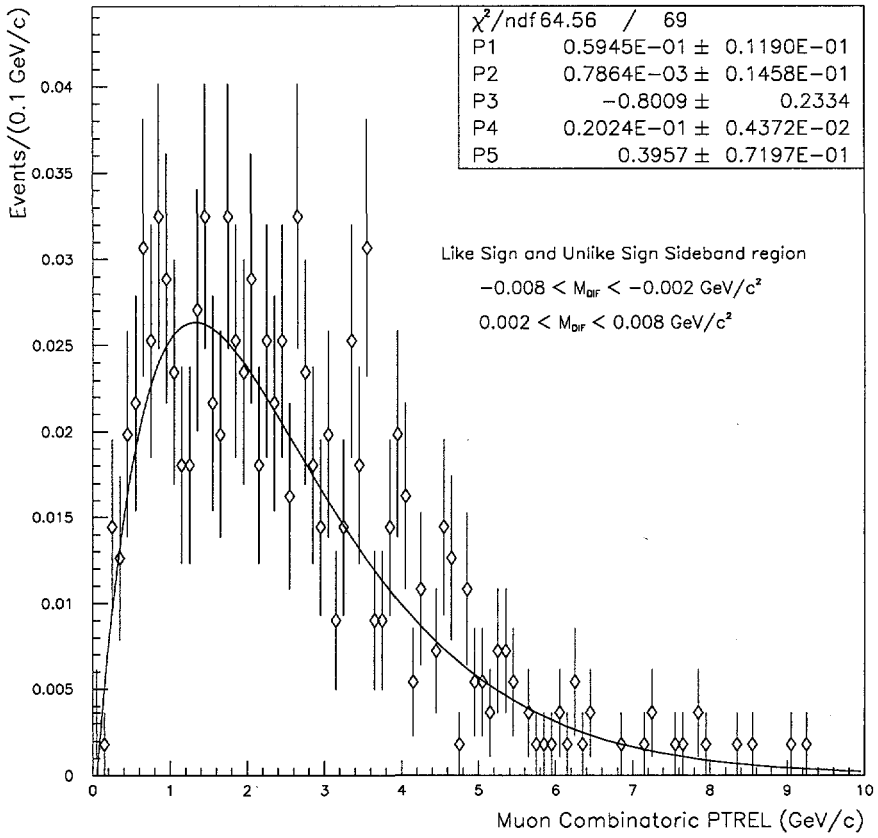

Figure 4-14. Normalized muon PTREL distribution in the MDIF sideband region fitted with a $[P_4 + P_1(x - P_5) + P_2(x - P_5)^2]exp(P_3 x)$ function. An SVX fit is required for each muon track.

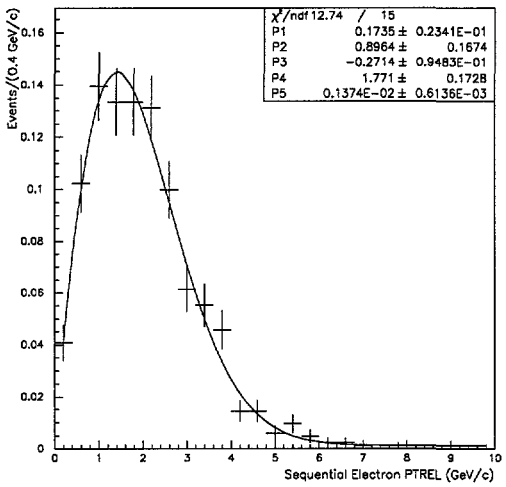

Figure 4-15. Normalized PTREL distribution for Run 1A sequential electrons fitted with $P_1\, x^{P_2}\, exp(P_3\, x^{P_4}) + P_5$.

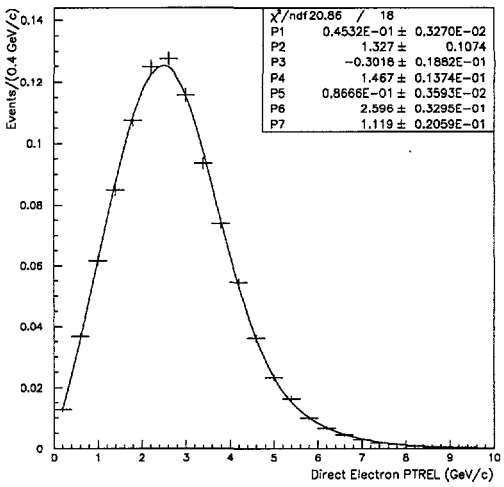

Figure 4-16. Normalized PTREL distribution
for Run 1A direct electrons fitted with $P_1\, x^{P_2}\, exp(P_3\, x^{P_4}) + \frac{P_5}{P_7}\, exp(-((x - P_6)/P_7)^2/2)$.

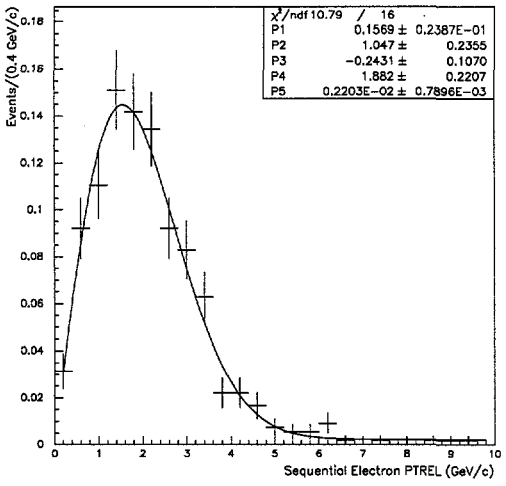

Figure 4-17. Normalized PTREL distribution for Run 1B sequential electrons fitted with $P_1\, x^{P_2}\, exp(P_3\, x^{P_4}) + P_5$.

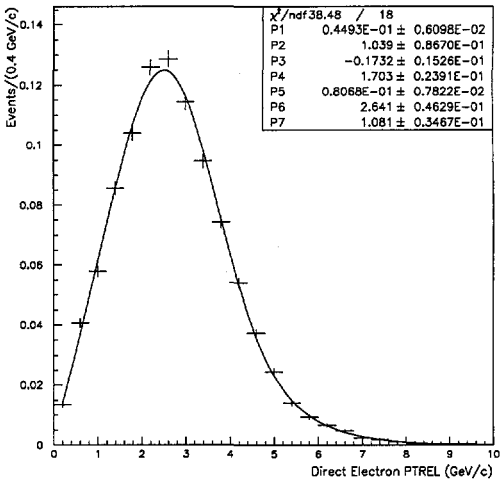

Figure 4-18. Normalized PTREL distribution
for Run 1B direct electrons fitted with $P_1\, x^{P_2}\, exp(P_3\, x^{P_4}) + \frac{P_5}{P_7}\, exp(-((x - P_6)/P_7)^2/2)$.

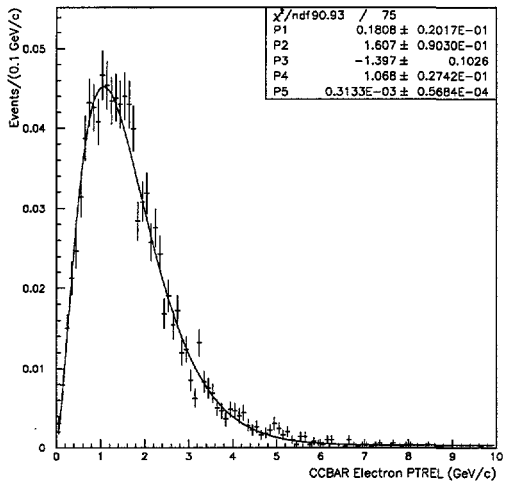

Figure 4-19. Normalized PTREL distribution for Run 1A $c\bar{c}$ electrons fitted with $P_1\, x^{P_2}\, exp(P_3\, x^{P_4}) + P_5$.

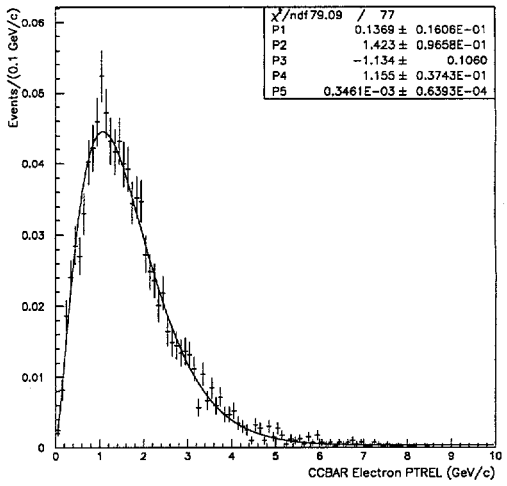

Figure 4-20. Normalized PTREL distribution for Run 1B $c\bar{c}$ electrons fitted with $P_1\, x^{P_2}\, exp(P_3\, x^{P_4}) + P_5$.

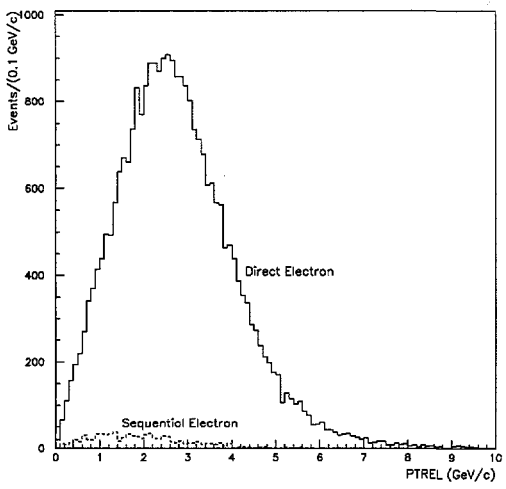

Figure 4-21. Solid curve is the PTREL profile of direct electrons, while the superimposed dashed curve is that of sequential electrons.

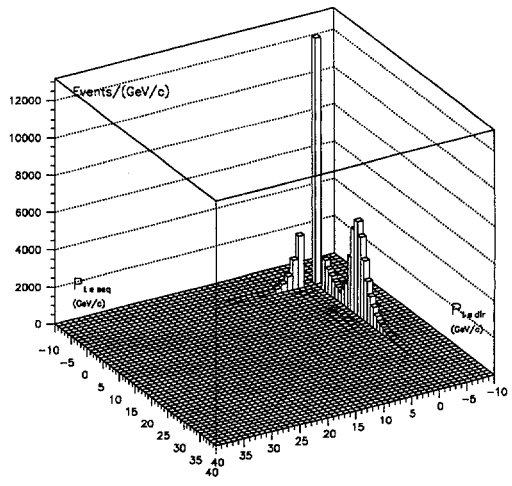

Figure 4-22. 3 dimensional scatter plot of P_t of sequential electrons and P_t of direct electrons. Notice that above $P_{t_{cutoff}} \approx 6\,GeV/c$ there is a very little amount of sequentials passing the trigger cutoff.

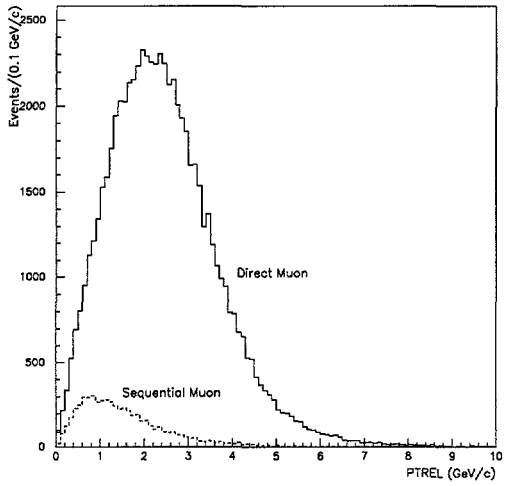

Figure 4-23. Solid curve is the PTREL profile of direct muons, while the superimposed dashed curve is that of sequential muons.

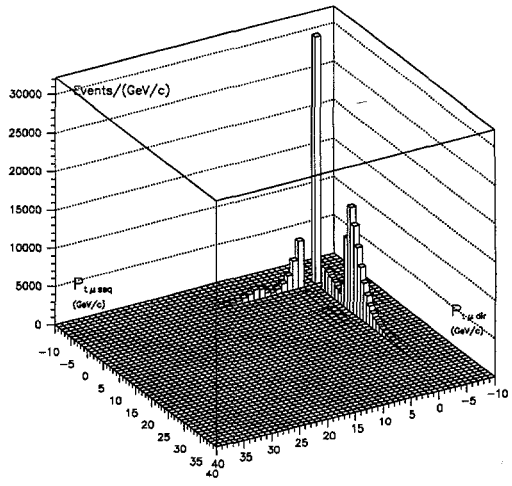

Figure 4-24. 3 dimensional scatter plot of P_t of sequential μ's and P_t of direct μ's. Notice that above $P_{t_{cutoff}} \approx 6\,GeV/c$ there is a very little amount of sequentials passing the trigger cutoff.

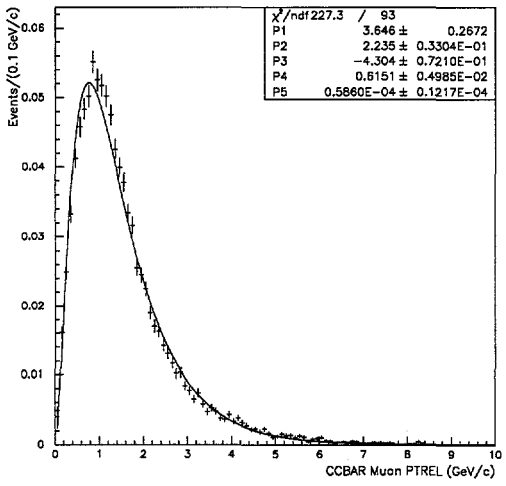

Figure 4-25. Normalized PTREL distribution for Run 1A $c\bar{c}$ μ's fitted with $P_1\, x^{P_2}\, exp(P_3\, x^{P_4}) + P_5$ function.

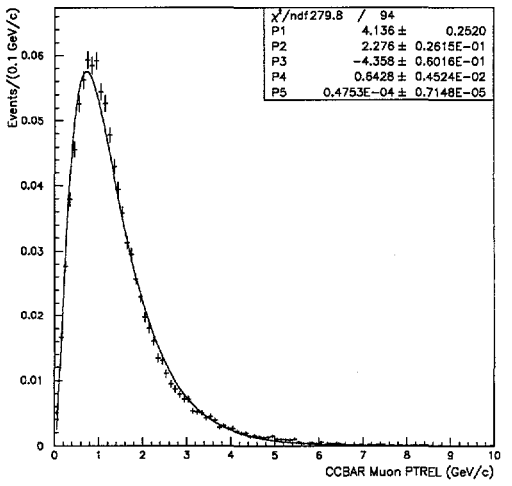

Figure 4-26. Normalized PTREL distribution for Run 1B $c\bar{c}$ μ's fitted with $P_1\, x^{P_2}\, exp(P_3\, x^{P_4}) + P_5$ function.

Figure 4-31 shows the PTREL distribution of electrons from $b\bar{b}$, $c\bar{c}$ and the combinatoric backgrounds superimposed on one another. Figure 4-32 shows the PTREL distribution of muons from $b\bar{b}$, $c\bar{c}$ and the combinatoric background. We can see that in general the PTREL of a $c\bar{c}$ lepton is softer than a $b\bar{b}$ lepton.

	f^r_{dir}	f^r_{seq}
Run 1A e^-	$97.10 \pm 0.10\%$	$2.90 \pm 0.10\%$
Run 1B e^-	$97.17 \pm 0.12\%$	$2.83 \pm 0.12\%$
Run 1A μ	$92.11 \pm 0.10\%$	$7.89 \pm 0.10\%$
Run 1B μ	$93.36 \pm 0.14\%$	$6.64 \pm 0.14\%$

Table 4-1. Relative fraction of direct and sequential leptons.

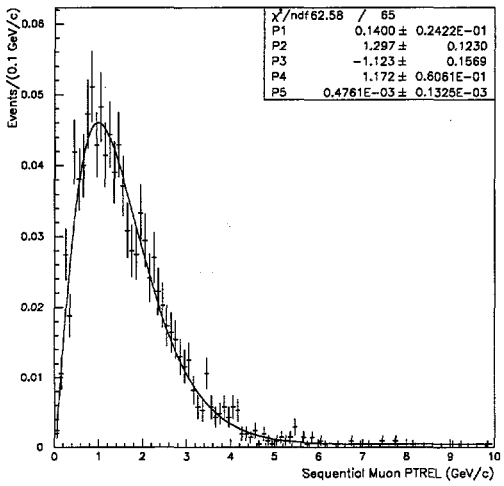

Figure 4-27. Normalized PTREL distribution for Run 1A sequential μ's fitted with $P_1\, x^{P_2}\, exp(P_3\, x^{P_4}) + P_5$ function.

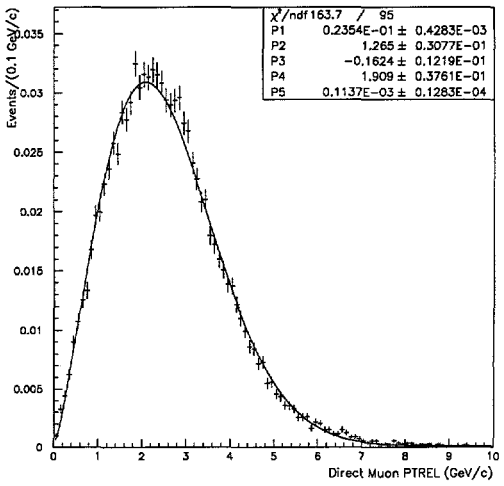

Figure 4-28. Normalized PTREL distribution for Run 1A direct μ's fitted with $P_1\, x^{P_2}\, exp(P_3\, x^{P_4}) + P_5$ function.

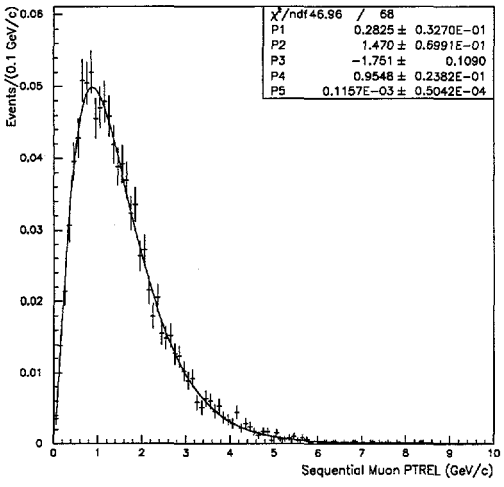

Figure 4-29. Normalized PTREL distribution for Run 1B sequential μ's fitted with $P_1\, x^{P_2}\, exp(P_3\, x^{P_4}) + P_5$ function.

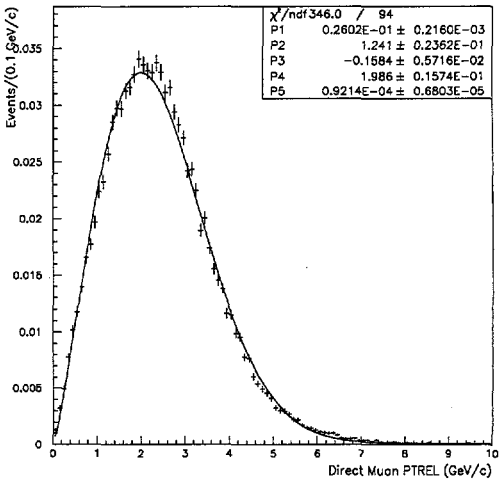

Figure 4-30. Normalized PTREL distribution for Run 1B direct μ's fitted with $P_1\, x^{P_2}\, exp(P_3\, x^{P_4}) + P_5$ function.

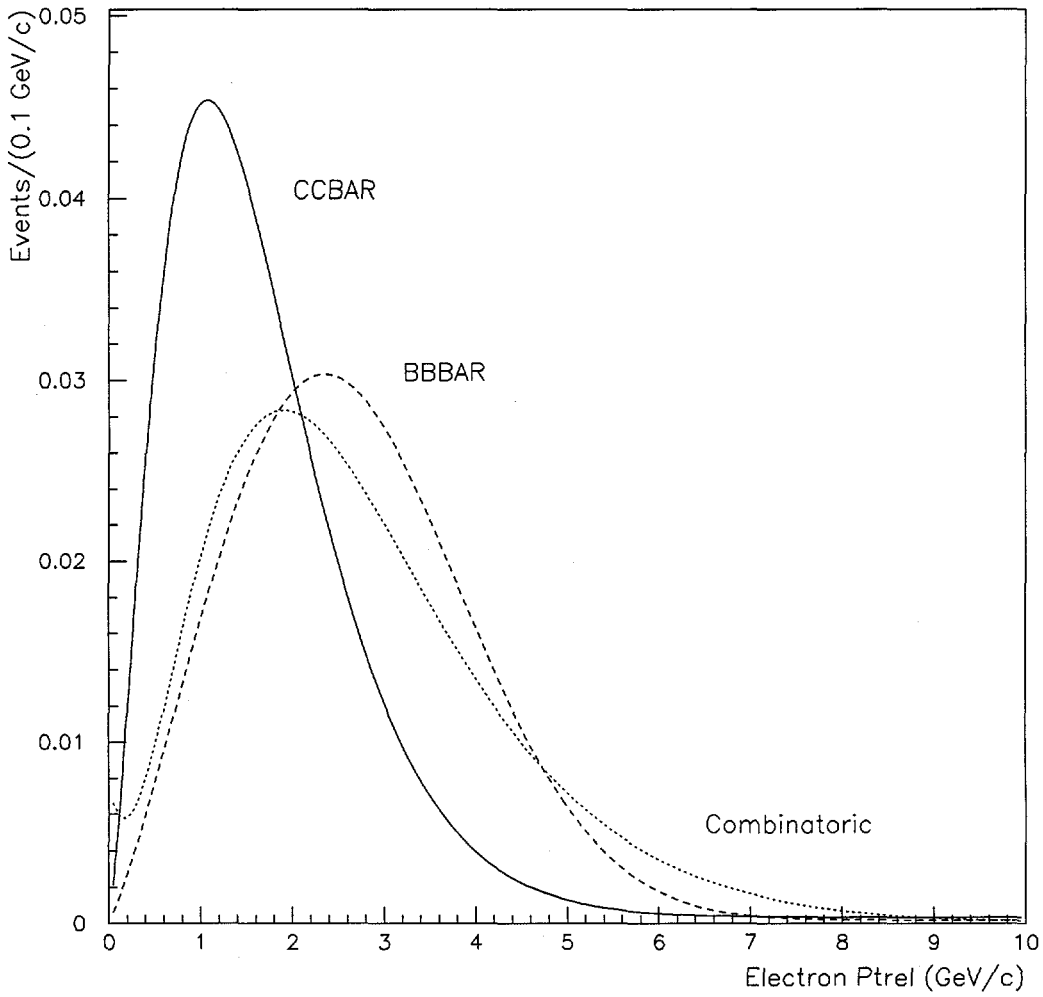

Figure 4-31. PTREL of electrons from $b\bar{b}$, $c\bar{c}$ and combinatoric background superimposed

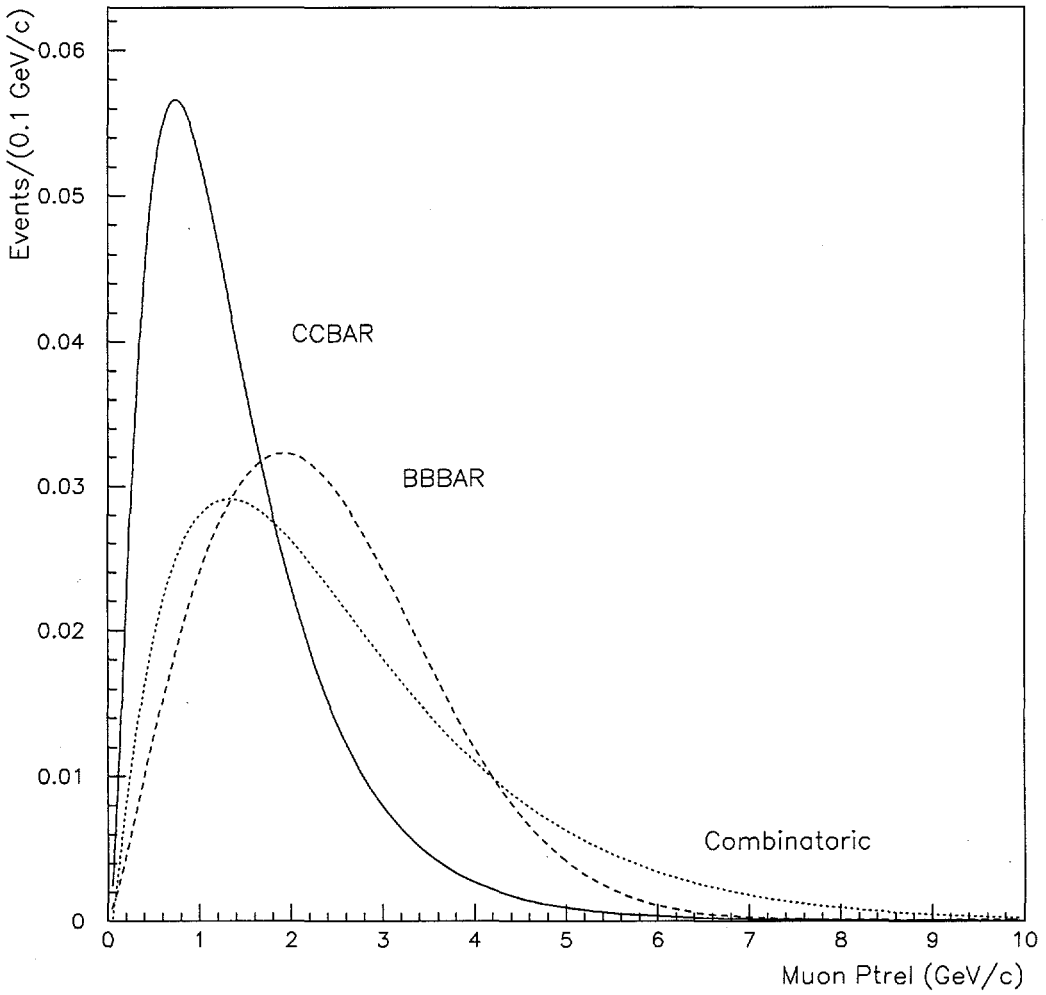

Figure 4-32. PTREL of muons from $b\bar{b}$, $c\bar{c}$ and combinatoric background superimposed

3. Simultaneous Fit of MDIF and PTREL

To improve the accuracy of the PTREL fit and of the MDIF fit, we fit the two distributions simultaneously and constrain parameters where appropriate. In the case of the like sign sample, we constrain the number of $b\bar{b}$ leptons (direct plus sequential) in the PTREL distribution to the area of the gaussian signal in the MDIF distribution. Also, the number of combinatoric background events in the PTREL distribution is constrained to the number of the combinatoric events in the signal region of the MDIF distribution. The simultaneous fit applied to the unlike sign sample proceeds in an identical fashion to the fit described for the like sign sample, with the exception that the $c\bar{c}$ background must be included in the fit. In this case, the area of the gaussian peak now consists of both $b\bar{b}$ and $c\bar{c}$ events. The plots of the fit results are found in Appendix C.

The results of these fits are summarized in Table 4-2. In the table, for each type of lepton, there are two values for $f_{c\bar{c}}$, one in the opposite sign column and one spanning the like sign and opposite column. The first one is the $c\bar{c}$ fraction relative to the unlike sign sample and the second one is the fraction relative to the total (both sign) sample.

e	Like Sign	Unlike Sign
$N_{b\bar{b}}$	99.92 ± 11.69	20.84 ± 18.47
N_{comb}	105.82 ± 6.67	96.22 ± 6.31
$N_{c\bar{c}}$	n/a	43.66 ± 15.05
f_{comb}	$51.4 \pm 4.6\%$	$59.9 \pm 6.1\%$
$f_{c\bar{c}}$	n/a	$27.2 \pm 9.6\%$
f^*_{comb}	$55.1 \pm 3.7\%$	
$f^*_{c\bar{c}}$	$11.9 \pm 4.2\%$	
μ	Like Sign	Unlike Sign
$N_{b\bar{b}}$	104.91 ± 11.86	72.57 ± 21.41
N_{comb}	98.13 ± 6.57	100.88 ± 6.36
$N_{c\bar{c}}$	n/a	48.64 ± 17.65
f_{comb}	$48.3 \pm 4.6\%$	$45.4 \pm 4.0\%$
$f_{c\bar{c}}$	n/a	$21.9 \pm 8.1\%$
f^*_{comb}	$46.8 \pm 3.0\%$	
$f^*_{c\bar{c}}$	$11.4 \pm 4.2\%$	

Table 4-2. Sample composition results from the simultaneous fit on the PTREL and MDIF distribution

4. Sources of Real D^*

The D^*'s considered as signal events in this analysis originate from the decay of B_d^0 mesons. However, other B meson species can decay into a D^* which is then viewed as a contaminant to the signal. A charged B meson can decay into a D^{**0} which can then decay into a D^*. The branching ratio of D^{**0} decaying semileptonically has been measured to be about 0.36. On the other hand, the hadronic decay of D^{**0} to D^* has not been measured. An estimate of the charged B contribution to our D^* signal is obtained from a Monte Carlo study using PYTHIA $v5.7$ with QQ decay to find out the relative fraction of events in the reconstructed D^* signal that come from different B meson species. The ratio of the B meson species yielding real D^*'s, $F_{B_d^0} : F_{B_s^0} : F_{B^\pm} = 0.64 : 0.05 : 0.31$. In order to obtain a realistic estimate of the error on $F_{B^\pm}$ and $F_{B_s^0}$ we have used a result from a closely related CDF analysis [22]. Hence we will use $F_{B^\pm} = 0.31 \pm 0.15$ and $F_{B_s^0} = 0.05 \pm 0.02$.

5. Fake Lepton Rate Determination

A Monte Carlo study was done to estimate the rate of fake electrons and fake muons associated with a reconstructed $D^{\star}$ on the opposite side. This study which does not require the lepton tracks to be SVX tracks, yields a fraction of fake electrons less than 1% at 95% confidence level of fake electron in the electron $D^{\star}$ sample coming from $b\bar{b}$ and $c\bar{c}$. For the muon $D^{\star}$ Monte Carlo sample, the fraction of fake muons is 2% at 95% confidence level. We are aware that the results of this MC study depend on the reliability of the QFL detector simulation package (which is not so clear) to simulate fake leptons.

One can see qualitatively by inspecting the HAD/EM distribution of the electron data that the fake electron contamination of the data is small. HAD/EM is the ratio of energy deposited in the hadronic calorimeter divided by the energy deposited in the electromagnetic calorimeter. The value of this ratio is expected to be small for a real electron. Therefore, it is used as a component of the electron identification cuts. A standard electron cut is $HAD/EM < 0.04$. The HAD/EM distribution of Run 1A and Run 1B electron sample for the raw signal (background unsubtracted signal), combinatoric background (MDIF sideband), and background subtracted signal appear to be consistent with that of a real electron (Fig. 4-33 and 4-34). The figures show that the HAD/EM distribution peaks at very low values. Similar plots for incoming hadrons would show an essentially flat behavior at low values of HAD/EM.

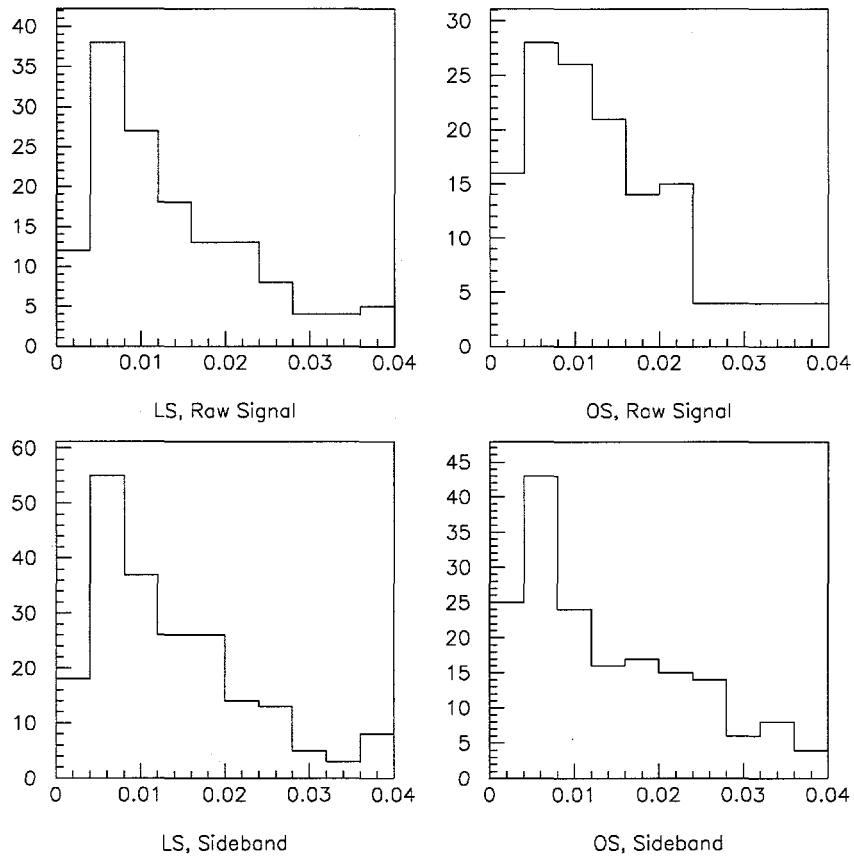

Figure 4-33. HAD/EM distribution for the raw signal and combinatoric background

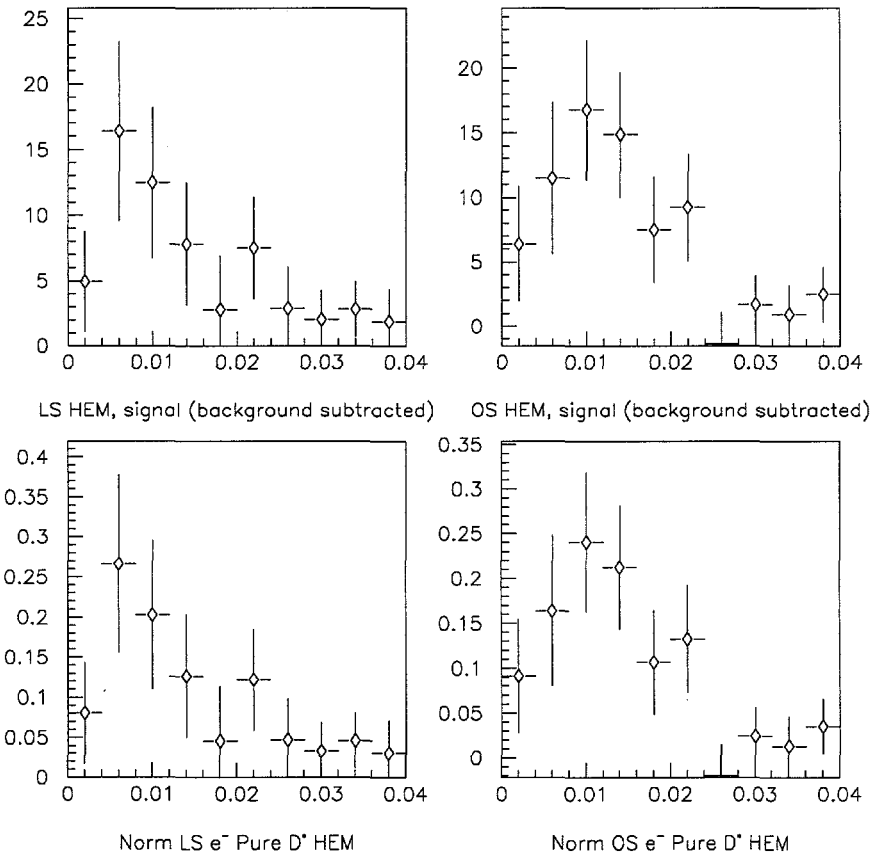

Figure 4-34. HAD/EM distribution for the background subtracted signal

As an additional evidence that the fake lepton background is small, we use a data set in which the selection criteria for electrons and muons have been relaxed. In the case of electrons, we now require that the ratio HAD/EM be large, namely greater than 0.04. For the muons, we only require that the muon candidate be observed in the CMU and merely points towards the CMP without CMP hits. The D^* lepton reconstruction code was run on this fake lepton data sample. Of 8969 fake electron events we are left only with 8 events when we applied the like-sign cuts and 4 events when we applied the unlike-sign cuts. When we release the MDIF cuts in this analysis, we have 302 like-sign events and 318 unlike-sign events. For the 22,259 fake muon events the corresponding numbers are 8 like-sign events and 13 unlike-sign events with the MDIF cut and 869 like-sign and 833 unlike-sign events without the MDIF cut. One can conclude from this analysis thus far that the fake lepton events will populate the like sign signal and unlike signal equally.

We use these fake lepton samples to obtain the PTREL distribution for the fake electrons and for the fake muons. Figure 4-35 and 4-36 respectively shows the PTREL template for the fake electrons and for the fake muons. These templates are used in the PTREL fits to find the number of fake leptons in our lepton D^* signal. The PTREL fit is done simultaneously for the like-sign and the unlike-sign combinatoric background subtracted sample (real D^*). The number of fake leptons in the like sign sample is constrained to be equal to that in the unlike sign sample. The like sign sample is fitted for the number of $b\bar{b}$ and fake leptons. The unlike sign sample is fitted for the number of $b\bar{b}$, $c\bar{c}$ and fake leptons. Figure 4-37 and 4-38 show the PTREL fit for electron. The PTREL fit for muon is shown in Fig. 4-39 and 4-40. The result of fit is summarized in Table 4-3. The PTREL fit result shows that we have practically no fake leptons in the electron sample and about $1 \pm 7\%$ fake leptons in the muon sample. However, we believe that we can estimate the number of fake leptons better than what the statistically limited PTREL fit is providing us with.

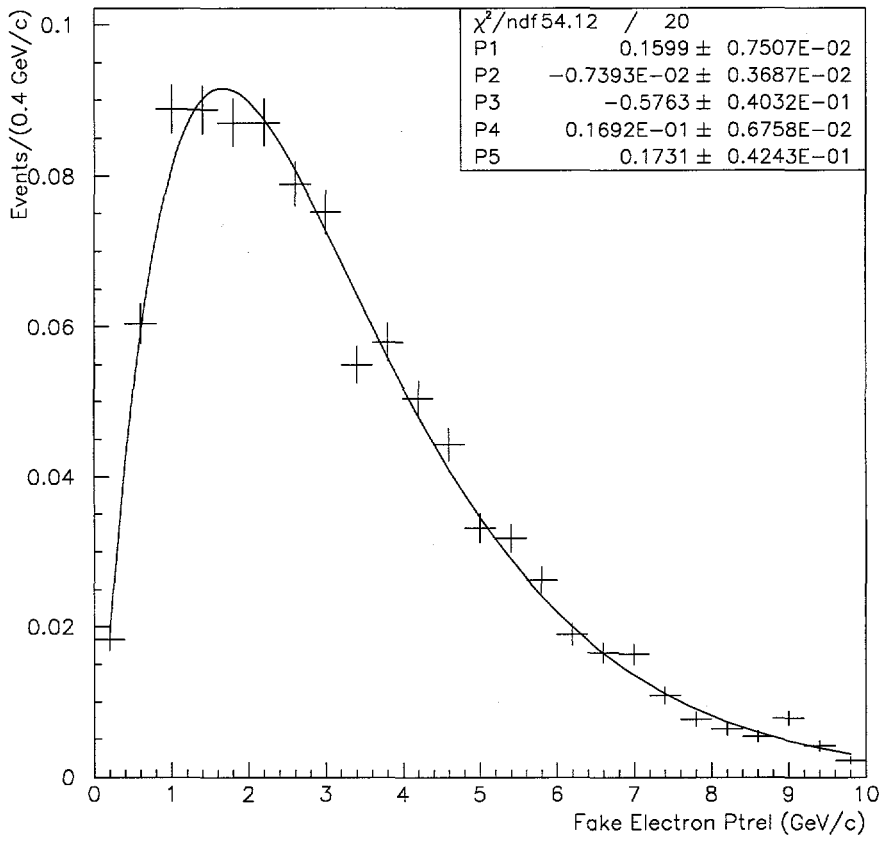

Figure 4-35. Normalized fake electron PTREL distribution parametrized with $[P_4 + P_1(x - P_5) + P_2(x - P_5)^2]exp(P_3x)$ Function.

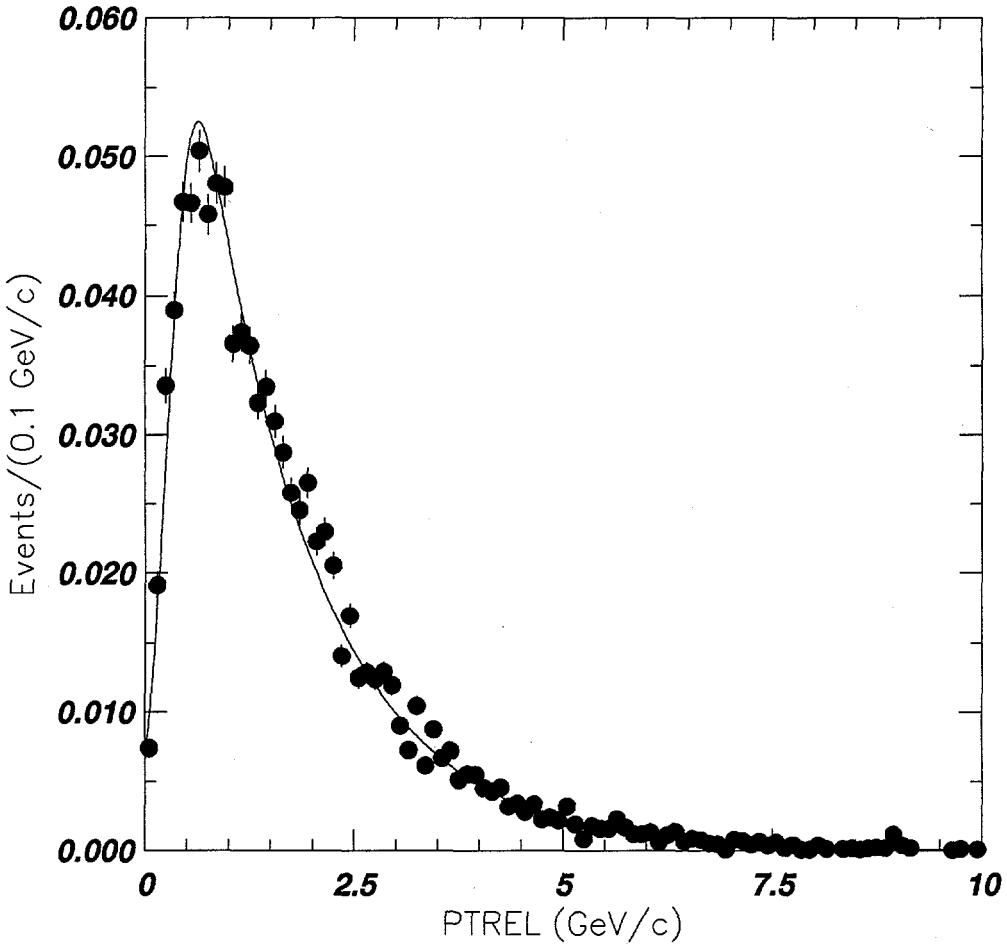

Figure 4-36. Normalized fake μ PTREL distribution parametrized with an exponential and a turn-on function : $[(Norm/ct1) * exp(-x/ct1) * dfreq((x - x0b)/c1b)]$.

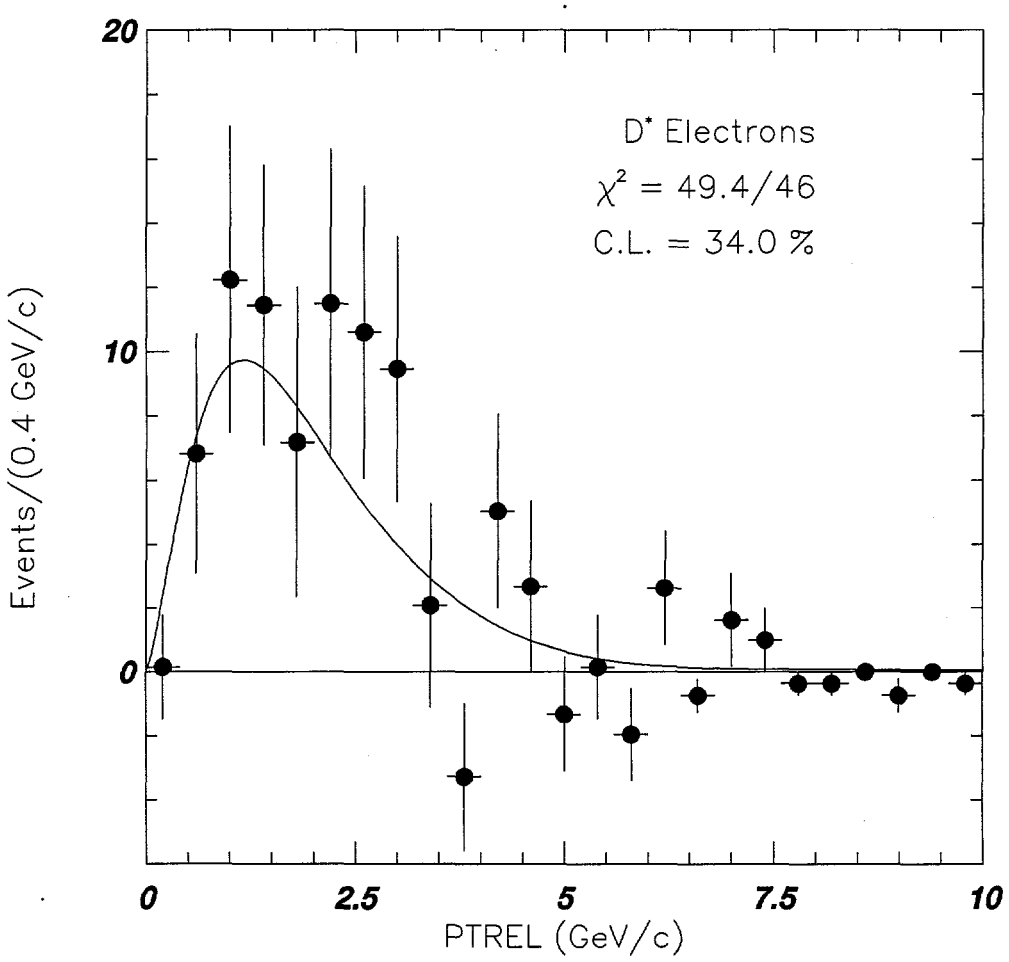

Figure 4-37. PTREL distribution of electrons in the like sign real D^* sample fitted for the fractions of $b\bar{b}$ and fake electrons. This distribution is simultaneously fitted with the PTREL distribution of electrons in the unlike sign real D^* sample. The number of fake e's in the like sign sample is constrained to be the same as the number of fake e's in the unlike sign sample. See Fig. 4-38.

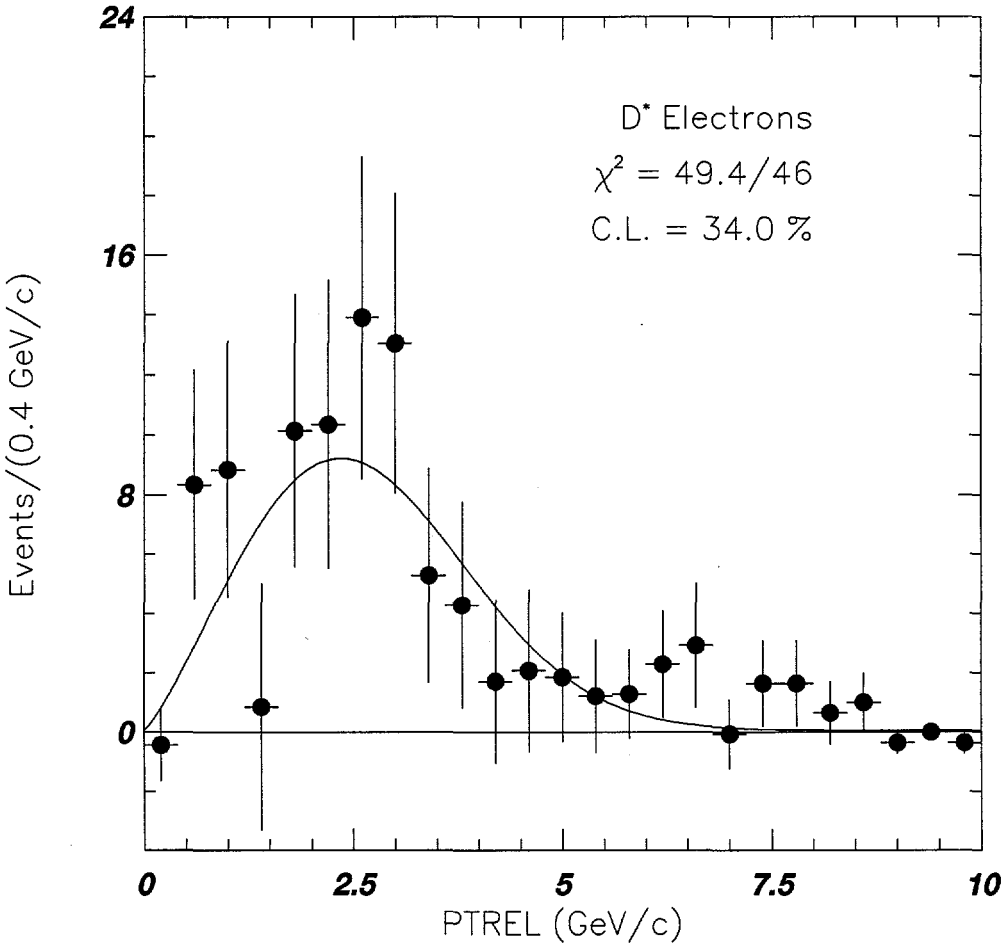

Figure 4-38. PTREL distribution of electrons in the unlike sign real D^* sample fitted for the fractions of $b\bar{b}$, $c\bar{c}$ and fake electrons. This distribution is simultaneously fitted with the PTREL distribution of electrons in the like sign real D^* sample. The number of fake electrons in the unlike sign sample is constrained to be the same as the number of fake electrons in the like sign sample. See Fig. 4-37.

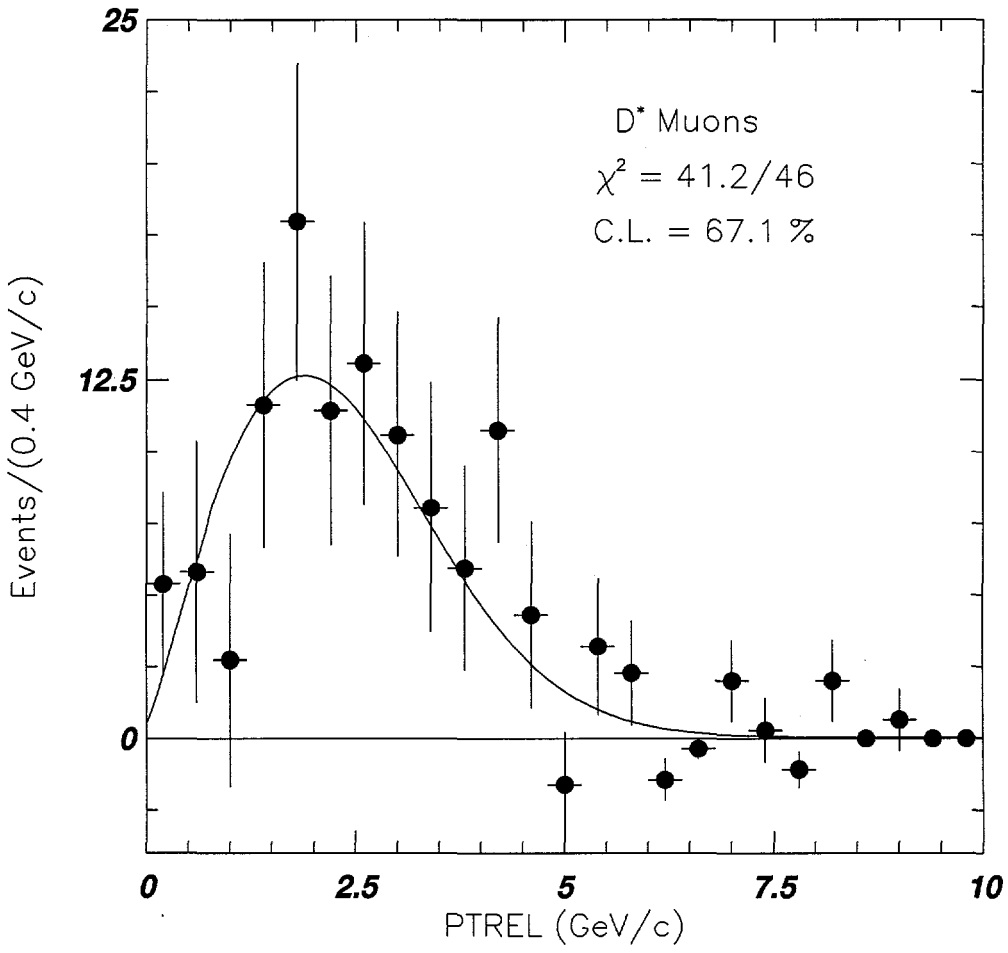

Figure 4-39. PTREL distribution of muons in the like sign real D^* sample fitted for the fractions of $b\bar{b}$ and fake muons. This distribution is simultaneously fitted with the PTREL distribution of muons in the unlike sign real D^* sample. The number of fake muons in the like sign sample is constrained to be the same as the number of fake muons in the unlike sign sample. See Fig. 4-40.

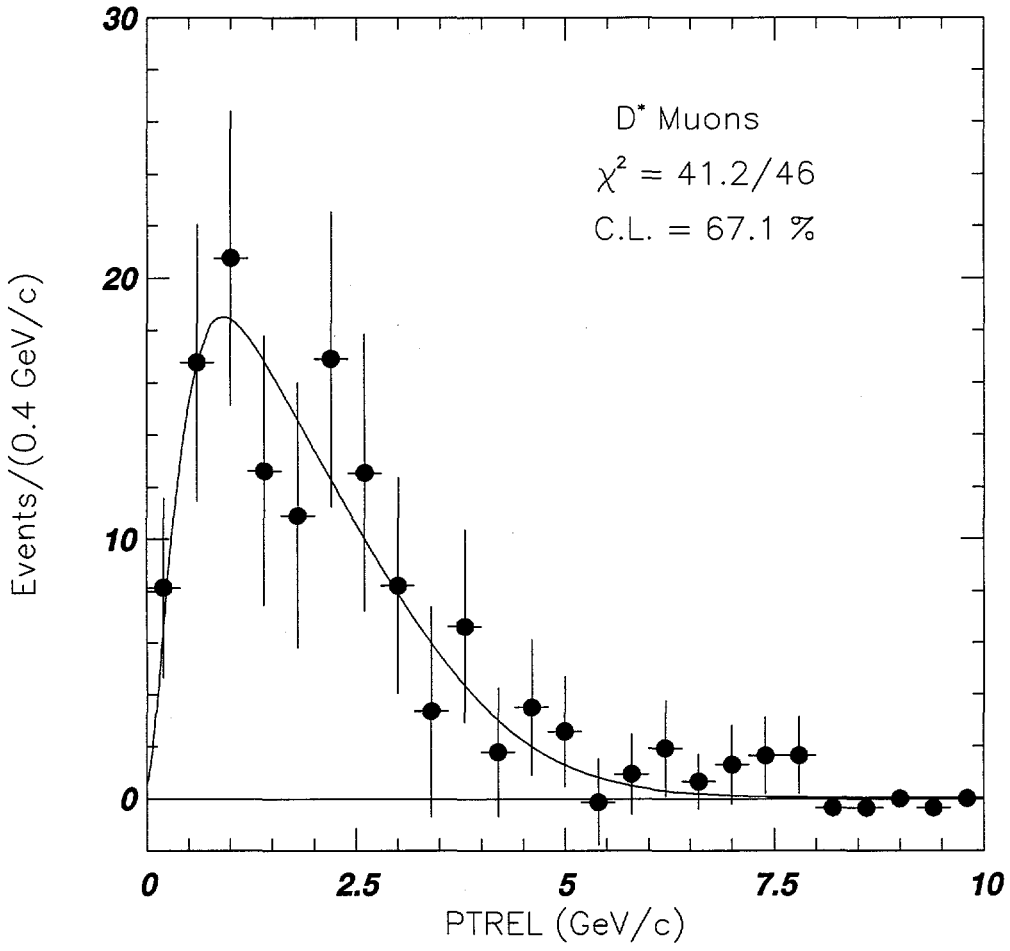

Figure 4-40. PTREL distribution of muons in the unlike sign real D^* sample fitted for the fractions of $b\bar{b}$, $c\bar{c}$ and fake muons. This distribution is simultaneously fitted with the PTREL distribution of muons in the like sign real D^* sample. The number of fake muons in the unlike sign sample is constrained to be the same as the number of fake muons in the like sign sample. See Fig. 4-39.

PTREL Fit	1A+1B LS μ	1A+1B US μ
$N_{b\bar{b}}$	96.05 ± 20.31	62.22 ± 22.07
$N_{c\bar{c}}$	$xxxxx$	56.64 ± 22.90
N_{fake}	2.94 ± 15.78	2.94 ± 15.78
$f_{b\bar{b}}$	$72.7 \pm 19.4\%$	
$f_{c\bar{c}}$	$26.0 \pm 11.6\%$	
f_{fake}	$1.4 \pm 7.3\%$	
PTREL Fit	1A+1B LS e	1A+1B US e
$N_{b\bar{b}}$	76.08 ± 13.96	15.56 ± 17.75
$N_{c\bar{c}}$	$xxxxx$	47.18 ± 16.46
N_{fake}	0 ± 0.01	0 ± 0.01
$f_{b\bar{b}}$	$66.0 \pm 21.0\%$	
$f_{c\bar{c}}$	$34.0 \pm 13.7\%$	
f_{fake}	$0 \pm 0\%$	

Table 4-3. Result of the simultaneous fit on the LS (like sign) and US (unlike sign) PTREL distribution to find the number of fake leptons in Run 1A+1B μ and e data sample with the combinatoric background subtracted out. The number of $c\bar{c}$ is fixed to zero in the LS sample while the number of fake leptons in the LS sample is constrained to be the same as the number of fake leptons in the US sample.

Fake muon events are mainly due to decay-in-flight and punch-through pions and kaons. The punch-through events are due to pions and kaons that managed to make it through the various steel absorbers to the CMU and CMP detectors without interacting. The punch-through tracks have to traverse 5.5 pion absorption lengths to get to the CMU and 8 pion absorption lengths to get to the CMP, corresponding to a punch-through probability of 3×10^{-4} and about 5×10^{-3} for pions and kaons respectively, to reach the CMP. We shall see later that these rates are small compared to decay in flight.

The decay-in-flight (DIF) backgrounds are basically those muons coming from $K \rightarrow \mu\,\nu$ and $\pi \rightarrow \mu\,\nu$. It is clear that the DIF fraction is associated with the decay of a pion or kaon while travelling between the production point and the CMU. The CMU is located about 3.5 meters away from the beam pipe. The boost factor γ for 6 GeV/c pion is 43 and for kaon it is 12. Pions and kaons which decay in flight to produce fake leptons must have $p_t > 6GeV/c$. We therefore take an average $\gamma_\pi \approx 50$ and $\gamma_K \approx 15$. With $c\tau_\pi = 7.8$ m and $c\tau_K = 3.7$ m, the decay distance ($\gamma c\tau$) for pions is about 400 meters and for kaons about 60 meters. If there were no material between the beam pipe and the muon chamber, then the probability of decay in flight would be $3.5/(\gamma c\tau)$. However, the pion or kaon could still decay once it has entered the CMU material prior to interacting. To take this effect into account we will consider an infinitesimal amount of material dx through which the pion or kaon enters. Given an initial number of particles N_0 and mean free path of the interacting material λ, the number of kaons or pions that survive from interaction and decay-in-flight after travelling a distance x is given by Equation 4-15.

$$N_x = N_0\, e^{-x(\frac{1}{\lambda}+\frac{1}{\gamma c\tau})} \tag{4-15}$$

If N_x particles enter the element dx, the number of particles that may decay-in-flight inside dx is given by Equation 4-16.

$$dN_d = N_x \frac{dx}{\gamma c\tau} \tag{4-16}$$

By integrating both sides of Equation 4-16, we will get Equation 4-17 which gives the number of particles that may decay-in-flight in the material after travelling

a distance x.

$$N_{decay} = \frac{N_0/\gamma c\tau}{(\frac{1}{\lambda} + \frac{1}{\gamma c\tau})} \left[1 - e^{-x(\frac{1}{\lambda} + \frac{1}{\gamma c\tau})}\right] \tag{4-17}$$

For iron, $\lambda \approx 0.2m$ and hence is much smaller than $\gamma c\tau$. Equation 4-17 then simplifies to Equation 4-18.

$$N_{decay} = \frac{N_0\lambda}{\gamma c\tau} \left[1 - e^{-\frac{x}{\lambda}}\right] \tag{4-18}$$

For CMP, x/λ is about 8. The probability of decay-in-flight in the material is :

$$\frac{N_{decay}}{N_0} = \frac{\lambda}{\gamma c\tau} \tag{4-19}$$

So the total probability of decay-in-flight is given by Equation 4-20.

$$\mathcal{P}_{DIF} = \frac{x}{\gamma c\tau} + \frac{\lambda}{\gamma c\tau} \approx \frac{x}{\gamma c\tau} \tag{4-20}$$

For pions, we have $\mathcal{P}^{\pi}_{DIF} = 3.5/400 \approx 1\%$ and for kaon we have $\mathcal{P}^{\pi}_{DIF} = 3.5/60 \approx 6\%$. These figures give an upper limit since the detector acceptance, track reconstruction efficiency and backward decay-in-flight of the pion or kaon have not yet been taken into account. A Monte Carlo study of the rate of decay-in-flight for pions and kaons done for a closely related analysis [23] gives $\mathcal{P}^{\pi}_{DIF} = 2.0 \pm 0.5\%$ and $\mathcal{P}^{K}_{DIF} = 0.7 \pm 0.2\%$. This study took into account the track reconstruction efficiency and detector acceptance. The number of fake muons N_{fake} resulting from this analysis are given by Equation 4-21.

$$N_{fake} = N^{CMU/P}_{CTC} \left[\mathcal{P}^{\pi}_{DIF} f_{\pi} + \mathcal{P}^{K}_{DIF} f_K\right] \tag{4-21}$$

We relaxed the muon identification cuts of the muon D^* sample, and consider all of the CTC tracks pointing to the CMU/CMP fiducial region ($N^{CMU/P}_{CTC}$). We obtained 304 events in the D^* signal region for $N^{CMU/P}_{CTC}$. We then determine the fraction of pions (f_{π}) and kaons (f_K) among these tracks. These fractions are determined using dE/dX (the energy lost of the particle in traversing a thickness dx of the material) measurement on the tracks. This procedure involved the gaussian fitting of the 3 pull distributions [2], namely the pull distribution of the

[2] A pull distribution is a distribution of the difference between a quantity and some expected quantity divided by the error

predicted $\frac{dE}{dx}$ for pions against the predicted $\frac{dE}{dx}$ for electrons (Equation 4-22), the pull distribution of the predicted $\frac{dE}{dx}$ for kaons against the predicted $\frac{dE}{dx}$ for electrons (Equation 4-23), and lastly the pull distribution of the measured $\frac{dE}{dx}$ against the predicted $\frac{dE}{dx}$ for electrons (Equation 4-24).

$$\frac{Pred\ \frac{dE^{\pi}}{dx} - Pred\ \frac{dE^{e}}{dx}}{Pred\ \sigma_{dE^{e}/dx}} \tag{4-22}$$

$$\frac{Pred\ \frac{dE^{K}}{dx} - Pred\ \frac{dE^{e}}{dx}}{Pred\ \sigma_{dE^{e}/dx}} \tag{4-23}$$

$$\frac{Measured\ \frac{dE}{dx} - Pred\ \frac{dE^{e}}{dx}}{Pred\ \sigma_{dE^{e}/dx}} \tag{4-24}$$

The gaussian fit of the quantity in Equation 4-22 gives width σ_π and mean μ_π while the gaussian fit of the quantity in Equation 4-23 gives width σ_K and mean μ_K. The quantity in Equation 4-24 is fitted with 3 gaussian. The first gaussian (the electron component) has a fixed width $\sigma_0 = 1$ and a fixed mean $\mu_0 = 0$, the second gaussian (the pion component) has a fixed width $\sigma'_\pi = \sqrt{1+\sigma_\pi^2}$ and a fixed mean μ_π, the third gaussian (the kaon component) has a fixed width $\sigma'_K = \sqrt{1+\sigma_K^2}$ and a fixed mean μ_K. These fits should be done as a function of track momentum. The result of this procedure in the signal region gives an electron fraction $f_e = 11.1 \pm 10.0\%$, a pion fraction $f_\pi = 88.9 \pm 17.6\%$ and a kaon fraction $f_K = 0 \pm 2.1\%$. Using these figures and the DIF rates $\mathcal{P}^{\pi}_{DIF} = 1\%$ and $\mathcal{P}^{K}_{DIF} = 6\%$ we have an upper limit of $N_{fake} = 2.7 \pm 0.6$ events expected among the 304 tracks pointing at CMU and CMP. This corresponds to a fake rate of about $0.9 \pm 0.2\%$. If we use $\mathcal{P}^{\pi}_{DIF} = 2.0 \pm 0.5\%$ and $\mathcal{P}^{K}_{DIF} = 0.7 \pm 0.2\%$ then we would get an upper limit of $N_{fake} = 5.4 \pm 1.7$ or a fake rate of $1.8 \pm 0.6\%$.

As a comparison we also adopted a MINUIT based likelihood fit method [24] on the same dE/dx distributions above. The result of the fit for the D^* signal region is tabulated in Table 4-4 and plotted in Fig. 4-41. This gives a maximum of $N_{fake} = 5.3 \pm 1.7$ or a fake rate of $1.8 \pm 0.6\%$ for the muon D^* data. A fit in the MDIF sideband region (See Fig. 4-42) gives $f_e = 6.2 \pm 4.5\%$, $f_\pi = 87.5 \pm 8.2\%$, $f_K = 5.6 \pm 5.7\%$ and $f_p = 0.8 \pm 0.2\%$.

	Signal Region	Sideband
f_e	$10.8 \pm 9.6\%$	$6.2 \pm 4.5\%$
f_π	$87.4 \pm 17.2\%$	$87.5 \pm 8.2\%$
f_K	$1.9 \pm 8.3\%$	$5.6 \pm 5.7\%$
f_p	$0 \pm 0.4\%$	$0.8 \pm 0.2\%$

Table 4-4. The result of the likelihood fit on the dE/dx pull distributions for the CMU/CMP fiducial tracks in the MDIF signal region and sideband region.

As for the remaining fakes in the electron sample, they consist basically either a π_0 in the proximity of a charged pion track where the neutral pion showers in the calorimeter, or a charged pion or kaon track that showers early in the calorimeter. The dE/dx measurement and prediction for the electron tracks are used together with the dE/dx predictions for pion, kaon, proton and the prediction of the dE/dx width. The result of the dE/dx likelihood fit for the electron candidate tracks in the D^* signal region is tabulated in Table 4-5 and plotted in Fig. 4-43. There are 380 events in the signal region, but only 102 events pass the $N_{ctc} > 24$ cut (the number of CTC hits used to calculate dE/dx after 80% mean truncation) of the likelihood fitter. The number of pionic fake electrons among the 380 events in the signal region predicted by the fit is 64 ± 53 events. These are the fakes associated with both real D^* and fake D^* in the signal region. We know from the MDIF fit that the fraction of fake D^*'s in the signal region is about $56.1 \pm 3.6\%$. Now we need to find out the amount of fake electron associated with real D^*. To do this we look into the MDIF sideband region where all the events are fake D^*'s.

We present the results of the dE/dx likelihood fit for the sideband region, with 1429 events, in Table 4-5 as well. The sideband fit shows $32.1 \pm 7.8\%$ of the tracks are fake electrons. We know that all the tracks in the sideband region

	Signal Region	Sideband
f_e	$83.1 \pm 16.1\%$	$67.9 \pm 5.1\%$
f_π	$16.9 \pm 14.0\%$	$25.6 \pm 6.8\%$
f_K	0	$5.8 \pm 3.7\%$
f_p	0	$0.7 \pm 1.3\%$

Table 4-5. The result of the likelihood fit on the dE/dx pull distributions for the electron tracks in the MDIF signal region and sideband region.

are associated with fake D^*'s. If we extrapolate this result into the signal region we expect to have $(32.1 \pm 7.8\%) \times (56.1 \pm 3.6\%) \times 380 = 68 \pm 17$ fake electrons associated with fake D^*'s in the signal region. So the number of fake electrons in the signal region associated with real D^*'s should be $(64 \pm 53) - (68 \pm 17) = -4 \pm 56$ events. This result, although with a large error bar, is consistent with the result from the PTREL fit, namely we do not have any fake electrons associated with real D^*'s.

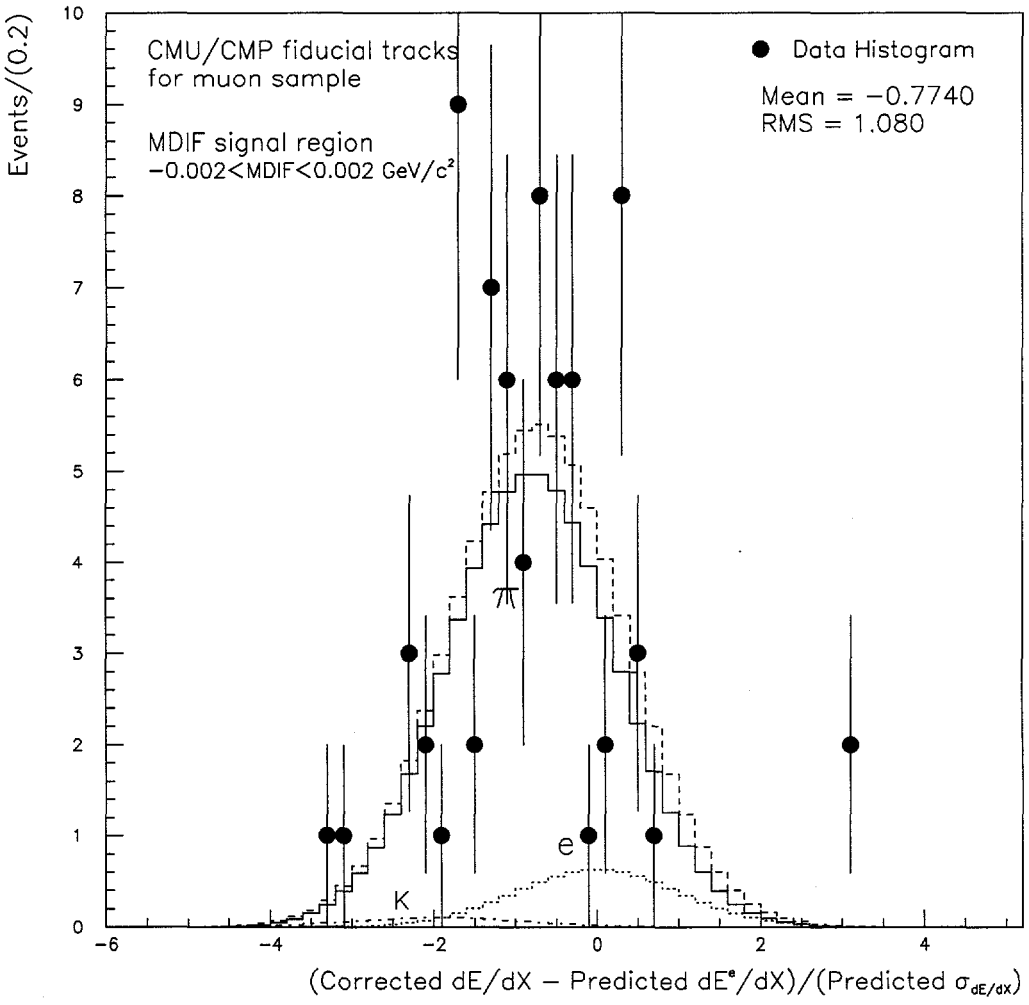

Figure 4-41. The likelihood fit result on the measured dE/dx pull distribution of the CMU/CMP fiducial tracks in the D^* signal region superimposed with the predicted distribution for the pion, kaon and electron components.

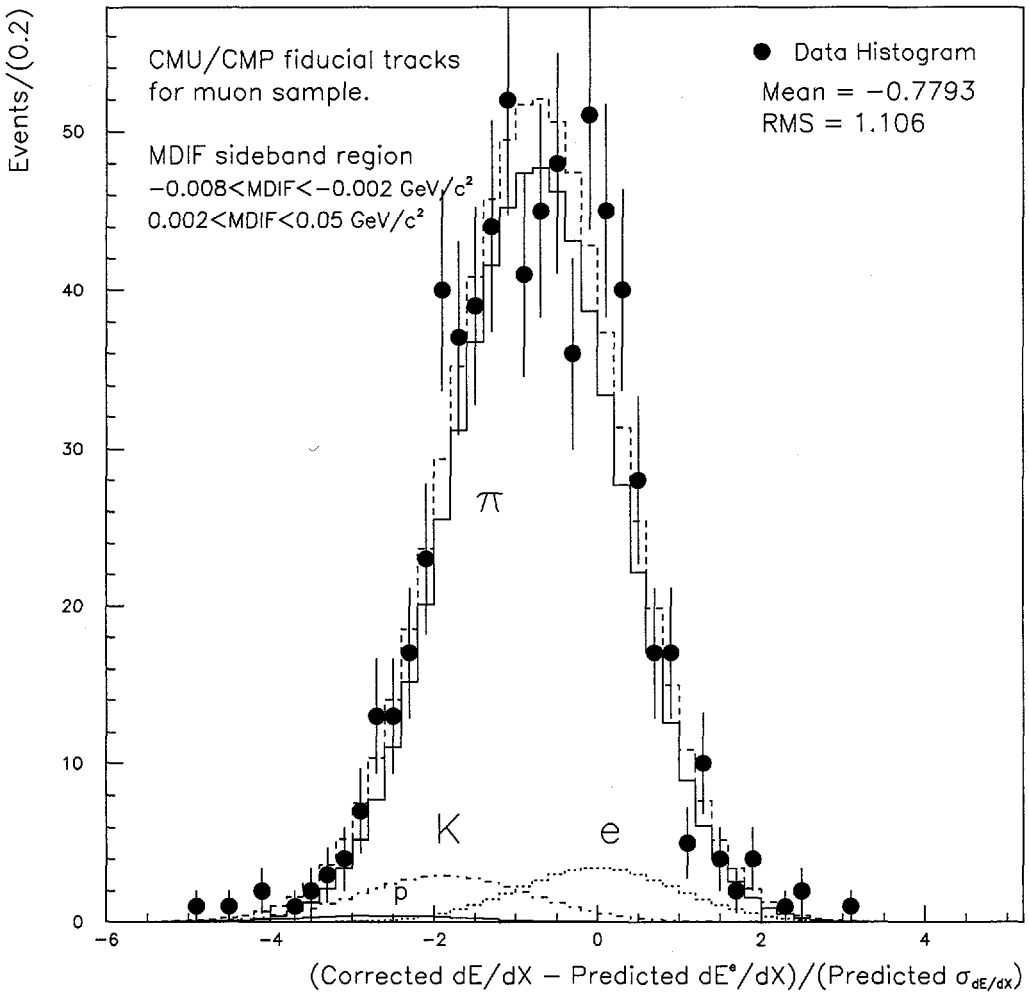

Figure 4-42. The likelihood fit result on the measured dE/dx pull distribution of the CMU/CMP fiducial tracks in the D^* sideband region superimposed with the predicted distribution for the pion, kaon and electron components.

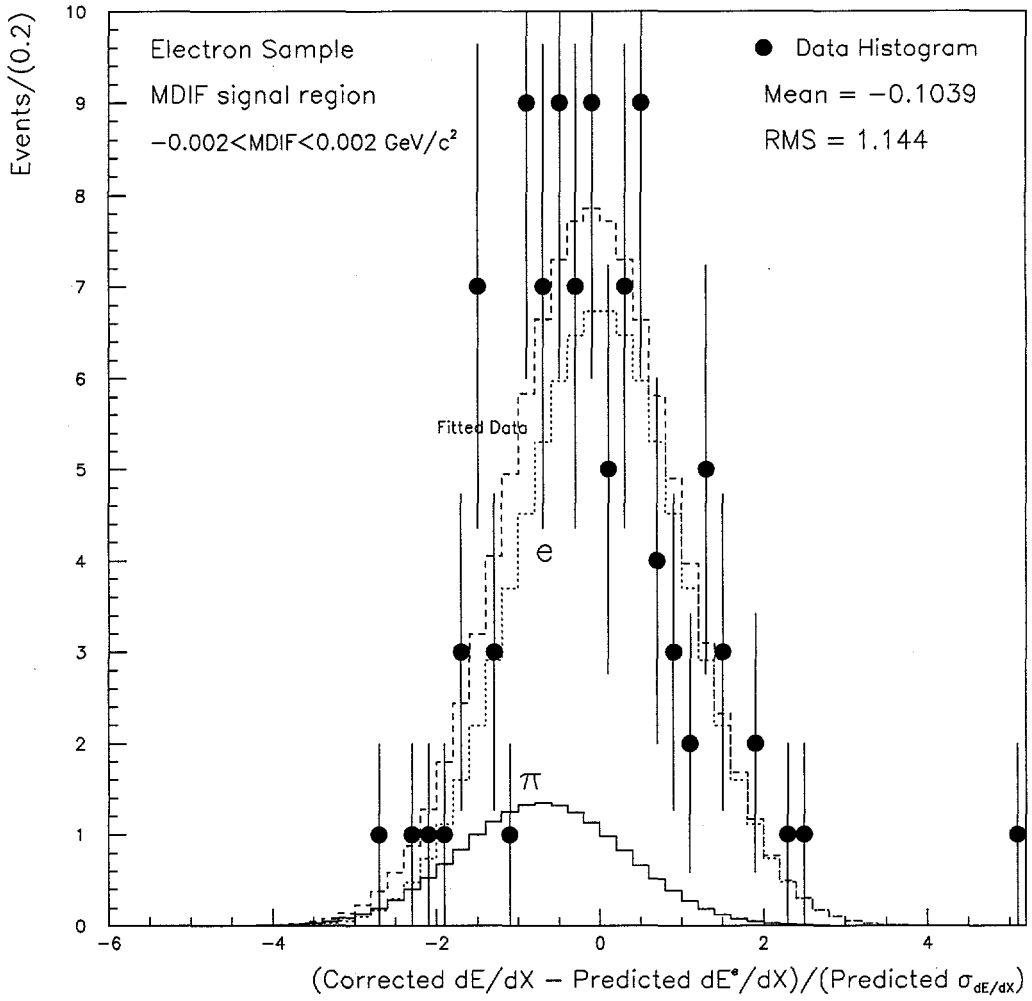

Figure 4-43. The likelihood fit result on the measured dE/dx pull distribution of the electron tracks in the D^* signal region superimposed with the predicted distribution for the pion, kaon and electron components.

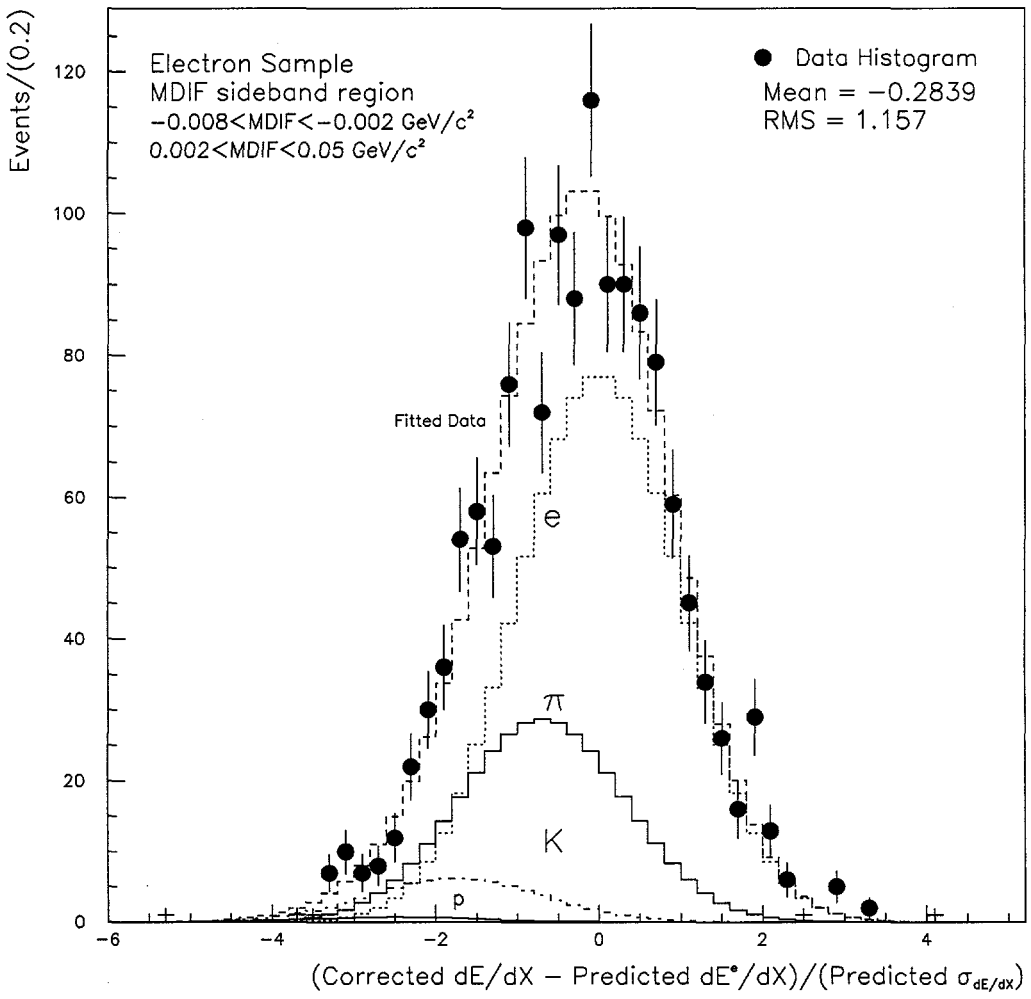

Figure 4-44. The likelihood fit result on the measured dE/dx pull distribution of the electron tracks in the D^* sideband region superimposed with the predicted distribution for the pion, kaon and electron components.

F. Comparison Between Data and Monte Carlo

To be confident of our sample composition estimation and of the quality of our data distribution, we compare the distribution of the data with the distribution generated by Monte Carlo. The Monte Carlo sample was generated using Pythia and the mixing parameter was set to be 0.7 for X_d and 10 for X_s in the decay table. Only the decays of D^0, $\bar{D}^0$, $D^{*\pm}$ were forced into the channels of interest. Figures 4-45 and 4-46 show the comparison between the background subtracted signal CTAU distribution and Monte Carlo for the like sign and unlike sign D^* electron samples respectively. Figure 4-47 and 4-48 represent these comparisons for D^* muon samples. We can see from these comparisons that our signal data distributions are consistent with Monte Carlo.

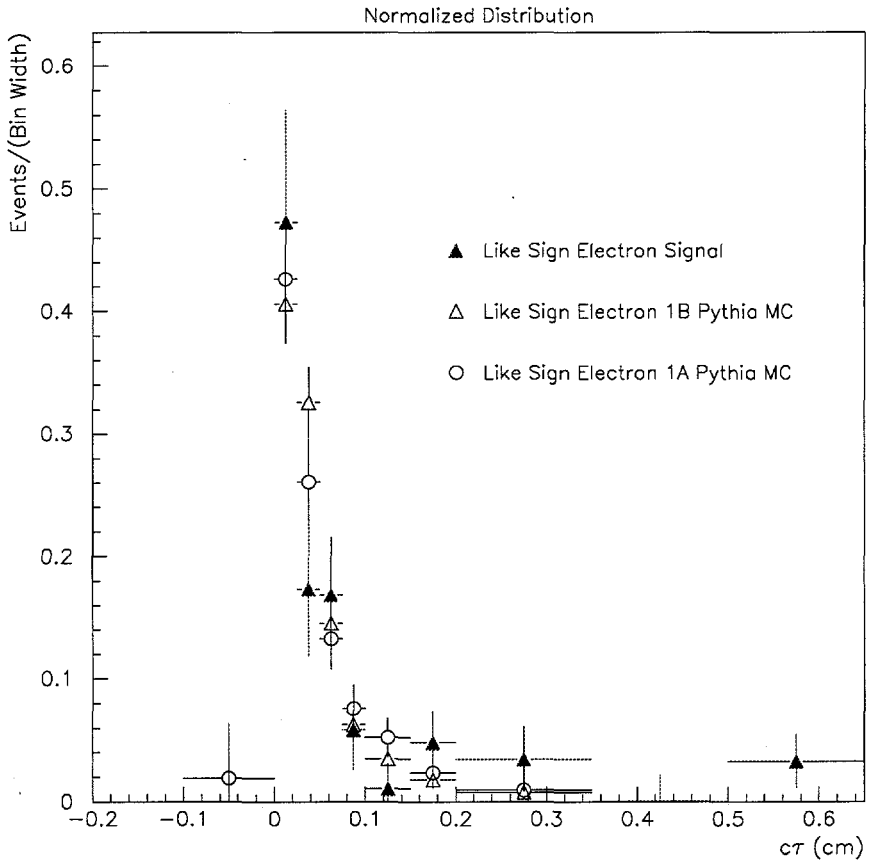

Figure 4-45. Background subtracted signal CTAU distribution for like sign Run 1A+1B $e\,D^{\star}$ sample compared with that of like sign Run 1A and Run 1B Pythia Monte Carlo.

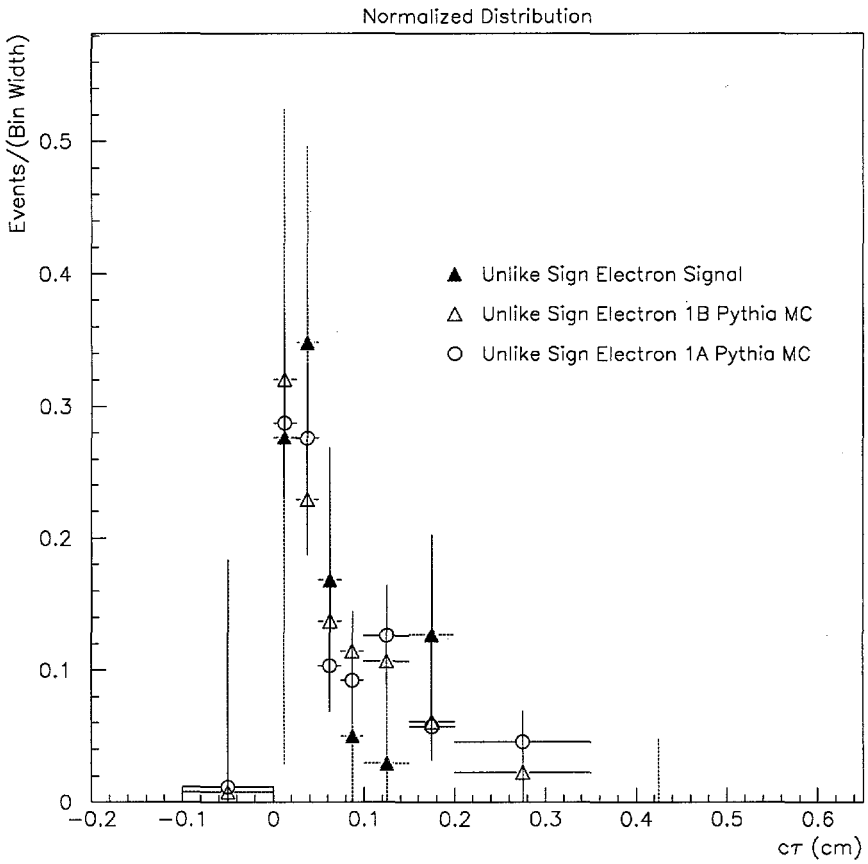

Figure 4-46. Background subtracted signal CTAU distribution for unlike sign Run 1A+1B e $D^{\star}$ sample compared with that of unlike sign Run 1A and Run 1B Pythia Monte Carlo.

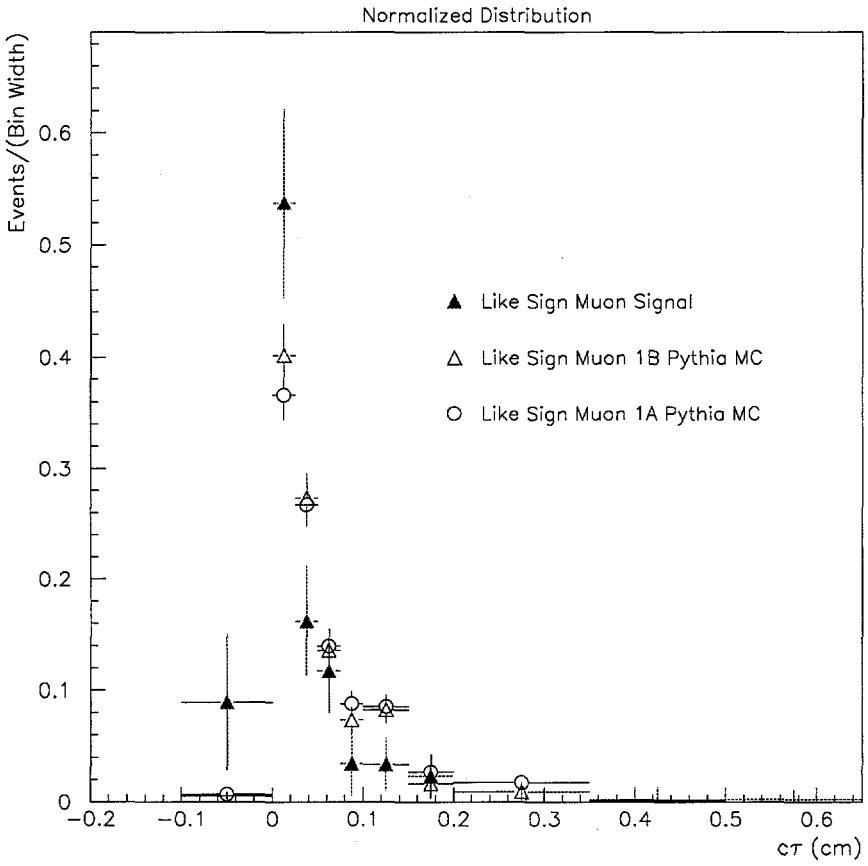

Figure 4-47. Background subtracted signal CTAU distribution for like sign Run 1A+1B μ $D^{\star}$ sample compared with that of like sign Run 1A and Run 1B Pythia Monte Carlo.

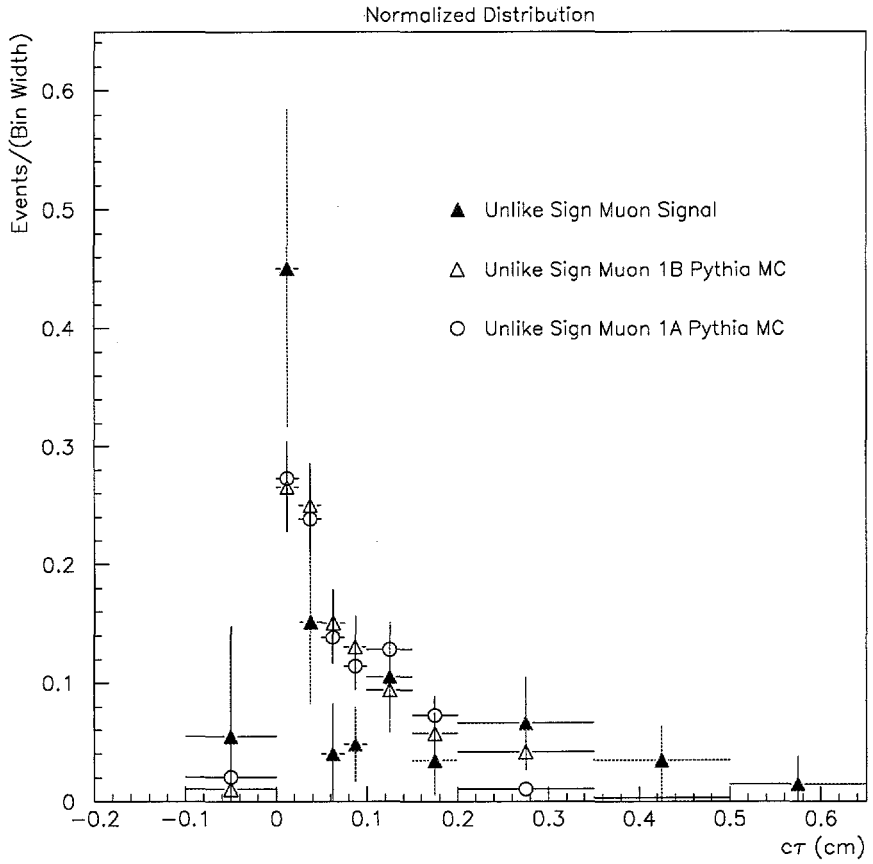

Figure 4-48. Background subtracted signal CTAU distribution for unlike sign Run 1A+1B μ $D^{\star}$ sample compared with that of unlike sign Run 1A and Run 1B Pythia Monte Carlo.

G. Asymmetry Distribution Fitting Function

The measurement of ΔM_d is done by fitting the asymmetry distribution (oscillation plot) with a fitting function. There are two ways of presenting the asymmetry distribution :

1. Using $c\bar{c}$ and combinatoric background subtracted $c\tau_B$ distributions.

2. Using $c\tau_B$ distributions where all the backgrounds including the combinatorics and $c\bar{c}$ are not subtracted. The fake lepton background is taken to be zero.

The asymmetry distribution without backgrounds is a useful visual aid in understanding any problem that may contribute to the accuracy of the measurement since we can clearly see the expected cosine distribution. However, keeping the backgrounds in the distribution and accounting for them in the fitting function makes it much more convenient for the systematic error study since one simply has to set a parameter in the fitting function to its upper or lower limit instead of repeating the procedure of subtracting the backgrounds out of the distribution. For convenience in the systematic error determination, we shall keep the backgrounds in the $c\tau_B$ distributions.

1. Details of Fitting Function

The fitting function contains the asymmetry formula as a function of time. This formula is just the basic asymmetry convoluted with a gaussian $c\tau$ resolution due to vertex smearing. The asymmetry as a function of time is described in the following equation.

$$\begin{aligned} A(t) &= \frac{N^l(t) - N^u(t)}{N^l(t) + N^u(t)} \\ &= \frac{Prob(B^0 \to B^0) - Prob(B^0 \to \bar{B}^0)}{Prob(B^0 \to B^0) + Prob(B^0 \to \bar{B}^0)} \\ &= \cos\left(\frac{x\,t}{\tau}\right) \end{aligned} \tag{4-25}$$

Including contributions from $c\bar{c}$, $B^{\pm}$ and B_s^0, $A(t)$ becomes :

$$A(t) = \frac{\Sigma^{d,s} f_{d,s}[F_{d,s}^{NM}(t) - F_{d,s}^{M}(t)] + \frac{f_{ch}e^{-t/\tau_B}}{\tau_B} - \frac{f_{c\bar{c}}e^{-t/\tau_{c\bar{c}}}}{\tau_{c\bar{c}}}}{\Sigma^{d,s}\frac{f_{d,s}e^{-t/\tau_B}}{\tau_B} + \frac{f_{ch}e^{-t/\tau_B}}{\tau_B} + \frac{f_{c\bar{c}}e^{-t/\tau_{c\bar{c}}}}{\tau_{c\bar{c}}} + f_{com}\frac{e^{-t/\tau_{com}}}{\tau_{com}}} \quad (4\text{-}26)$$

Here we consider $\tau_{B^0} \approx \tau_{B^{\pm}}$. $F_{d,s}^{NM}(t)$ and $F_{d,s}^{M}(t)$ are the non-mixing and mixing probability functions.

$$F_i^{NM}(t) = \frac{e^{-t/\tau_B}}{2\tau_B}(1 + \cos(\frac{x_i t}{\tau_B})) \quad (4\text{-}27)$$

$$F_i^{M}(t) = \frac{e^{-t/\tau_B}}{2\tau_B}(1 - \cos(\frac{x_i t}{\tau_B})) \quad (4\text{-}28)$$

The index i represents either a d or s quark. $f_{d,s}$, f_{ch}, $f_{c\bar{c}}$ and f_{com} are fractions of $B_{d,s}^0$, $B^{\pm}$, $c\bar{c}$ and combinatorics respectively in the signal. The sum of these fractions should add up to 1. We can collect the B related fractions into one term called f_B for convenience.

$$f_d + f_s + f_{ch} + f_{c\bar{c}} + f_{com} = 1 \quad (4\text{-}29)$$

$$f_d + f_s + f_{ch} = (C_d + C_s + C_{ch})f_B = f_B \quad (4\text{-}30)$$

$$f_B = 1 - f_{c\bar{c}} - f_{com} \quad (4\text{-}31)$$

Each term in $A(t)$ is convoluted with a gaussian function describing the $c\tau$ resolution smearing. The resolution function σ(t) is determined using MC. After smearing the equation, $A(t)$ becomes :

$$A(t) = \frac{\Sigma^{d,s} f_{d,s}[\mathcal{F}_{d,s}^{NM} - \mathcal{F}_{d,s}^{M}] + f_{ch}E_{ch} - f_{c\bar{c}}E_{c\bar{c}}}{\Sigma^{d,s} f_{d,s}E_{d,s} + f_{ch}E_{ch} + f_{c\bar{c}}E_{c\bar{c}} + f_{com}E_{com}} \quad (4\text{-}32)$$

where the smeared non-mixing and mixing probability function (i=d,s) is :

$$\mathcal{F}_i^{NM,M}(t,\sigma) = F_i^{NM,M}(t) \otimes G(t,\sigma) \quad (4\text{-}33)$$
$$= \frac{1}{\sqrt{2\pi}\sigma\tau_B}\int_0^{\infty} e^{-\frac{z}{\tau_B}} e^{-\frac{(t-z)^2}{2\sigma^2}}(1 \pm \cos(\frac{x_i z}{\tau_B}))dz$$

and the smeared B meson and $c\bar{c}$ contribution are :

$$E_{d,s} = \frac{1}{\sqrt{2\pi}\sigma\tau_B}\int_0^\infty e^{-z/\tau_B}e^{-(t-z)^2/2\sigma^2}dz \quad (4\text{-}34)$$

$$E_{ch} = \frac{1}{\sqrt{2\pi}\sigma\tau_B}\int_0^\infty e^{-z/\tau_B}e^{-(t-z)^2/2\sigma^2}dz \quad (4\text{-}35)$$

$$E_{c\bar{c}} = \frac{1}{\sqrt{2\pi}\sigma\tau_{c\bar{c}}}\int_0^\infty e^{-z/\tau_{c\bar{c}}}e^{-(t-z)^2/2\sigma^2}dz \quad (4\text{-}36)$$

$$E_{com} = N_k\int_0^\infty (\frac{C}{ct1}e^{-z/ct1} + \frac{1-C}{ct2}e^{-z/ct2})dz \quad (4\text{-}37)$$

We can see that $E_{d,s} = E_{ch} \equiv E_B$. This is because we consider $\tau_{B^0} \approx \tau_{B^\pm}$. A simple algebra and saturating the value of X_s to a large value leads to :

$$A(t) = \frac{\mathcal{D}_0(f_d\mathcal{A}_d(t,\sigma) + f_{ch})E_B - f_{c\bar{c}}E_{c\bar{c}}}{f_BE_B + f_{c\bar{c}}E_{c\bar{c}} + f_{com}E_{com}}$$

$$f_d = (1 - C_s - C_{ch})(1 - f_{c\bar{c}} - f_{com})$$

$$f_{ch} = C_{ch}(1 - f_{c\bar{c}} - f_{com})$$

where the asymmetry part for the B_d^0 is :

$$\mathcal{A}_d(t,\sigma) = [\mathcal{F}_d^{NM} - \mathcal{F}_d^M]/E_B \quad (4\text{-}38)$$

$\mathcal{A}_d(t,\sigma)$ is the real part of the ratio of two complex WWERF functions analytically derived by assuming that the $c\tau$ resolution is gaussian distributed and varies slowly as a function of $c\tau$.

$$WWERF(z) = e^{-z^2}\left(1 + \frac{2i}{\sqrt{\pi}}\int_0^z e^{t^2}\,dt\right) \quad (4\text{-}39)$$

$\mathcal{D}_0$ is the dilution parameter, the value of which is generally different from 1 because of the lepton sign mistag rate.

The combinatoric background lifetime (E_{com}) part of the fitting function is obtained by parametrizing the normalized $c\tau_B$ shape of electron and muon samples (Fig. 4-49) in the MDIF sideband region ($-0.008 < MDIF < -0.002$ and $0.002 < MDIF < 0.008$). This shape is parametrized with the sum of two exponentials. To get E_B, or the $b\bar{b}$ lifetime portion of the fitting function, we parametrize the reconstructed $c\tau_B$ distribution of $b\bar{b}$ events from a Pythia Monte Carlo sample. The shape is parametrized with a gaussian convoluted

exponential and a frequency function to describe the turn-on effect (Fig. 4-50). Similarly for $E_{c\bar{c}}$, the $c\bar{c}$ part, we use $c\bar{c}$ Pythia Monte Carlo sample. The $c\tau$ shape here is also parametrized with a gaussian convoluted exponential and a frequency function (Fig. 4-51).

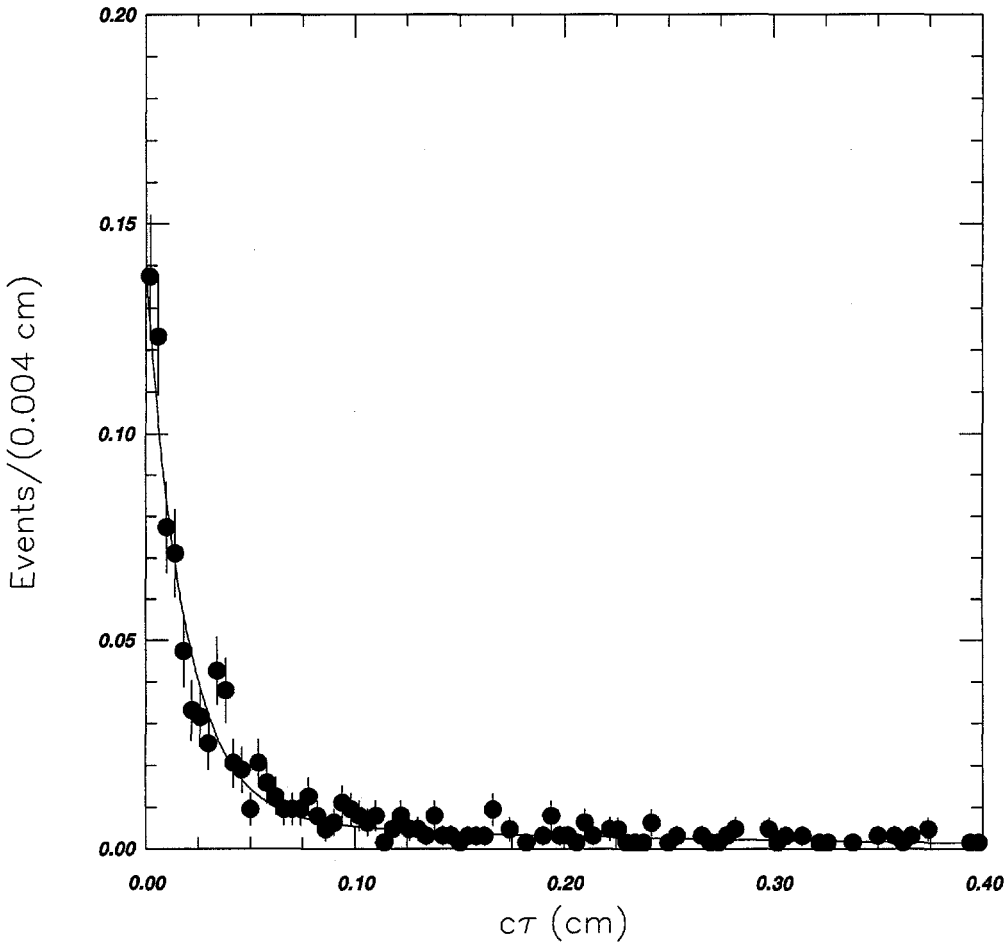

Figure 4-49. Normalized combinatorics estimated $c\tau_B$ shape from e and μ sample (LS+US) MDIF sideband parametrized with the sum of two exponentials.

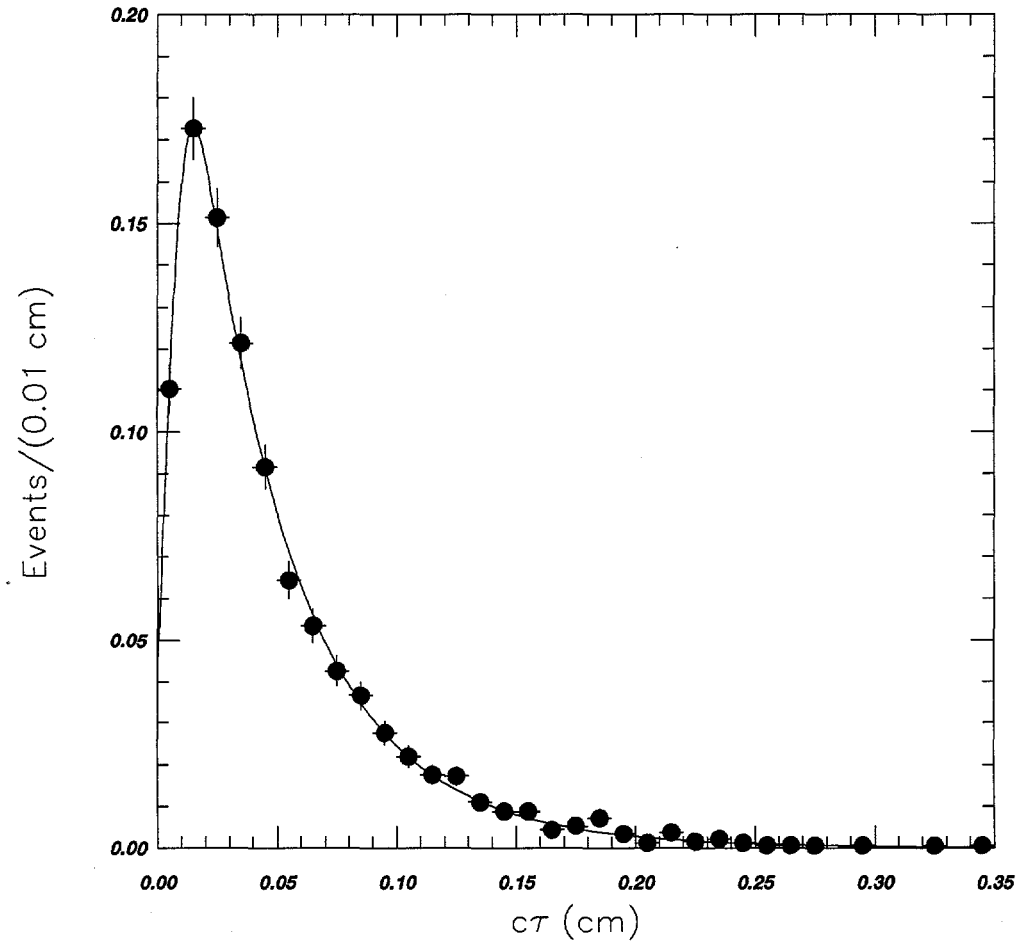

Figure 4-50. Normalized estimated $c\tau_B$ distribution shape from $b\bar{b}$ Pythia Monte Carlo Run 1A and Run 1B e and μ sample (LS+US). The shape is parametrized with a gaussian convoluted exponential function and a FREQ function to describe the turn-on effect in the low $c\tau_B$ region.

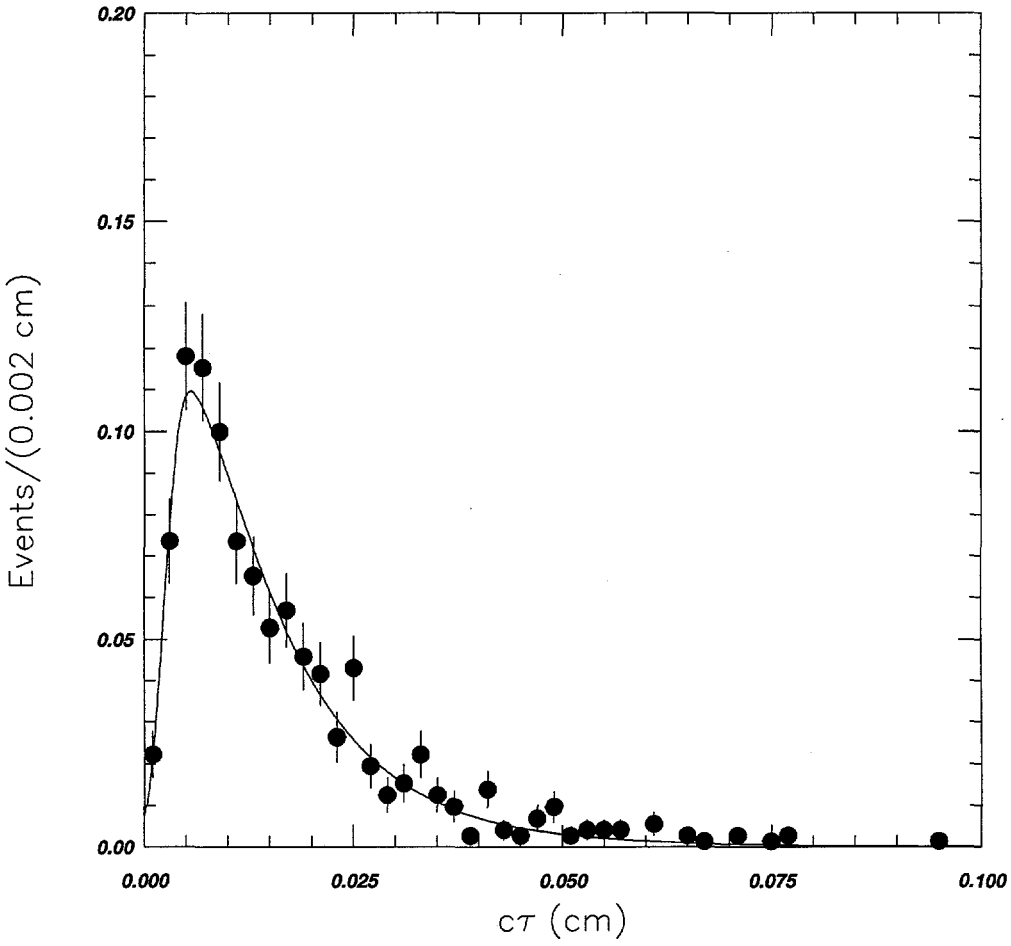

Figure 4-51. Normalized estimated $c\tau$ distribution shape from $c\bar{c}$ Pythia Monte Carlo Run 1A and Run 1B e and μ sample (LS+US). The shape is parametrized with a gaussian convoluted exponential function and a FREQ function to describe the turn-on effect in the low $c\tau$ region.

a. $c\tau$ Resolution Function.

A B_d^0 Monte Carlo sample (47168 events) with $X_d = 0.7$ generated using BGEN program is used in the study of the estimated $c\tau_B$ resolution function. Since the detector resolution is small compared to the B vertex reconstruction resolution, we use the generated information on P_{t_D} and L_{xy} in constructing the $c\tau_B$ quantity for this study. Figure 4-52 shows that the estimated $c\tau_B$ resolution in the region of $0 < c\tau_B < 0.65$ cm is more accurately described by 2 gaussians rather than by a single gaussian function. But each $c\tau_B$ bin in Fig. 4-53 is well described by a single gaussian fit. Figure 4-53 shows the σ of the gaussian fit ($c\tau$ resolution) as a straight line ($P_1 + P_2 x$ cm) function of $c\tau_B$. The fit gives $P_1 = 51$ μm and $P_2 = 0.2027$. This straight line form of the $c\tau$ resolution ($\sigma_{c\tau}$) works reasonably well when used in the WWERF fitting function $\mathcal{A}_d(t, \sigma)$. A higher order polynomial with an exponential term ($P_1 + P_2 x + P_3 x^2 + P_4 e^{-P_5 x}$) fits better to the $c\tau$ resolution distribution. When used in the WWERF fitting function $\mathcal{A}_d(t, \sigma)$, this higher order $\sigma_{c\tau}$ performs better than the simple straight line $\sigma_{c\tau}$ in extracting a known MC ΔM_d.

The asymmetry distribution of the same B_d^0 MC sample used for the $c\tau$ resolution study is shown in Fig. 4-55 and Fig. 4-56. The input value of X_d to generate the sample is 0.7, which corresponds to a value of ΔM_d of 0.45. Since the sample consists purely of B_d^0, the dilution of the asymmetry distribution is expected to be 1. The sample is used to test the $\mathcal{A}_d(t, \sigma)$ part of the fitting function, to see how well the straight line or higher order polynomial parametrization of the $c\tau$ resolution function perform in the WWERF form of $\mathcal{A}_d(t, \sigma)$. The result of the fitting function with the straight line form of $\sigma_{c\tau}$ is shown in Fig. 4-55. As a comparison we can see Fig. 4-56 which shows the result of the fitting function with ($\sigma_{c\tau} = P_1 + P_2 x + P_3 x^2 + P_4 e^{-P_5 x}$). Here we can see that the fitting function with the higher order form of σ extracts the value of ΔM_d better than the same fitting function with the straight line form of σ.

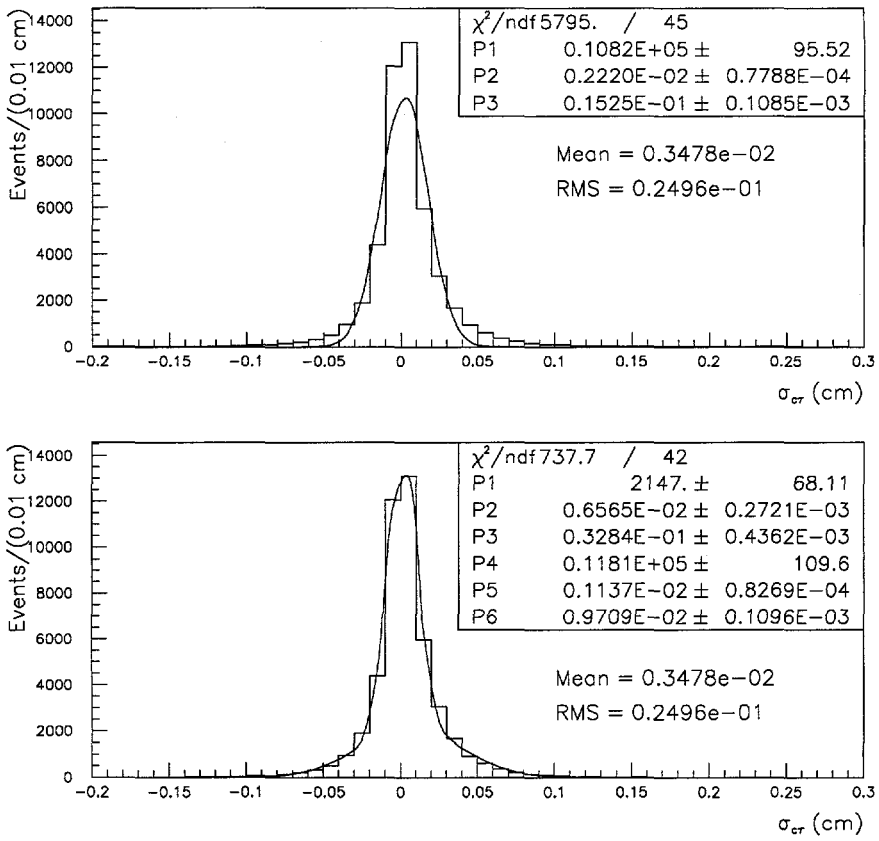

Figure 4-52. Estimated $c\tau_B$ resolution fitted using a gaussian function (top) and using 2 gaussians (bottom). P1(P4),P2(P5),P3(P6) are the area, the mean and the width of the gaussian fit.

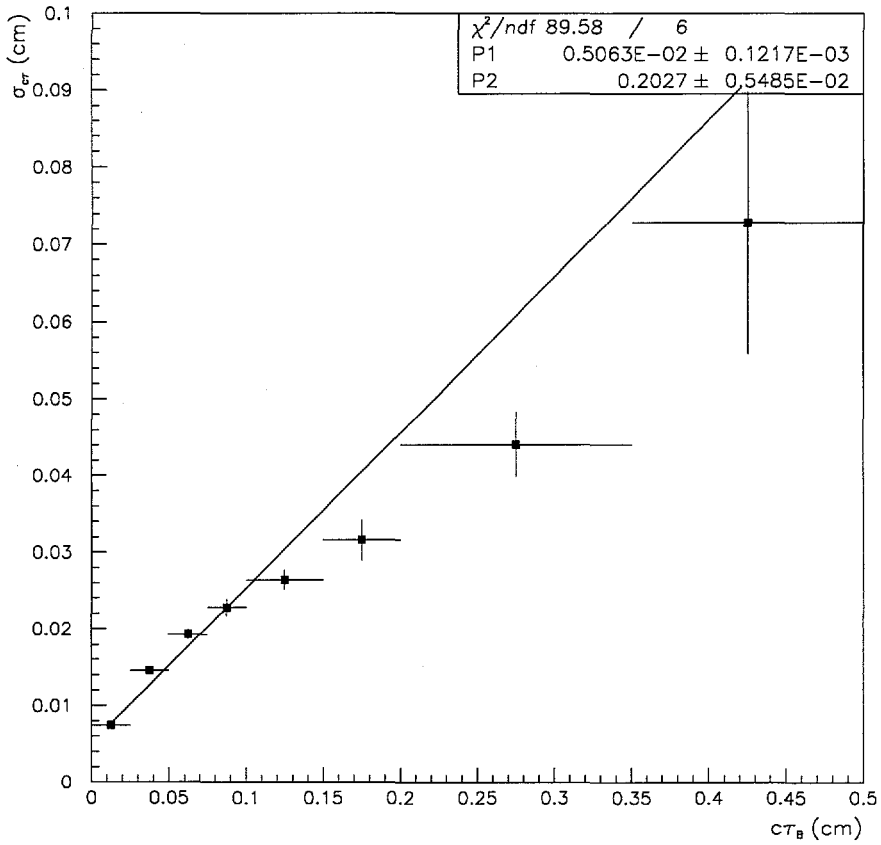

Figure 4-53. Estimated $c\tau_B$ resolution (gaussian sigma) as a function of $c\tau_B$ fitted with a straight line ($\sigma_{c\tau} = P_1 + P_2 x$). Each $c\tau_B$ bin is fitted using a gaussian function.

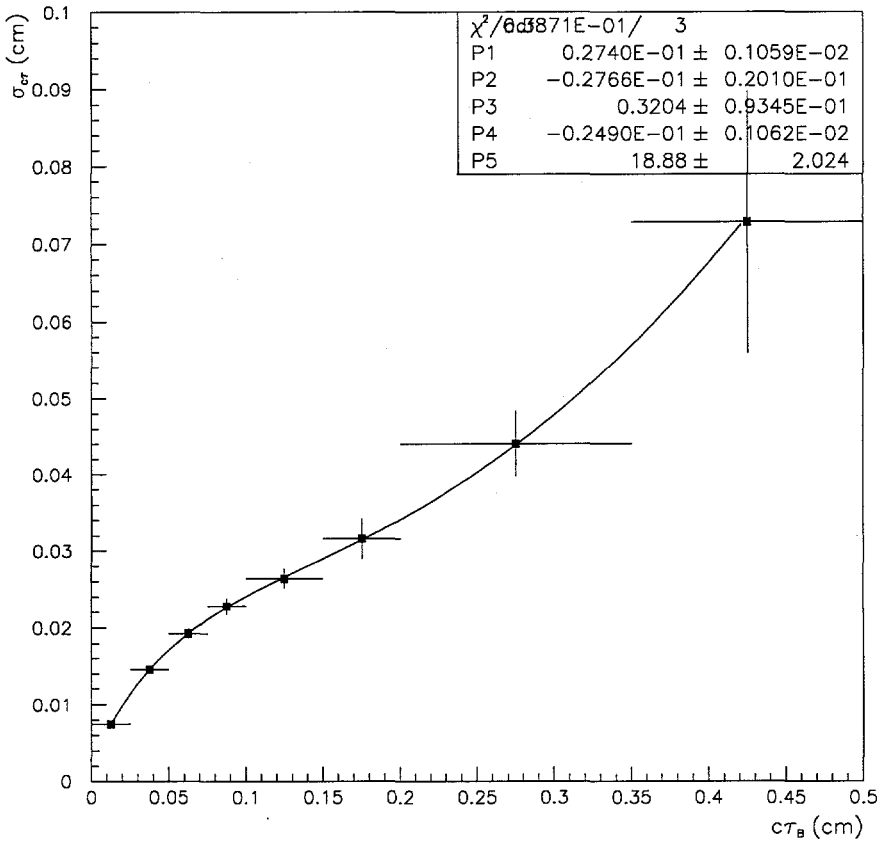

Figure 4-54. $\sigma_{c\tau} = P_1 + P_2 x + P_3 x^2 + P_4 e^{-P_5 x}$.

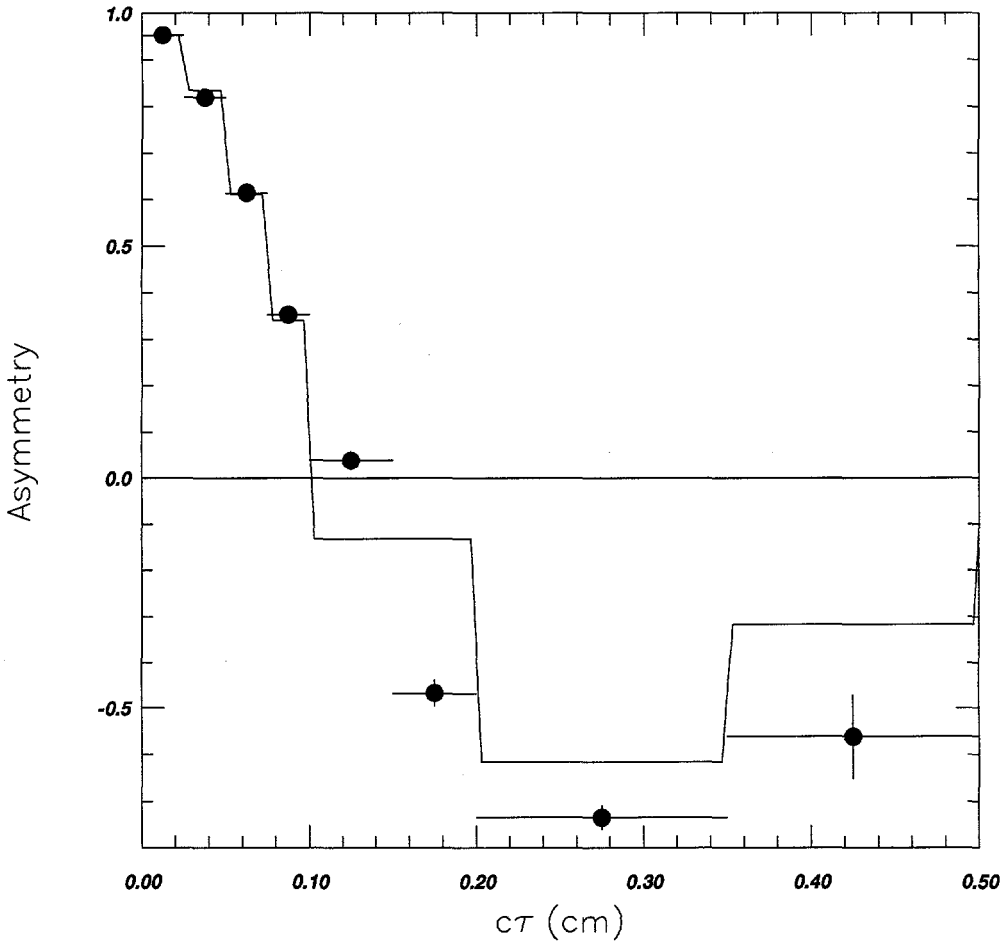

Figure 4-55. The result of the asymmetry fit using $\sigma_{c\tau} = 0.005063 + 0.2027x$ on an asymmetry distribution of a Monte Carlo sample generated with $\Delta M_d = 0.45$ and $\mathcal{D}_0 = 1$. The fit results are $\Delta M_d = 0.475$ and $\mathcal{D}_0 = 0.985$.

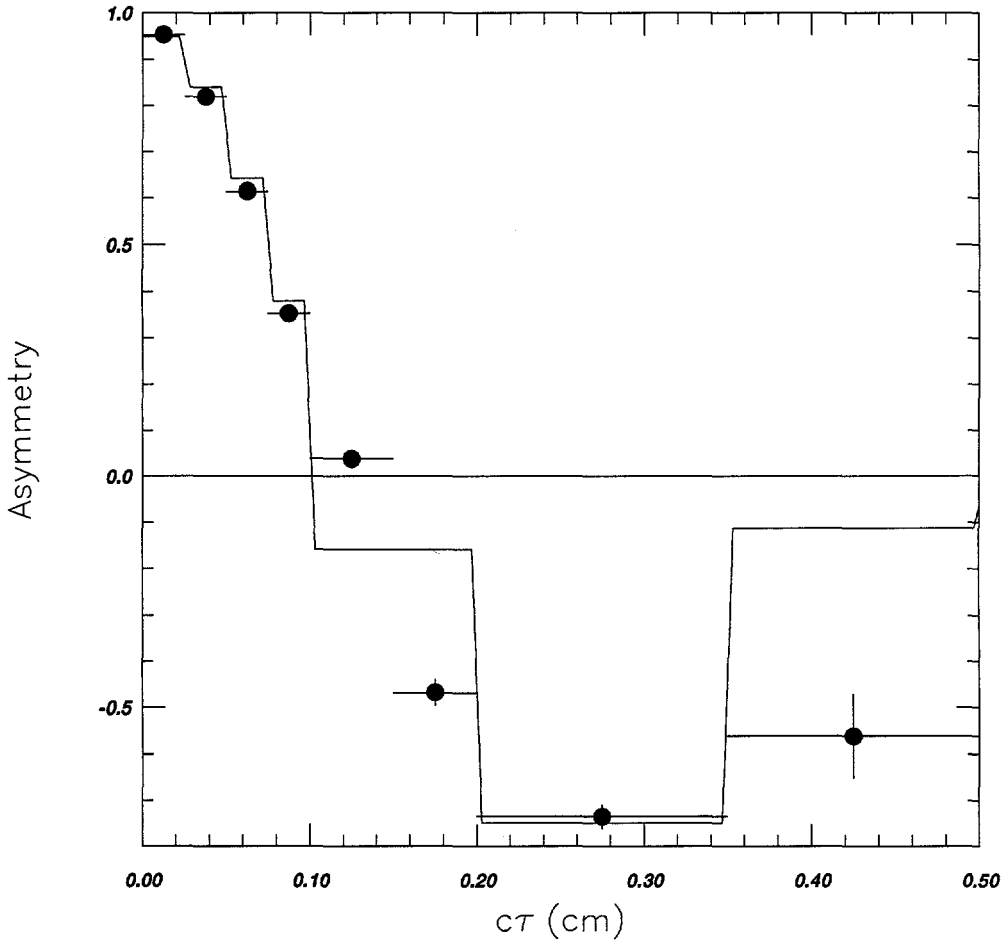

Figure 4-56. The result of the asymmetry fit using $\sigma_{c\tau} = P_1 + P_2 x + P_3 x^2 + P_4 e^{-P_5 x}$ on the same asymmetry distribution as in Fig. 4-55. The fit results are $\Delta M_d = 0.455$ and $\mathcal{D}_0 = 0.978$.

b. TOYMC Sample and Binning Effect.

To test the whole part of the fitting function we need to have asymmetry plots of Monte Carlo events with known background compositions and ΔM_d. For this purpose a TOYMC program was prepared. This program generates $c\tau$ distributions of $b\bar{c}$, $c\bar{c}$ and combinatoric events according to the parametrization we have for E_B, $E_{c\bar{c}}$, and E_{com}. The relative amount of each component and the mistag rate (dilution) can be varied and fixed conveniently. The TOYMC sample is used for the calibration of the fitter. It is especially useful for the study and correction of the binning effect on the fitter's accuracy in measuring the value of ΔM_d.

First, a TOYMC sample consisting of 1 million B_d^0 events is made with $\Delta M_d^{input} = 0.474\, ps^{-1}$ and $D_0^{input} = 0.67$. The fitting function is used to extract these parameter values from the asymmetry distribution. When the distribution is binned very finely (520 bins) or practically unbinned (Fig. 4-57), the fitting function gives $\Delta M_d^{output} = 0.475 \pm 0.001$ and $D_0^{output} = 0.669 \pm 0.001$. However, if the distribution is binned (Fig. 4-58) according to the binning used in the real data, the fitting function gives $\Delta M_d^{output} = 0.439 \pm 0.001$ and $D_0^{output} = 0.654 \pm 0.001$. So the binning effect is an offset in ΔM_d of 0.035 ± 0.001. The discrepancy due to the binning can be corrected by modifying the fitting function. This is done by taking the fitting function value for the asymmetry averaged over the bin instead of taking the value at the center of the bin. The averaging is done bin by bin resulting in a discrete distribution instead of a continuous distribution of the asymmetry. If we use this discrete version of the fitting function on the binned $c\tau$ distribution (Fig. 4-59), we can obtain the input value with an accuracy within 0.4% ($\Delta M_d^{output} = 0.476$ and $D_0^{output} = 0.670$). This very small shift is most likely due to the accuracy of the numerical integration procedure in the MNFIT fitting program.

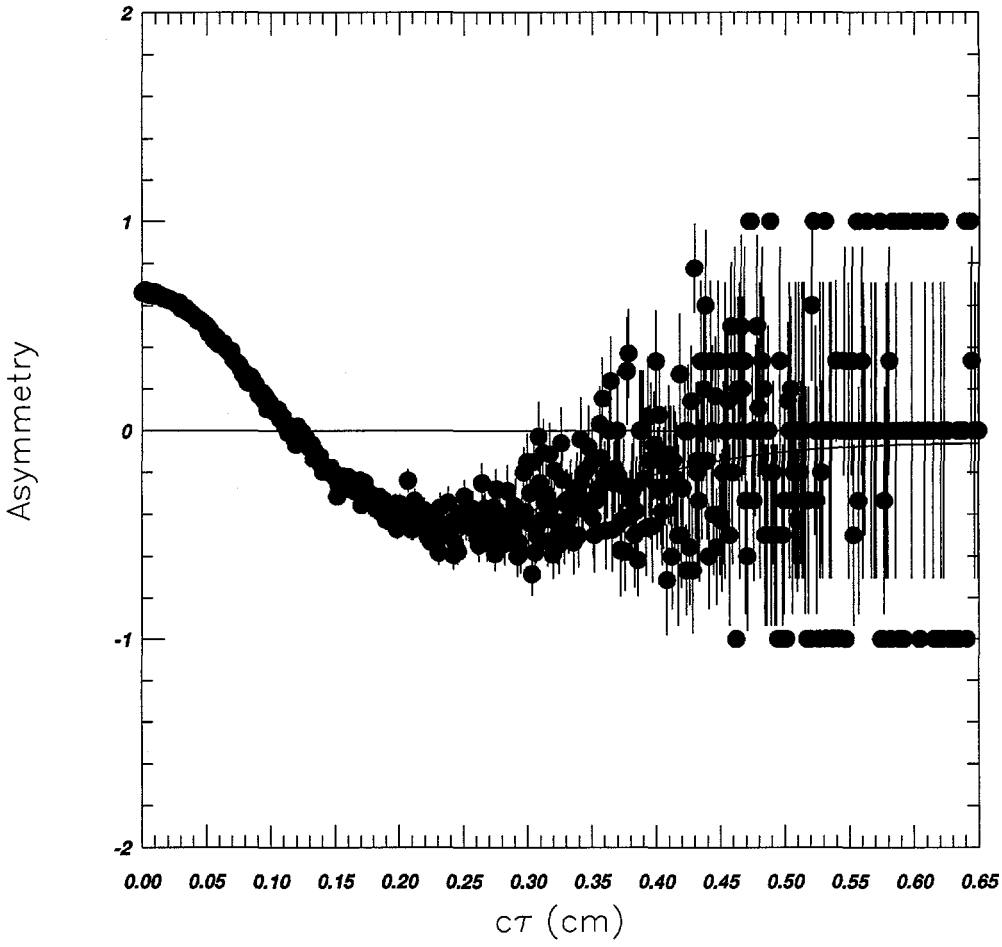

Figure 4-57. The fit result on the unbinned asymmetry distribution of 1 million pure B_d^0 events. Input ΔM_d is 0.474 and input dilution is 0.67. Fit ΔM_d is 0.475 ± 0.001 and $\mathcal{D}_0$ is 0.669 ± 0.001.

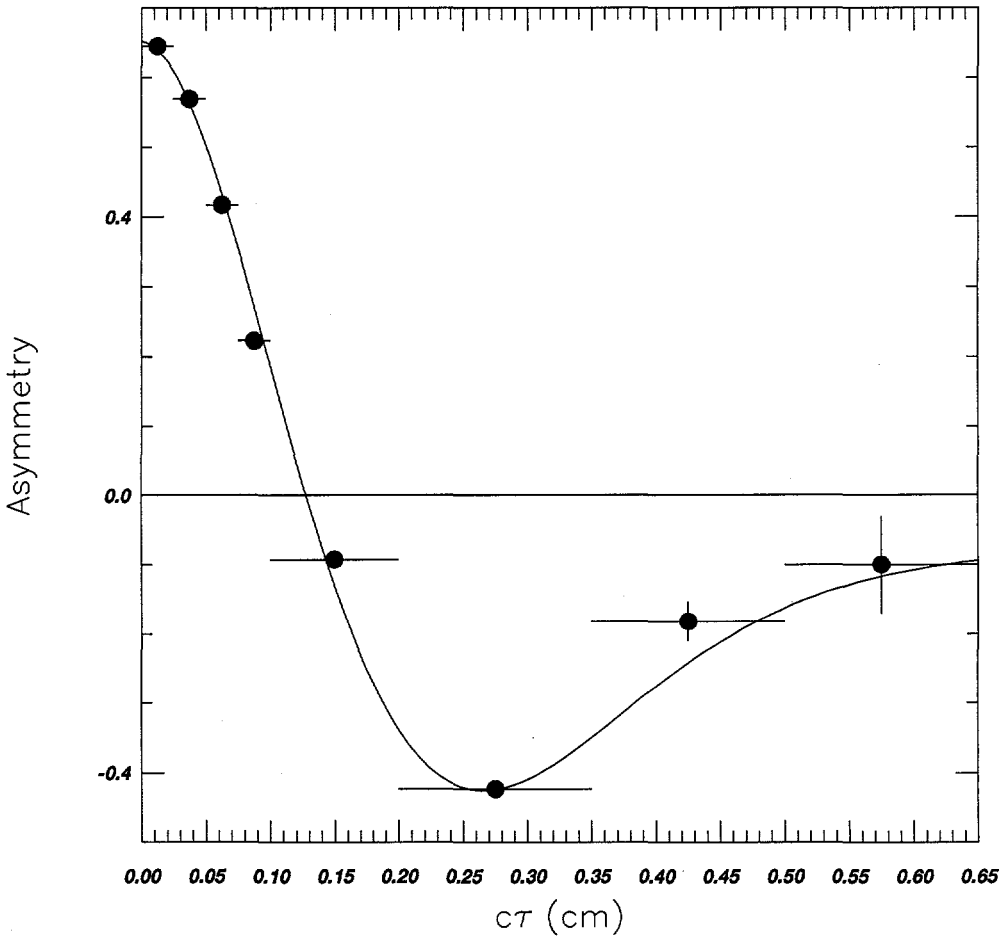

Figure 4-58. The fit result on the binned asymmetry distribution of 1 million pure B_d^0 events. Input ΔM_d is 0.474 and input dilution is 0.67. Output ΔM_d is 0.439 ± 0.001 and $\mathcal{D}_0$ is 0.654 ± 0.001.

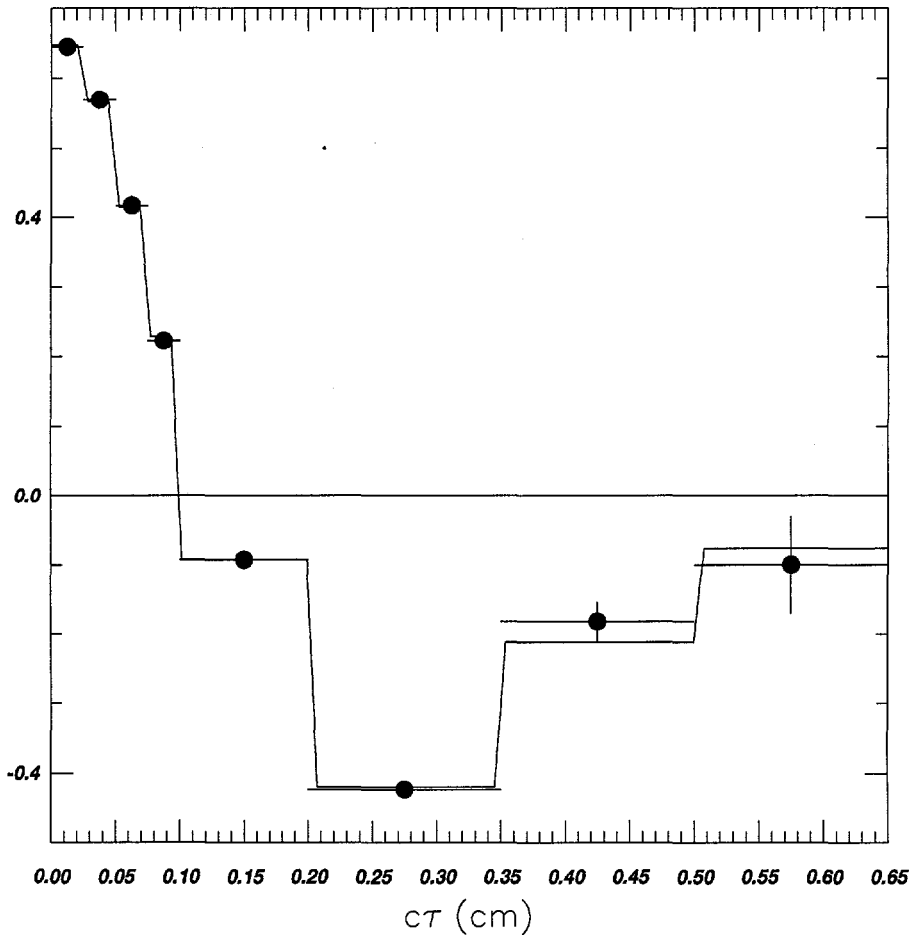

Figure 4-59. The discrete fit result on the binned asymmetry distribution of 1 million pure B_d^0 events. Input ΔM_d is 0.474 and input dilution is 0.67. Output ΔM_d is 0.476 and $\mathcal{D}_0$ is 0.67.

Next, we make a sample of 1 million B^0 with background events where the composition of the backgrounds follow that of the data and we bin the asymmetry distribution of this sample the same way as we bin the data. Figure 4-60 shows the unbinned asymmetry distribution of the sample. The continuous fit on the binned distribution gives $\Delta M_d^{output} = 0.432$ and $D_0^{output} = 0.639$ (Fig. 4-61), but the discrete fit of the binned distribution gives $\Delta M_d^{output} = 0.473$ and $D_0^{output} = 0.670$ (Fig. 4-62). Using the discrete fitting function we can eliminate the binning effect even when the backgrounds are present in the distribution.

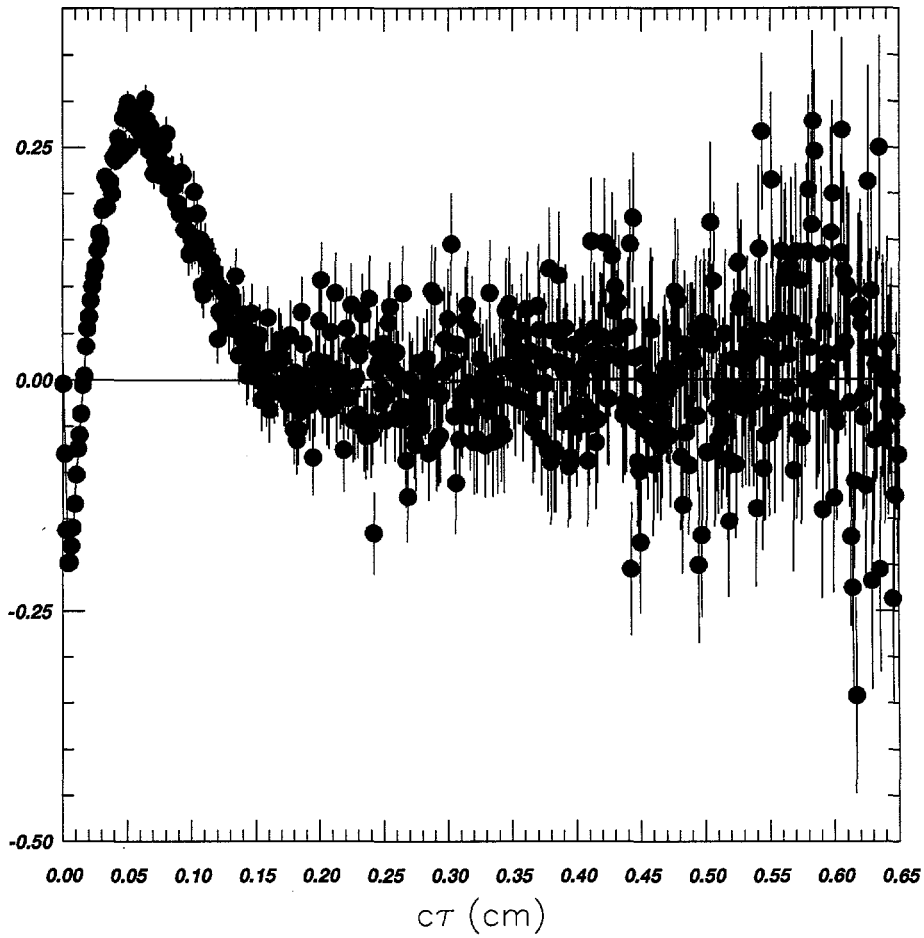

Figure 4-60. The fit result on the unbinned asymmetry distribution of 1 million B^0 plus background events. Input ΔM_d is 0.474 and input dilution is 0.67. Output ΔM_d is 0.474 and $\mathcal{D}_0$ is 0.67.

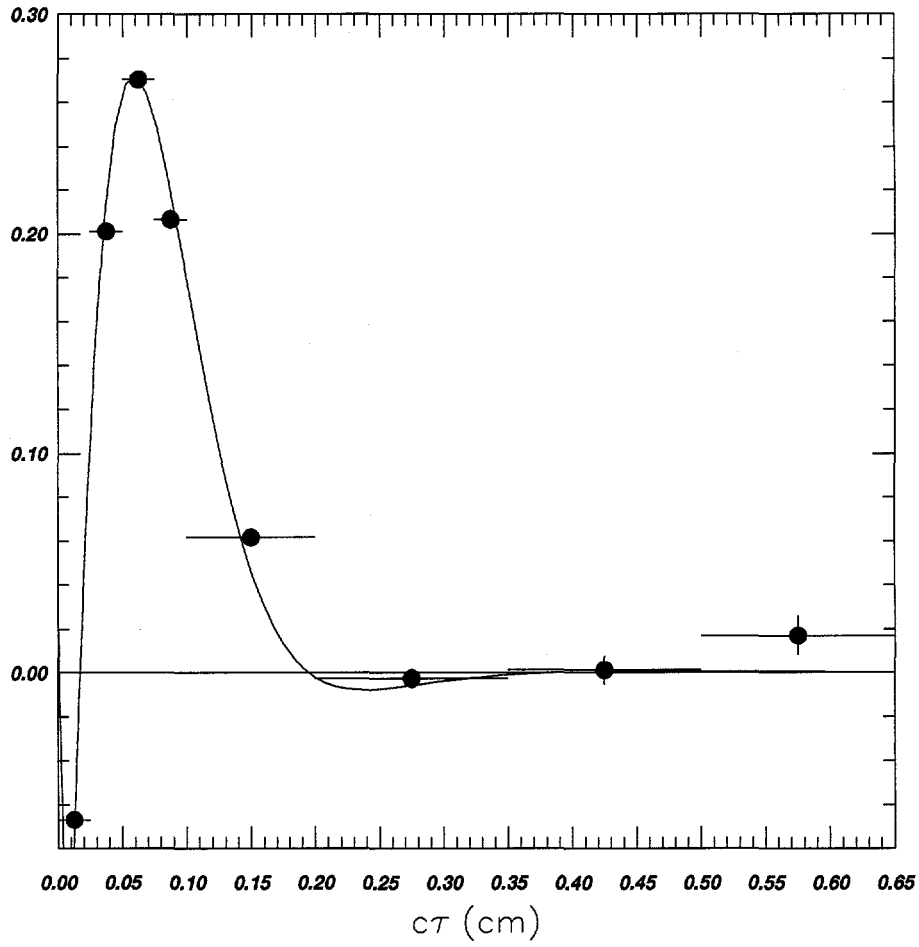

Figure 4-61. The continuos fit result on the binned asymmetry distribution of 1 million B^0 plus background events. Input ΔM_d is 0.474 and input dilution is 0.67. Output ΔM_d is 0.432 and $\mathcal{D}_0$ is 0.64.

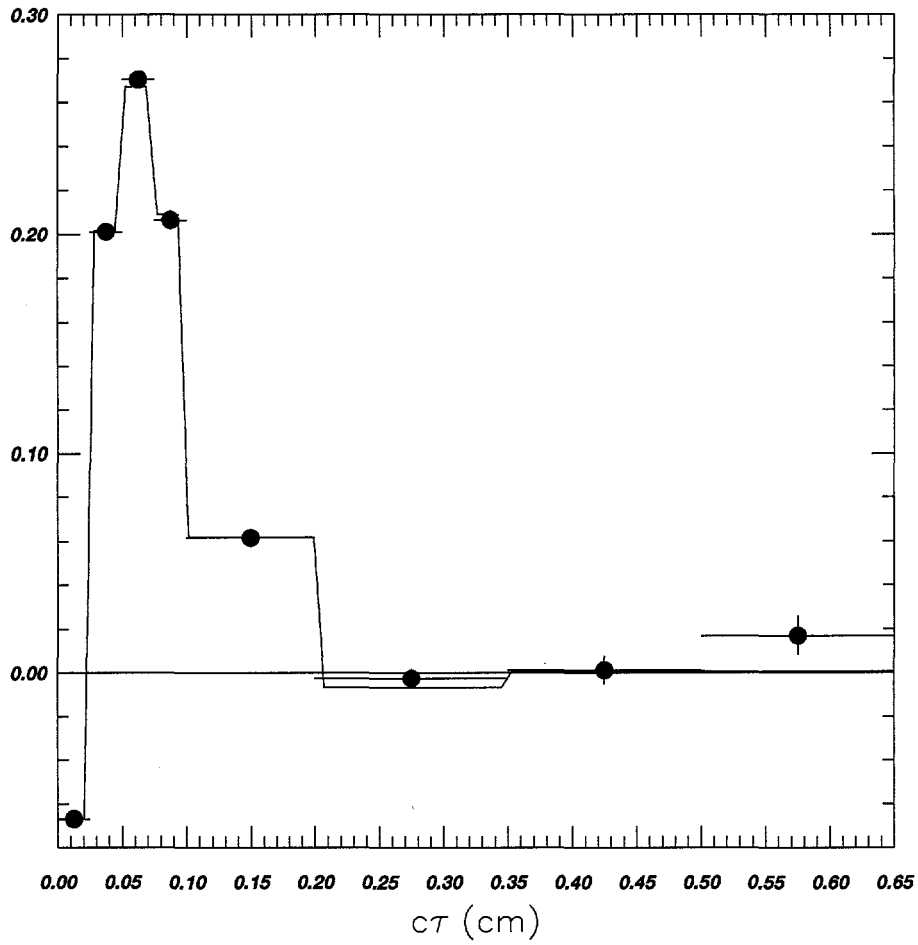

Figure 4-62. The discrete fit result on the binned asymmetry distribution of 1 million B^0 plus background events. Input ΔM_d is 0.474 and input dilution is 0.67. Output ΔM_d is 0.473 and $\mathcal{D}_0$ is 0.67.

Then, to test the fitter's accuracy in extracting the value of ΔM_d of a sample with the same statistical level as the data, we created 1000 such samples. We set the relative amount of the background and signal components and the total number of events (800 events) to be about the same as that estimated in the total electron and muon data. One thousand such samples were produced with input $\Delta M_d = 0.474\ ps^{-1}$ and input $\mathcal{D}_0 = 0.67$. The fitting function is then used to extract the ΔM_d and $\mathcal{D}_0$ of these Monte Carlo samples. The distribution of the fit values of ΔM_d is gaussian with a mean value of $\Delta M_d = 0.476 \pm 0.006\ ps^{-1}$ (Fig. 4-63). The width of this gaussian distribution is $0.164 \pm 0.005\ ps^{-1}$. The width of the ΔM_d distribution can be used to predict the error on the ΔM_d measurement that we may get from the data. Figure 4-65 shows the distribution of the MINOS error [3] of ΔM_d. The pull distribution of ΔM_d using MINOS error is shown in Fig. 4-64.

To study the effect of underestimating or overestimating the $c\bar{c}$ background fraction, we generated 1000 TOYMC samples with $f_{c\bar{c}}^{input} = 0.1166$, $\Delta M_d^{input} = 0.474$, and $D_0^{input} = 0.67$. We fit these samples three times, each time fixing the fraction of $c\bar{c}$ to a different value. The first time with $f_{c\bar{c}}^{fixed} = 0.1166$, the second time with $f_{c\bar{c}}^{fixed} = 0.0869$ and the third time with $f_{c\bar{c}}^{fixed} = 0.1463$. When we fixed the $c\bar{c}$ fraction to its input value (see Fig. 4-66), we obtained the mean values of $\Delta M_d^{fit} = 0.4779 \pm 0.0056$ and $D_0^{fit} = 0.694 \pm 0.005$. When we fixed the $c\bar{c}$ fraction to its lower limit (underestimate), we obtained (see Fig. 4-67), $\Delta M_d^{fit} = 0.4191 \pm 0.0059$ and $D_0^{fit} = 0.536 \pm 0.004$. And when the $c\bar{c}$ fraction is fixed to its upper limit (overestimate), we obtained (Fig. 4-68) $\Delta M_d^{fit} = 0.5440 \pm 0.0059$ and $D_0^{fit} = 0.864 \pm 0.006$. So we can see that ΔM_d may vary by 0.06 when the $f_{c\bar{c}}$ is varied by 3%.

[3] MINOS is the algorithm/method used in the MINUIT minimization program to calculate correct errors of the parameters in general cases, especially when the function to be minimized depends non-linearly on the parameters.

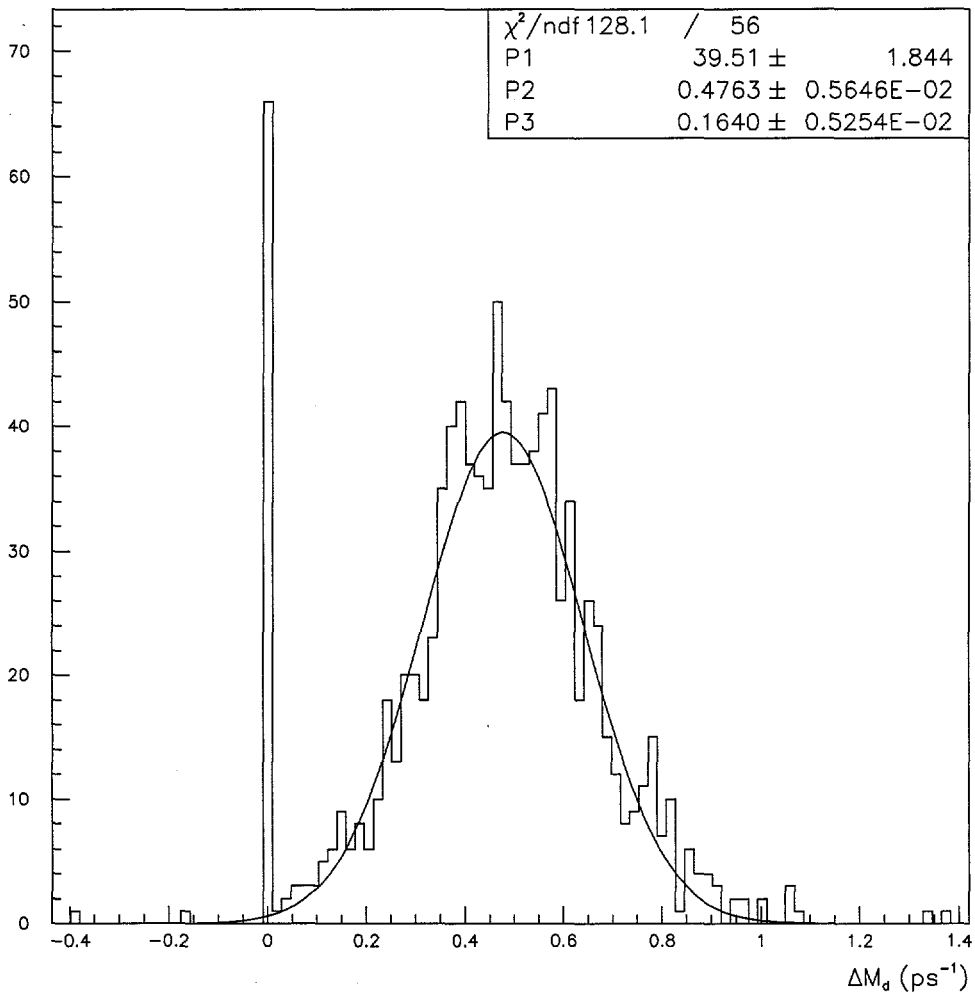

Figure 4-63. ΔM_d distribution for the 1000 TOYMC samples (each with a statistic and composition similar to that of the data). The the dilution parameter in the fitting function is unfixed. The distribution is fitted to a gaussian function. P1 is the area, P2 is the mean and P3 is the width of the gaussian fit.

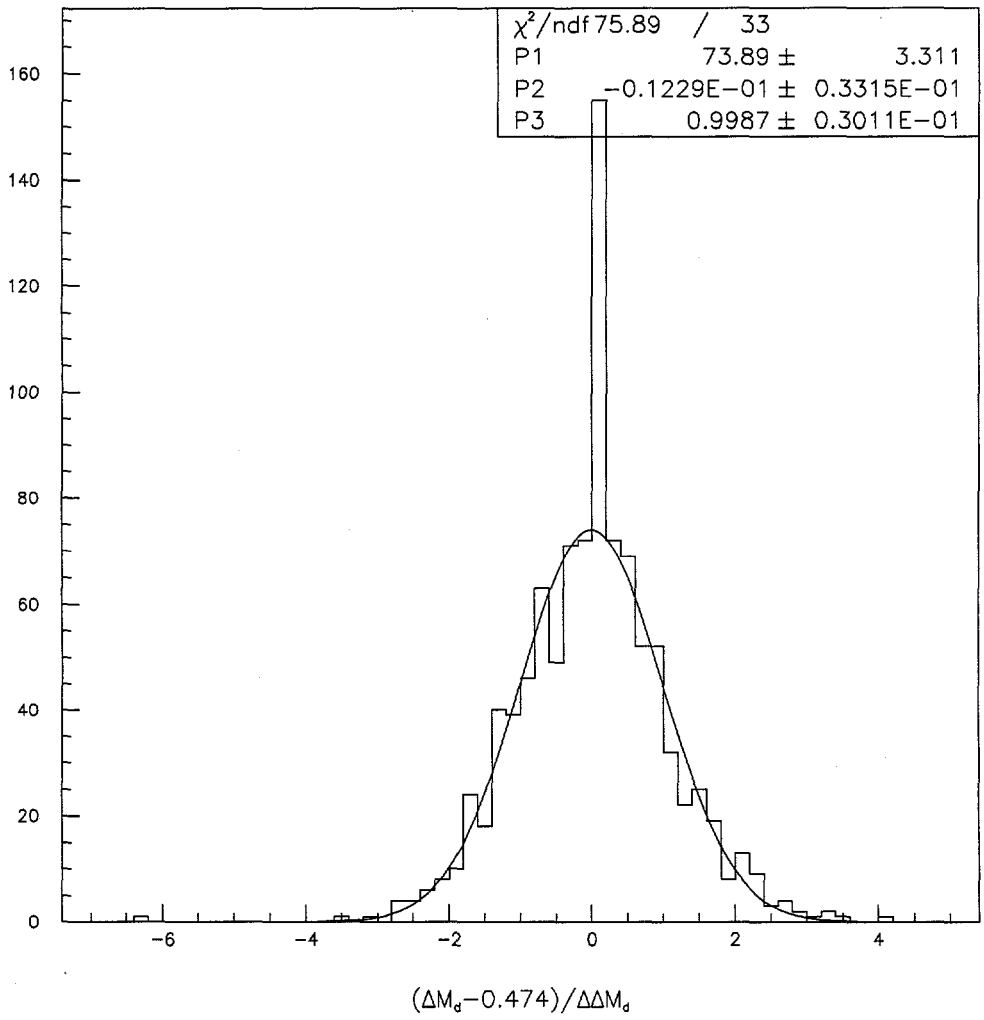

Figure 4-64. ΔM_d pull distribution with error obtained using MINOS.

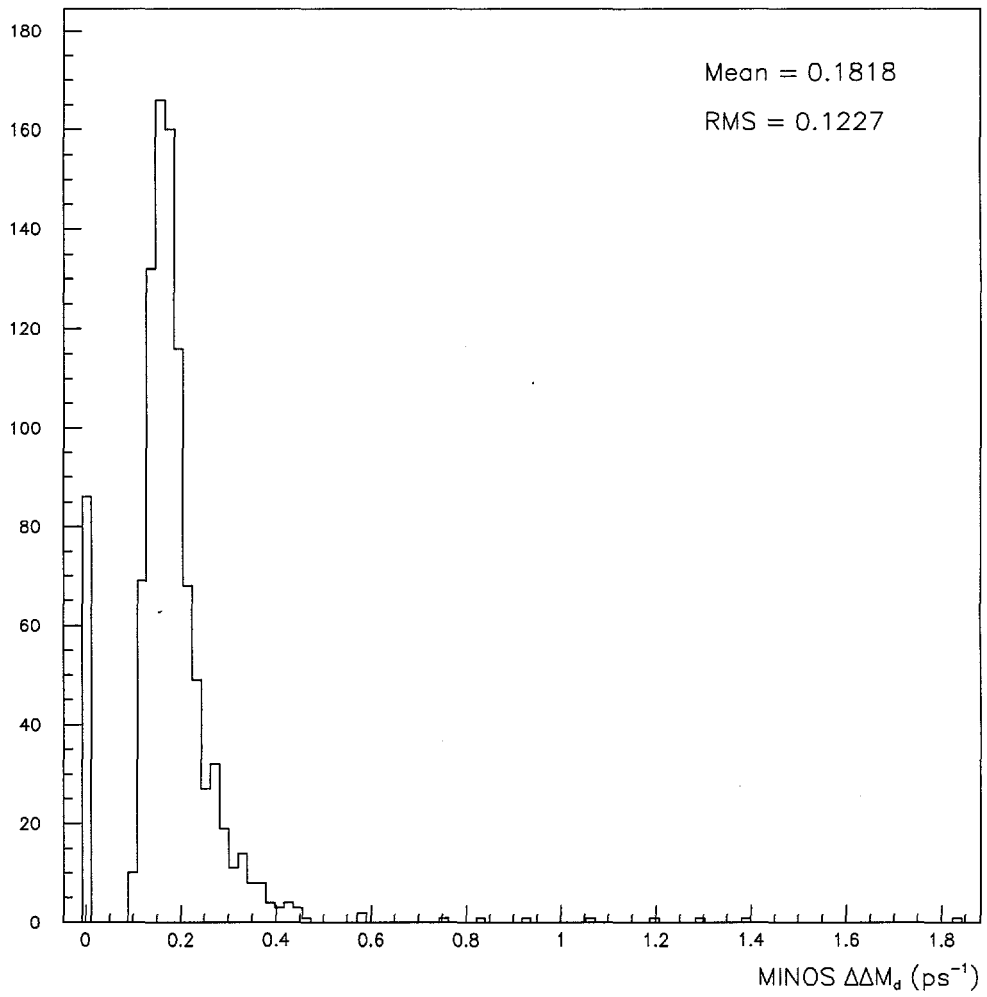

Figure 4-65. ΔM_d MINOS error distribution for the 1000 TOYMC samples.

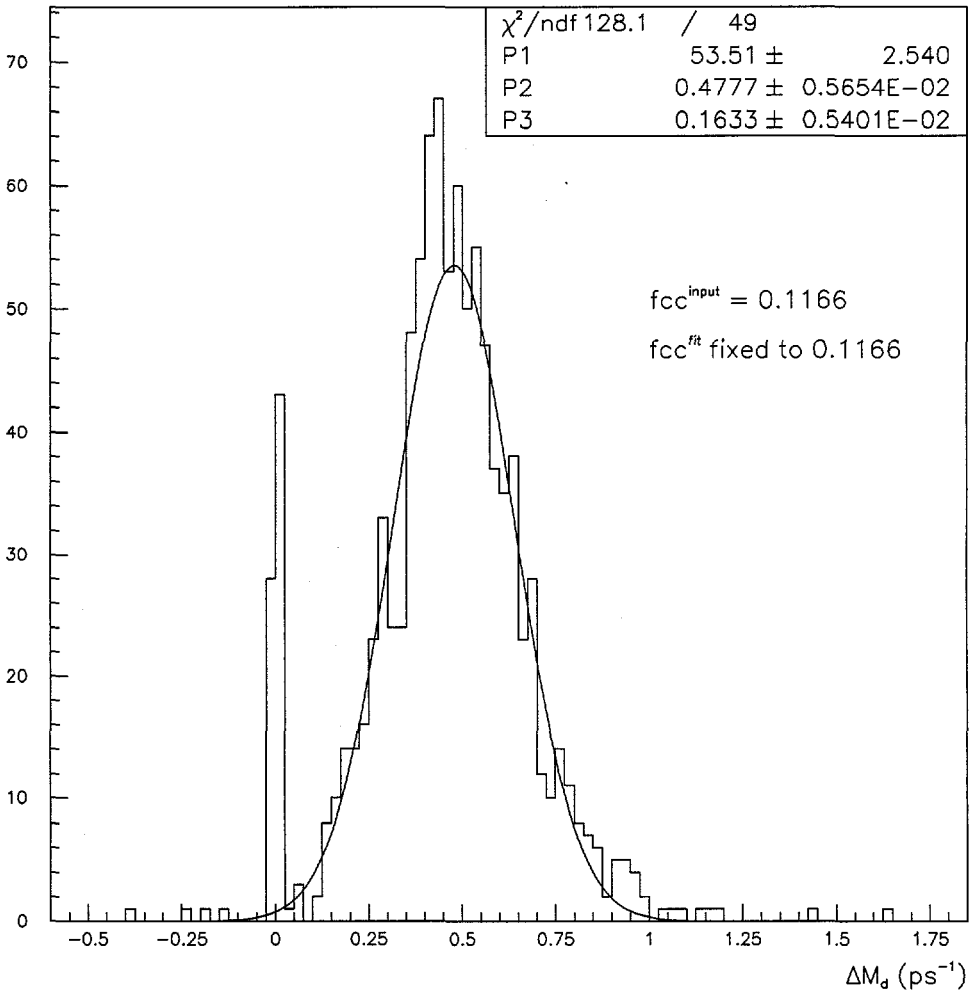

Figure 4-66. ΔM_d distribution for the 1000 TOYMC samples with $f_{c\bar{c}}^{input} = 0.1166$ and $f_{c\bar{c}}^{fixed} = 0.1166$. P1 is the area, P2 is the mean and P3 is the width of the gaussian fit.

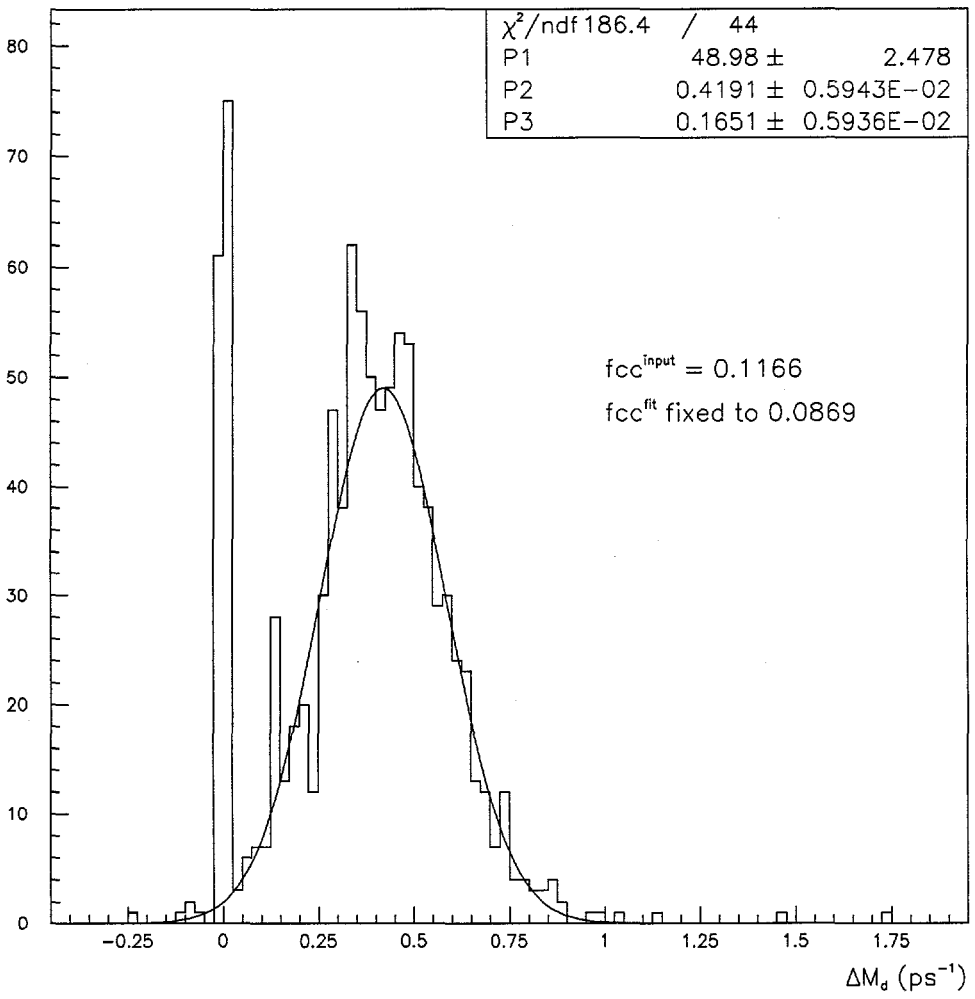

Figure 4-67. ΔM_d distribution for the 1000 TOYMC samples with $f_{c\bar{c}}^{input} = 0.1166$ and $f_{c\bar{c}}^{fixed} = 0.0869$. P1 is the area, P2 is the mean and P3 is the width of the gaussian fit.

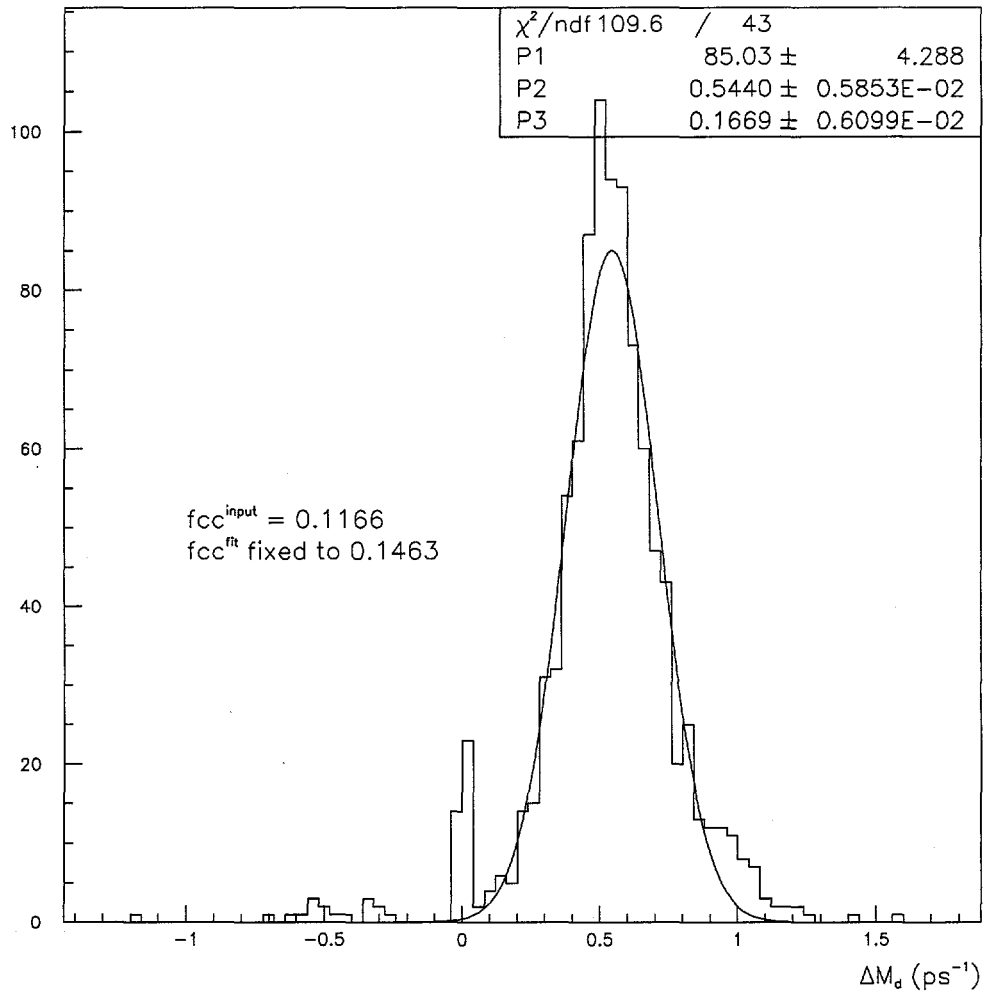

Figure 4-68. ΔM_d distribution for the 1000 TOYMC samples with $f_{c\bar{c}}^{input} = 0.1166$ and $f_{c\bar{c}}^{fixed} = 0.1463$. P1 is the area, P2 is the mean and P3 is the width of the gaussian fit.

H. Background Handling

The $c\tau_B$ distributions for both the like sign and unlike sign sample in the signal region have not yet been background corrected. The like sign background consists of combinatorics (fake D^*), sequential leptons, leptons coming from B^0's that have mixed, D^*'s coming from other B meson species. The unlike sign background consists of combinatorics, sequential leptons, leptons from B^0's that have mixed and leptons and D^*'s coming from $c\bar{c}$ productions. The combinatoric background can be subtracted out from the signal. To subtract a background from a signal distribution, we need to know the number and the distribution shape of the background for that quantity. The $c\tau_B$ distribution shape of the background in the signal region can be obtained by taking the $c\tau_B$ distribution in the sideband region of the D^* signal. In this case we use $\mid MDIF \mid < 0.002\ GeV/c^2$ as the D^* signal region and $-0.008 < MDIF < -0.002$ and $0.002 < MDIF < 0.008$ as the lower and upper sideband region respectively. The shape of the combinatoric background in the signal region should be the same as that in the sideband region. By interpolating the sideband data to the signal region we can estimate the number of the combinatoric background in the signal region. But to be more accurate, we simultaneously fit the MDIF distribution and the PTREL distribution in estimating the number of combinatorics. Knowing the $c\tau$ shape and the number of the combinatorics in the signal region, then we can properly subtract the combinatoric out of the $c\tau$ distribution in the signal region. The $c\bar{c}$ shape can be obtained from a Monte Carlo generated sample. These $c\bar{c}$ Monte Carlo generated events are then filtered, selected and reconstructed by the reconstruction code. A distribution of those events passing the reconstruction code can then be made and thus the $c\bar{c}$ estimated $c\tau$ shape can be obtained. The number of $c\bar{c}$ in the signal region is estimated by performing a simultaneous fit on the unlike sign sample distributions of PTREL and MDIF. Normalizing the shape of the Monte Carlo $c\bar{c}$ $c\tau$ distribution by the number of $c\bar{c}$ in the signal region gives us the $c\tau$ distribution of the $c\bar{c}$ for the data. Subtracting the $c\tau$ distribution in the unlike sign sample signal region with this $c\bar{c}$ distribution cleans our sample from $c\bar{c}$ background. The sequential background and the leptons from B^0's that

have mixed are not subtracted out, however the effect of these two types of background on the asymmetry is just to dilute the amplitude of the oscillation, hence the term "dilution." The presence of these backgrounds in the $c\tau$ distribution does not significantly affect the measurement of the frequency of the oscillation which is related to the quantity ΔM_d.

Another way to account for the background, is to fit the background unsubtracted asymmetry distribution with the shape of the signal and background components. The fraction of the background components can be fixed to the values obtained from the PTREL and MDIF methods. In this analysis, we decided to keep the backgrounds in our asymmetry distribution.

Since we have a negligible rate of fake lepton, the dilution of the oscillation amplitude then comes mostly from sequentials and mixing on the lepton tagging side. The lepton sign mistag rate is proportional to the rate of sequential decay and the rate of B mixing on the away side. The statements above can be clearly explained by considering the following processes, which are possible candidates for the away side :

1. $\bar{B}^0 \rightarrow l^-$
2. $\bar{B}^0 \rightarrow D^+ \rightarrow l^+$
3. $\bar{B}^0 \rightarrow B^0 \rightarrow l^+$
4. $\bar{B}^0 \rightarrow B^0 \rightarrow D^- \rightarrow l^-$

The first process is a direct decay of a B meson to a lepton (the process of interest for our signal) where the sign of the lepton correctly tags the flavor of the B^0 on the D^* side at production time. The second process is a sequential decay. Since we have no means of distinguishing a sequential decay from a direct decay, the sign of the lepton would incorrectly tag the flavor of the B^0 on the D^* side at production time. The third process shows that the B meson on the away side has mixed. This also leads to a mistag effect. The fourth process shows that a mixing followed by a sequential decay has occured to the B meson on the away side. In this case, the sign of the lepton correctly tags the flavor of the B^0 on the D^* side at production time.

It is clear that the effective mistag rate is the sum of the rates of the second and third possibilities. Hence we have a mistag rate $R = R_{seq}(1-\bar{\chi})+\bar{\chi}(1-R_{seq})$, where $R_{seq} = 2.85\pm0.09\%$ (from Monte Carlo) is the sequential electron fraction and $\bar{\chi} = f_d\chi_d + f_s\chi_s = 0.126 \pm 0.008$ is the average probability of mixing for the lepton side. We can then calculate the expected dilution for electron :

$$\mathcal{D}_o^{limit} = \quad 1 - 2 * R = \quad 0.71 \pm 0.02 \tag{4-40}$$

while for muon with an average sequential fraction of $6.93 \pm 0.11\%$, we expect

$$\mathcal{D}_o^{limit} = \quad 1 - 2 * R = \quad 0.64 \pm 0.02 \tag{4-41}$$

With 43.7% of the sample being electron and 56.3% muon, we we have the average expected dilution for the combined sample to be :

$$\mathcal{D}_o^{limit} = \quad 1 - 2 * R = \quad 0.67 \pm 0.01 \tag{4-42}$$

A measurement of the dilution, as given by the asymmetry fitting function's parameter for the dilution, different from the expected value may show the effect of other processess not taken into account, like the fake lepton rate.

CHAPTER 5.

Results and Conclusions

A. Asymmetry Fitting Result

We fit the asymmetry distribution for the electron data, the muon data and the combined electron and muon data. For the electron data, the fit result for the ΔM_d is $0.58 \pm^{0.20}_{0.25}\ ps^{-1}$ and for the dilution D_0 is $0.90\pm^{0.26}_{0.25}$. The chisquare of fit is 7.5 for 4 degrees of freedom with a confidence level of 11.1%. Figure 5-1 shows the result for the fit on the electron data drawn as a continuous function. For the muon data, the fit result for the ΔM_d is $0.52 \pm^{0.23}_{0.22}\ ps^{-1}$ and for the dilution D_0 is $0.45\pm^{0.17}_{0.16}$. The chisquare of the fit is 6.7 for 4 degrees of freedom with a confidence level of 15.5% Figure 5-2 shows the result for the fit on the muon data drawn as a continuous function. For the combined electron and muon data, the fit result for the ΔM_d is $0.55 \pm^{0.15}_{0.16}\ ps^{-1}$ and for the dilution D_0 is $0.64\pm^{0.15}_{0.14}$. The chisquare of the fit is 7.0 for 4 degrees of freedom with a confidence level of 13.6%. Figure 5-3 shows the result for the fit on the combined electron and muon data drawn as a continuous function.

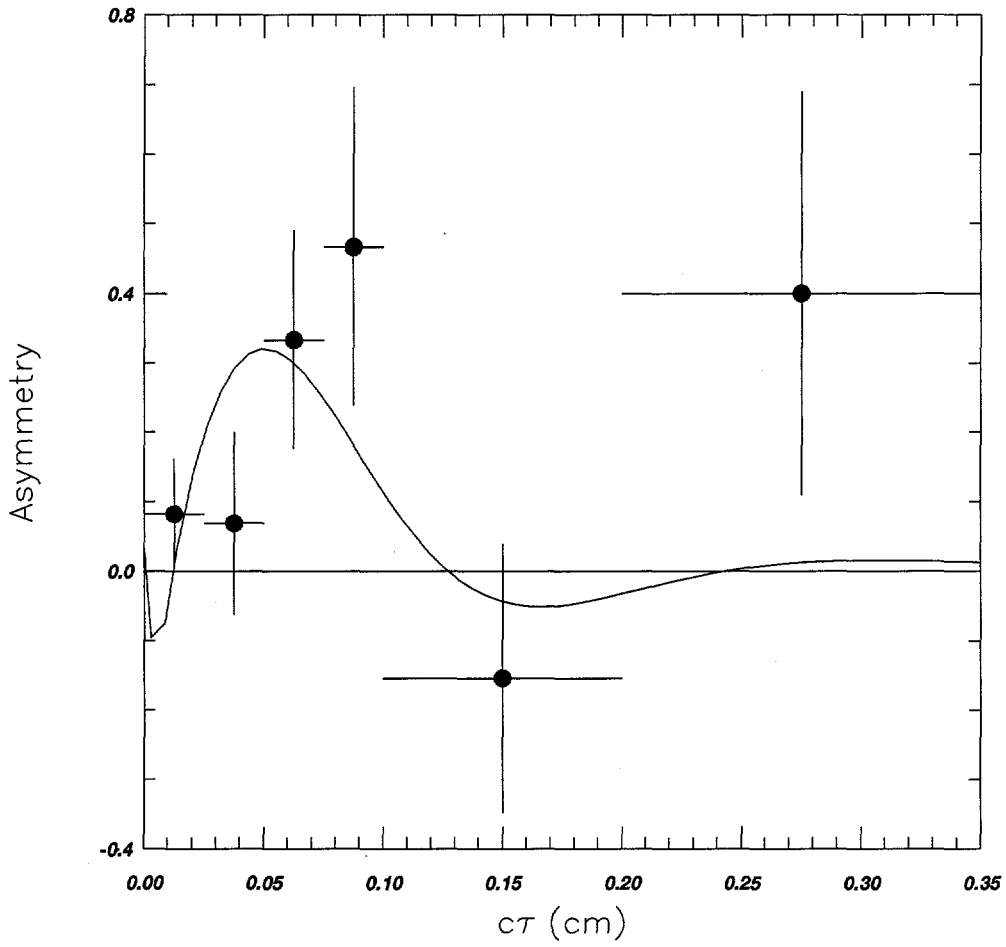

Figure 5-1. The result for the fit on the electron Run 1a and 1b data drawn as a continuous function. No fitting is done here.

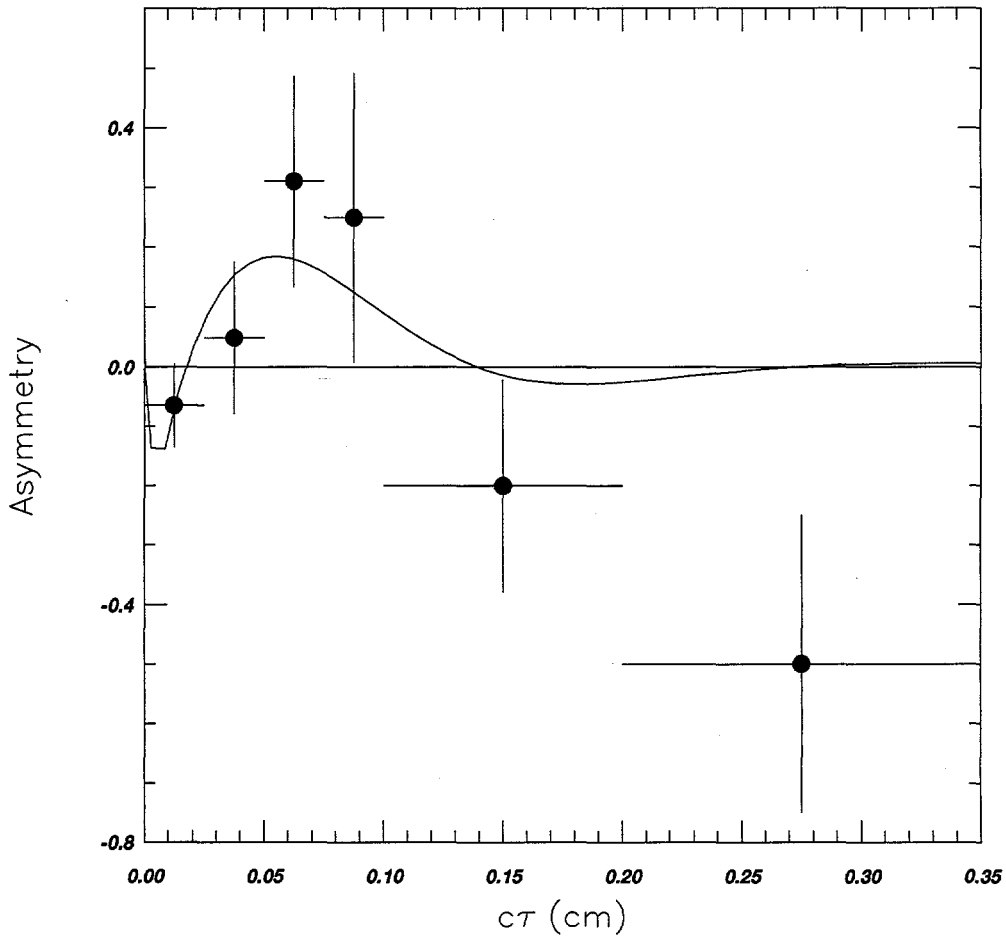

Figure 5-2. The result for the fit on the muon Run 1a and 1b data drawn as a continuous function. No fitting is done here.

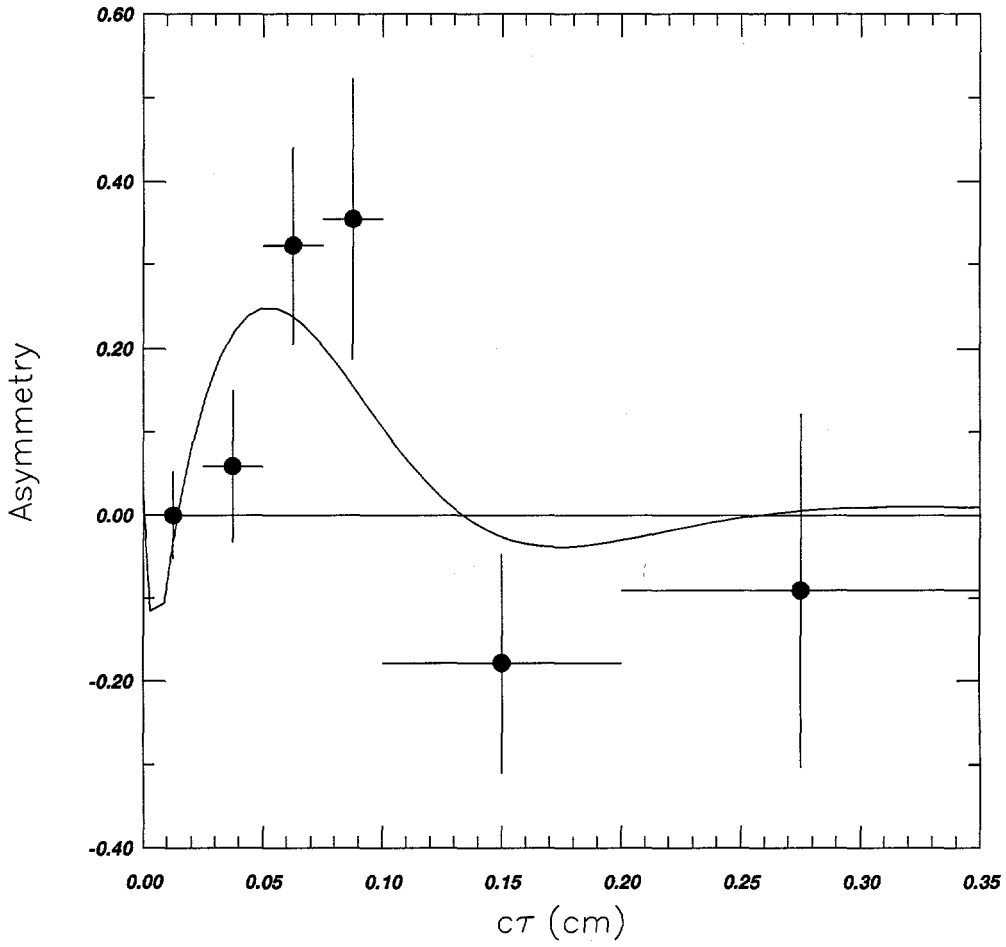

Figure 5-3. The result for the fit on the electron and muon Run 1a and 1b data drawn as a continuous function. No fitting is done here.

The sample composition determination gives an estimate of the $c\bar{c}$ and combinatoric fraction in the $c\tau$ distribution of the signal region with some uncertainties. If we take these uncertainties into account, then we obtain the systematic errors associated with our determination of ΔM_d and D_0. We find this systematic error by varying the $c\bar{c}$ and combinatoric background fractions within their limits. Table 5-1 shows the result for the combined electron and muon sample. The results for the electron sample are found in Table 5-2 and for the muon sample they are found in Table 5-3.

f_{com}	f_{cc}	ΔM_d (ps^{-1})	D_0
0.5066	0.1166	$0.5458\pm^{0.1529}_{0.1571}$	$0.6367\pm^{0.1457}_{0.1394}$
0.5066	0.0869	$0.5027\pm^{0.1687}_{0.1849}$	$0.4933\pm^{0.1296}_{0.1241}$
0.5066	0.1463	$0.5859\pm^{0.1423}_{0.1405}$	$0.8018\pm^{0.1657}_{0.1574}$
0.4831	0.1166	$0.5457\pm^{0.1524}_{0.1560}$	$0.6055\pm^{0.1376}_{0.1318}$
0.4831	0.0869	$0.5028\pm^{0.1686}_{0.1833}$	$0.4703\pm^{0.1229}_{0.1178}$
0.4831	0.1463	$0.5851\pm^{0.1419}_{0.1394}$	$0.7595\pm^{0.1555}_{0.1480}$
0.5301	0.1166	$0.5458\pm^{0.1534}_{0.1580}$	$0.6716\pm^{0.1552}_{0.1476}$
0.5301	0.0869	$0.5026\pm^{0.1688}_{0.1865}$	$0.5190\pm^{0.1369}_{0.1311}$
0.5301	0.1463	$0.5867\pm^{0.1426}_{0.1415}$	$0.8500\pm^{0.1773}_{0.1681}$

Table 5-1. ΔM_d and Dilution systematic error due to the variations of $f_{c\bar{c}}$ and f_{com} for the $e + \mu$ sample.

f_{com}	f_{cc}	ΔM_d (ps^{-1})	D_0
0.5513	0.1191	$0.5752\pm^{0.2036}_{0.2507}$	$0.9041\pm^{0.2637}_{0.2467}$
0.5513	0.0776	$0.4956\pm^{0.2399}_{1.231}$	$0.6543\pm^{0.2214}_{0.2111}$
0.5513	0.1606	$0.6379\pm^{0.1821}_{0.1993}$	$1.2167\pm^{0.3211}_{0.2970}$
0.5142	0.1191	$0.5771\pm^{0.2033}_{0.2481}$	$0.8303\pm^{0.2386}_{0.2239}$
0.5142	0.0776	$0.4980\pm^{0.2401}_{1.236}$	$0.6061\pm^{0.2028}_{0.1940}$
0.5142	0.1606	$0.6388\pm^{0.1816}_{0.1971}$	$1.1035\pm^{0.2860}_{0.2652}$
0.5884	0.1191	$0.5734\pm^{0.2041}_{0.2535}$	$0.9951\pm^{0.2959}_{0.2750}$
0.5884	0.0776	$0.4931\pm^{0.2401}_{1.226}$	$0.7127\pm^{0.2444}_{0.2315}$
0.5884	0.1606	$0.6370\pm^{0.1822}_{0.2015}$	$1.3621\pm^{0.3666}_{0.3377}$

Table 5-2. ΔM_d and Dilution systematic error due to the variations of $f_{c\bar{c}}$ and f_{com} for the electron sample.

f_{com}	f_{cc}	ΔM_d (ps^{-1})	D_0
0.4681	0.1144	$0.5216\pm^{0.2306}_{0.2171}$	$0.4463\pm^{0.1720}_{0.1646}$
0.4681	0.0726	$0.4776\pm^{0.2820}_{0.3087}$	$0.2806\pm^{0.1492}_{0.1436}$
0.4681	0.1562	$0.5648\pm^{0.2071}_{0.1824}$	$0.6413\pm^{0.2014}_{0.1908}$
0.4379	0.1144	$0.5203\pm^{0.2285}_{0.2135}$	$0.4202\pm^{0.1608}_{0.1543}$
0.4379	0.0726	$0.4775\pm^{0.2808}_{0.3016}$	$0.2646\pm^{0.1404}_{0.1355}$
0.4379	0.1562	$0.5620\pm^{0.2050}_{0.1793}$	$0.6007\pm^{0.1865}_{0.1774}$
0.4983	0.1144	$0.5231\pm^{0.2322}_{0.2211}$	$0.4762\pm^{0.1849}_{0.1764}$
0.4983	0.0726	$0.4773\pm^{0.2832}_{0.3155}$	$0.2987\pm^{0.1590}_{0.1527}$
0.4983	0.1562	$0.5675\pm^{0.2091}_{0.1855}$	$0.6888\pm^{0.2188}_{0.2065}$

Table 5-3. ΔM_d and Dilution systematic error due to the variations of $f_{c\bar{c}}$ and f_{com} for the muon sample.

In addition, there are uncertainties in the fractions of the D^*'s coming from the different B species, which also contribute a systematic error to the measurement. In principle we can find this systematic error by varying the fraction of charged B and fraction of B_s in the D^* signal within their limits. The central values of these fractions are obtained using the Pythia Monte Carlo and the QQ decay table. The limits are assumed to be about 50% of the central value. Table 5-4 shows the results for the combined electron and muon sample. The results for the electron sample are found in Table 5-5 and for the muon sample they are found in Table 5-6.

$f_{B^\pm}$	f_{B_s}	ΔM_d (ps^{-1})	D_0
0.3108	0.0471	$0.5458\pm^{0.1529}_{0.1571}$	$0.6367\pm^{0.1457}_{0.1394}$
0.3108	0.0271	$0.5438\pm^{0.1512}_{0.1558}$	$0.6244\pm^{0.1427}_{0.1366}$
0.3108	0.0671	$0.5481\pm^{0.1545}_{0.1585}$	$0.6495\pm^{0.1489}_{0.1423}$
0.1608	0.0471	$0.4969\pm^{0.1217}_{0.1304}$	$0.6486\pm^{0.1434}_{0.1390}$
0.1608	0.0271	$0.4958\pm^{0.1211}_{0.1299}$	$0.6353\pm^{0.1405}_{0.1360}$
0.1608	0.0671	$0.4978\pm^{0.1224}_{0.1308}$	$0.6621\pm^{0.1468}_{0.1418}$
0.4608	0.0471	$0.5940\pm^{0.1971}_{0.1944}$	$0.6098\pm^{0.1427}_{0.1356}$
0.4608	0.0271	$0.5911\pm^{0.1940}_{0.1915}$	$0.5994\pm^{0.1403}_{0.1332}$
0.4608	0.0671	$0.5967\pm^{0.2008}_{0.1972}$	$0.6202\pm^{0.1454}_{0.1380}$

Table 5-4. ΔM_d and Dilution systematic error due to the variations of $f_{B^\pm}$ and f_{B_s} for the $e + \mu$ sample.

$f_{B^\pm}$	f_{B_s}	ΔM_d (ps^{-1})	D_0
0.3108	0.0471	$0.5752\pm^{0.2036}_{0.2507}$	$0.9041\pm^{0.2637}_{0.2467}$
0.3108	0.0271	$0.5714\pm^{0.2017}_{0.2491}$	$0.8848\pm^{0.2582}_{0.2414}$
0.3108	0.0671	$0.5790\pm^{0.2059}_{0.2520}$	$0.9236\pm^{0.2701}_{0.2521}$
0.1608	0.0471	$0.4916\pm^{0.1659}_{0.2207}$	$0.8856\pm^{0.2512}_{0.2407}$
0.1608	0.0271	$0.4898\pm^{0.1654}_{0.2199}$	$0.8666\pm^{0.2461}_{0.2352}$
0.1608	0.0671	$0.4933\pm^{0.1666}_{0.2212}$	$0.9049\pm^{0.2572}_{0.2457}$
0.4608	0.0471	$0.6605\pm^{0.2626}_{0.2933}$	$0.8928\pm^{0.2606}_{0.2416}$
0.4608	0.0271	$0.6553\pm^{0.2582}_{0.2897}$	$0.8762\pm^{0.2566}_{0.2372}$
0.4608	0.0671	$0.6654\pm^{0.2677}_{0.2969}$	$0.9094\pm^{0.2648}_{0.2459}$

Table 5-5. ΔM_d and Dilution systematic error due to the variations of $f_{B^\pm}$ and f_{B_s} for the electron sample.

$f_{B^\pm}$	f_{B_s}	ΔM_d (ps^{-1})	D_0
0.3108	0.0471	$0.5209\pm^{0.2277}_{0.2156}$	$0.4383\pm^{0.1686}_{0.1614}$
0.3108	0.0271	$0.5208\pm^{0.2279}_{0.2155}$	$0.4544\pm^{0.1756}_{0.1678}$
0.3108	0.0671	$0.5228\pm^{0.2332}_{0.2193}$	$0.4544\pm^{0.1756}_{0.1678}$
0.1608	0.0471	$0.4916\pm^{0.1659}_{0.2207}$	$0.8856\pm^{0.2512}_{0.2407}$
0.1608	0.0271	$0.4898\pm^{0.1654}_{0.2199}$	$0.8666\pm^{0.2461}_{0.2352}$
0.1608	0.0671	$0.4933\pm^{0.1666}_{0.2212}$	$0.9049\pm^{0.2572}_{0.2457}$
0.4608	0.0471	$0.6553\pm^{0.2582}_{0.2897}$	$0.8762\pm^{0.2566}_{0.2372}$
0.4608	0.0271	$0.6605\pm^{0.2626}_{0.2933}$	$0.8928\pm^{0.2606}_{0.2416}$
0.4608	0.0671	$0.6654\pm^{0.2677}_{0.2969}$	$0.9094\pm^{0.2648}_{0.2459}$

Table 5-6. ΔM_d and Dilution systematic error due to the variations of $f_{B^\pm}$ and f_{B_s} for the muon sample.

B. Conclusion

In conclusion, our analysis of the time dependent B_d^0 $\bar{B}_d^0$ mixing using opposite side lepton and D^* mesons obtained $\Delta M_d = 0.55 \pm^{0.15}_{0.16} (stat) \pm 0.04 (syst1) \pm 0.05 (syst2)\ ps^{-1}$ and $\mathcal{D}_0 = 0.64 \pm^{0.15}_{0.14} (stat) \pm^{0.21}_{0.17} (syst1) \pm^{0.03}_{0.04} (syst2)$. This analysis has used 100 pb^{-1} of data collected with the CDF detector from the $p\bar{p}$ collisions at $\sqrt{s} = 1.8\ TeV$.

Presented in Fig. 5-4 is a compilation of other measurements of the mixing parameter ΔM_d from different analyses in CDF. Fig. 5-5 shows our ΔM_d measurement compared to that of different experiments around the world. It is clear from these comparisons that our ΔM_d measurement is consistent with the world average. However, the statistical error of our present work is substantially larger than of the other measurements. A future effort will concentrate on combining the results of the present work with another closely related CDF analysis.

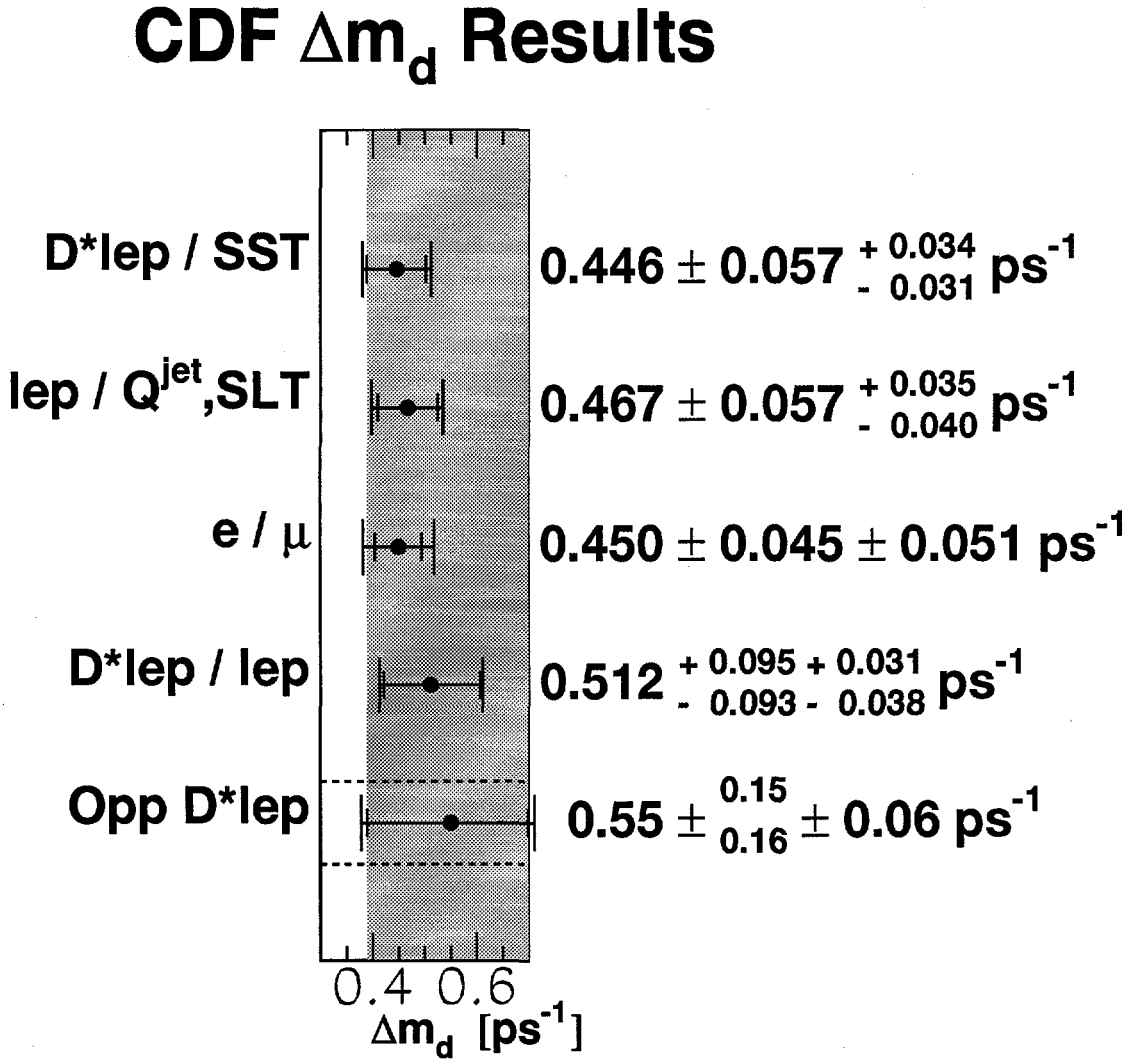

Figure 5-4. A comparison of our opposite Lepton D^* ΔM_d measurement with measurements from other analyses in CDF, namely the Same Side Tagging, Lepton Jet Charge Tagging / Soft Lepton Tagging, Electron Muon Analysis and Dilepton D^*.

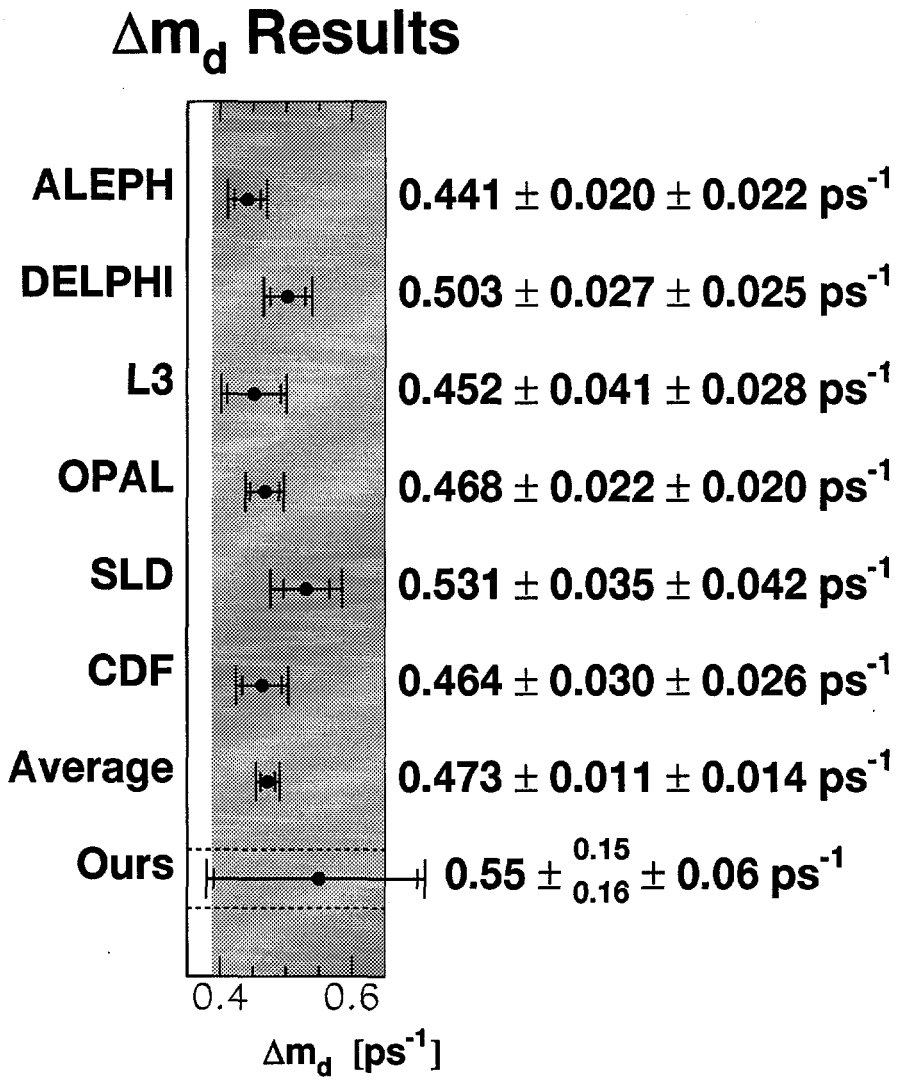

Figure 5-5. A comparison of our opposite Lepton D^* ΔM_d measurement with measurements from ALEPH, DELPHI, L3, OPAL, SLD, CDF and the world average.

APPENDIX A.

Lepton Identification and $D*$ Reconstruction Cuts

A. Electron Identification Cuts

- SVX tracks
- $3D$ tracks.
- CEM tracks.
- $E_{Had}/E_{EM} \leq 0.04$.
- $Lshr \leq 0.2$.
- Strip profile fit $\chi^2 \leq 10$.
- Wire profile fit $\chi^2 \leq 15$.
- Track $P_t \geq 6.0\,GeV/c$.
- $X_{CES} - X_{CTC} < 3.0$ cm.
- $Z_{CES} - Z_{CTC} < 5.0$ cm.
- Photon Conversion Rejection

B. Muon Identification Cuts

- SVX tracks
- Both CMU and CMP tracks.
- CTC-CMU track match in ϕ fit $\chi^2 \leq 9$.

- CTC-CMU track match in z fit $\chi^2 \leq 12$.
- CTC-CMP track match in ϕ fit $chi^2 \leq 9$.
- Track $P_t \geq 6.0\,GeV/c$.

C. D^0 and D^* Reconstruction Requirements

- SVX tracks requirements
- Kaon track $P_t > 1\,GeV/c$
- Pion track $P_t > 1\,GeV/c$
- Kaon and pion system $P_t > 2\,GeV/c$
- Kaon and pion vertex fit $\chi^2 > 0.01$
- $L_{xy}/\sigma_{L_{xy}} > 1.0$
- $\sigma_{L_{xy}} * 5.2790/P_{t\,K\pi} < 0.05cm$
- $1.84 < M_{K\,\pi} < 1.89GeV/c^2$
- Electron, kaon and pion system mass $M_{e\,K\,\pi} > 5.5\,GeV/c^2$
- $\mid MDIF \mid < 0.002\,GeV/c^2$
- Pion impact parameter significance $d/\sigma_d > 1.0$
- Kaon impact parameter significance $d/\sigma_d > 1.0$

APPENDIX B.

$< L_{xy_D} >$ and $< L_{xy_B} >$ Formula

The formula for $< L_{xy_D} >$, the calculated average 2 dimensional decay length of the reconstructed D^0 is derived from :

$$\begin{aligned} < L_{xy_D} > &= \frac{\int_0^{L_{xy}} L_{xy_D} P(L_{xy_D}) dL_{xy_D}}{\int_0^{L_{xy}} P(L_{xy_D}) dL_{xy_D}} && \text{(B-1)} \\ &= L_{xy}/(1 - e^{(a*L_{xy}/P_{t_{K\pi}}))} + P_{t_{K\pi}}/a \\ a &= 149.89 - 117.6 * CORRF && \text{(B-2)} \\ P(L_{xy_D}) &= C(L_{xy}) e^{-\alpha L_{xy_D}} && \text{(B-3)} \\ \alpha &= \alpha_D - \alpha_B && \text{(B-4)} \\ &= (\frac{M_D}{c\tau_D} - \frac{M_B * CORRF}{c\tau_B})/P_{t_D} \end{aligned}$$

$P(L_{xy_D})$ is the probability of having a certain L_{xy_D} and L_{xy_B} given a measured value of L_{xy}. If P_D is the probability distribution of D^0 decay length and P_B is the probability distribution of B^0 decay length, then

$$\begin{aligned} P(L_{xy_D}) &= P_D P_B && \text{(B-5)} \\ &= \alpha_D e^{-\alpha_D L_{xy_D}} \; \alpha_B e^{-\alpha_B (L_{xy} - L_{xy_D})} \\ &= C(L_{xy}) e^{-\alpha L_{xy_D}} \end{aligned}$$

It is straight forward to show that

$$\begin{aligned} < L_{xy_B} > &= L_{xy} - < L_{xy_D} > && \text{(B-6)} \\ &= L_{xy} \, (\frac{1}{\xi} + \frac{1}{1 - exp(\xi)}) \\ \xi &= -a \, \frac{L_{xy}}{P_{t_D}} && \text{(B-7)} \end{aligned}$$

$$RMSL_{xy_B} = (< L_{xy_B}^2 > - < L_{xy_B} >^2)^{\frac{1}{2}} \quad \text{(B-8)}$$

$$= L_{xy}(\frac{1}{\xi^2} - \frac{1}{(exp(\frac{\xi}{2}) - exp(\frac{\xi}{2}))^2})^{\frac{1}{2}}$$

$$< L_{xy_B}^2 > = \frac{\int_0^{L_{xy}} L_{xy_B}^2 P(L_{xy_B}) dL_{xy_B}}{\int_0^{L_{xy}} P(L_{xy_B}) dL_{xy_B}} \quad \text{(B-9)}$$

$$= L_{xy}^2(\frac{2}{\xi^2} + \frac{\frac{2}{\xi} + 1}{1 - exp(\xi)})$$

APPENDIX C.

Sample Composition Fit Results

As discussed earlier in the data analysis chapter, in the case of the like sign sample, we constrain the number of $b\bar{b}$ leptons (direct plus sequential) in the PTREL distribution to the area of the gaussian signal in the MDIF distribution. The number of combinatoric background events in the PTREL distribution is constrained to the number of the combinatoric events in the signal region of the MDIF distribution. The simultaneous fit applied to the unlike (opposite) sign sample proceeds in an identical fashion to the fit described for the like sign sample, with the exception that the $c\bar{c}$ background must be included in the fit. In this case, the area of the gaussian peak now consists of both $b\bar{b}$ and $c\bar{c}$ events. Fig. C-1 shows the MDIF distribution of the like sign electron sample, fitted simultaneously with the corresponding PTREL distribution (Fig.C-2). Figs. C-3 and C-4 are the unlike sign electron MDIF distribution and PTREL distribution respectively, fitted simultaneously as well. Fig. C-5 showing the like sign muon MDIF distribution is fitted simultaneously with the corresponding PTREL distribution (Fig. C-6). Fig. C-7 and C-8, are the unlike sign muon MDIF and PTREL distributions respectively (also simultaneously fitted.)

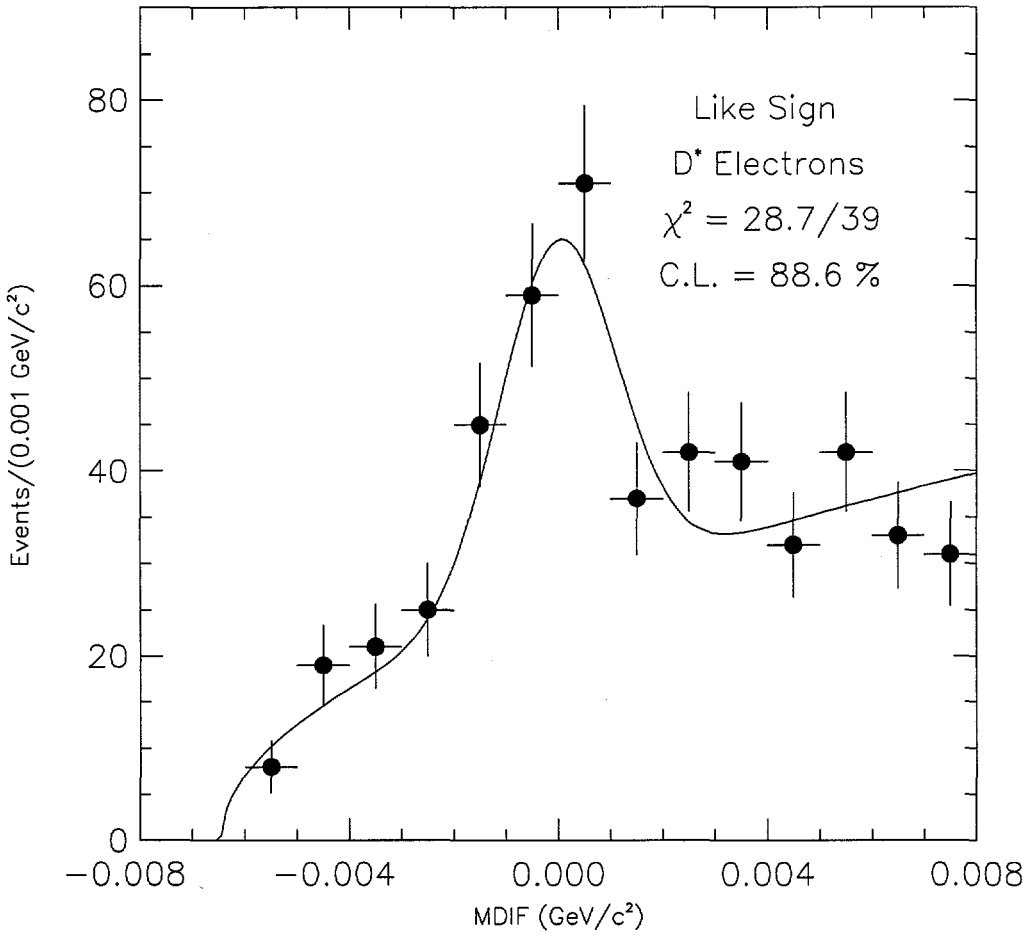

Figure C-1. MDIF plot of the like sign Run 1a and 1b e sample fitted with a gaussian and threshold (power) function. This fit is simultaneously done with the fit on the LS e PTREL distribution. See also Fig. C-2.

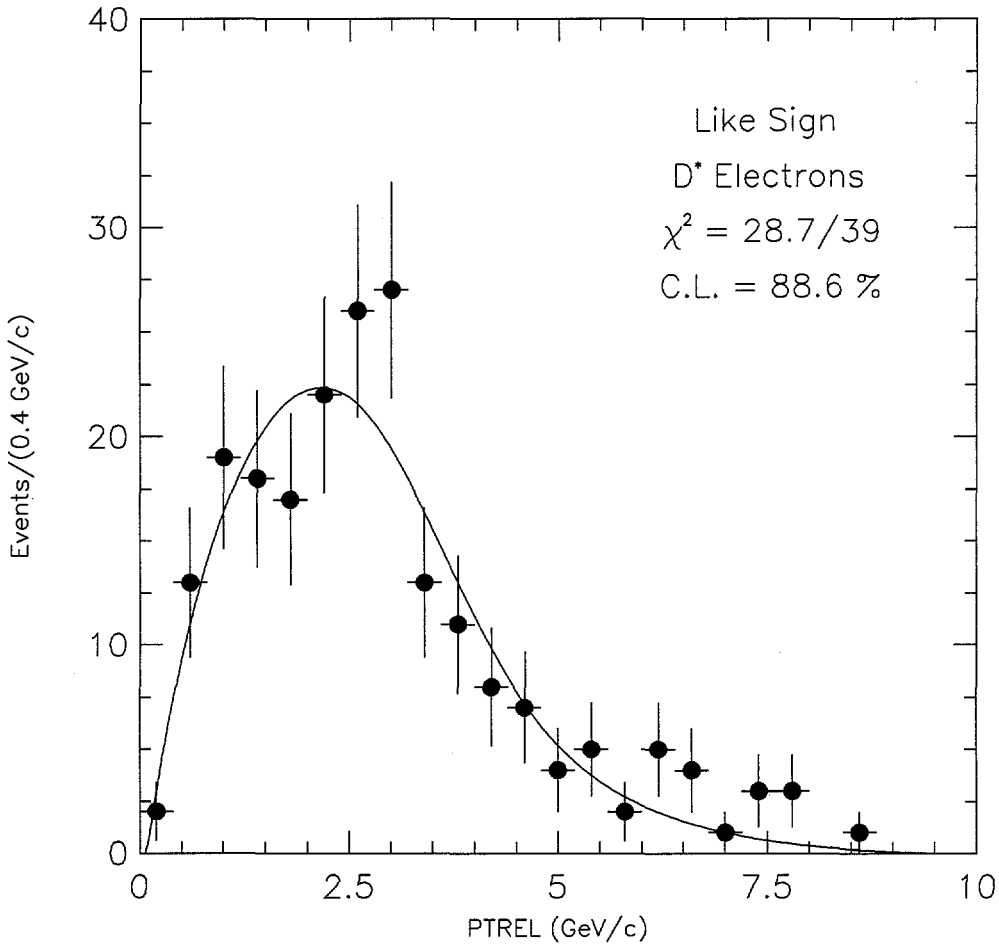

Figure C-2. PTREL Plot of the like sign Run 1a and 1b e sample. This distribution is fitted to a linear combination of $b\bar{b}$ electron PTREL function and electron PTREL function in the sideband region of MDIF plot. This fit is simultaneously done with the fit on MDIF plot. See also Fig. C-1.

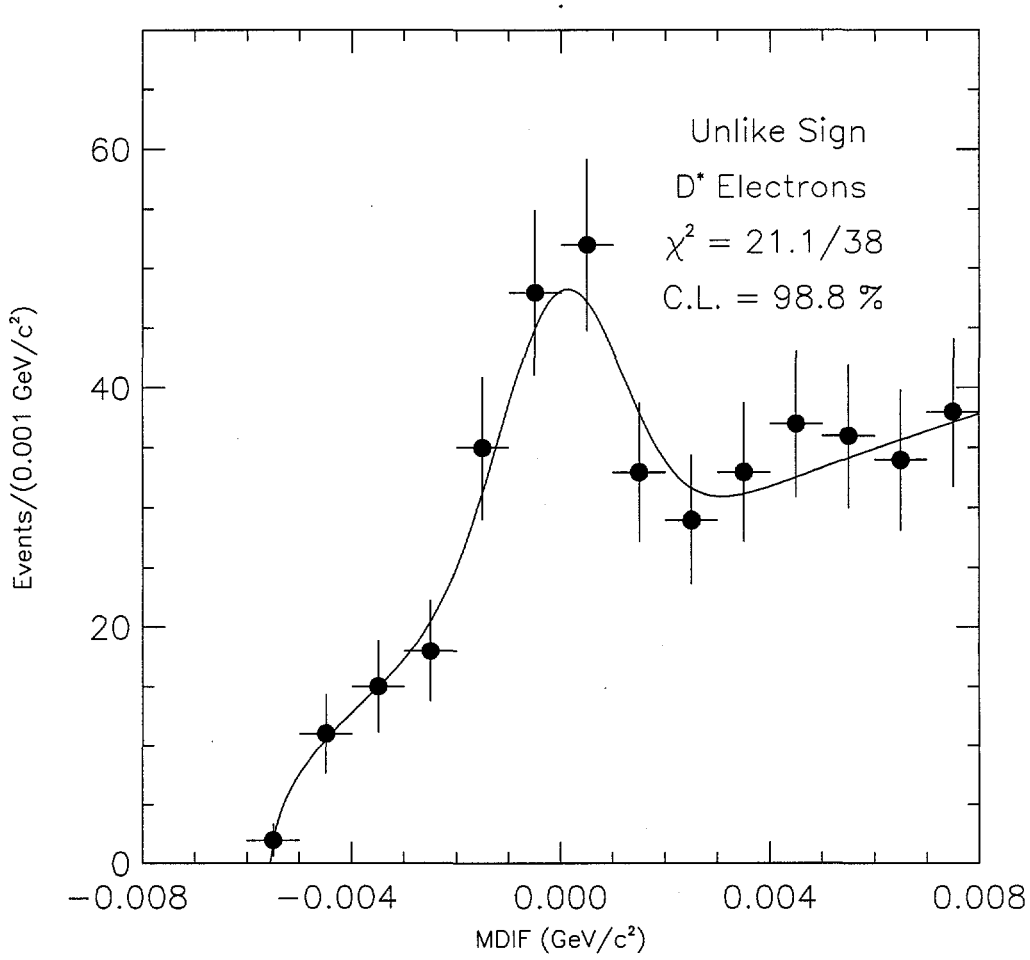

Figure C-3. MDIF plot of the unlike sign Run 1a and 1b e sample fitted with a gaussian and threshold (power) function. This fit is simultaneously done with the fit on the unlike sign e PTREL distribution. The PTREL distribution is fitted to a linear combination of $b\bar{b}$ electron PTREL function, $c\bar{c}$ electron PTREL function and electron PTREL function in the sideband region of MDIF plot. See also Fig. C-4.

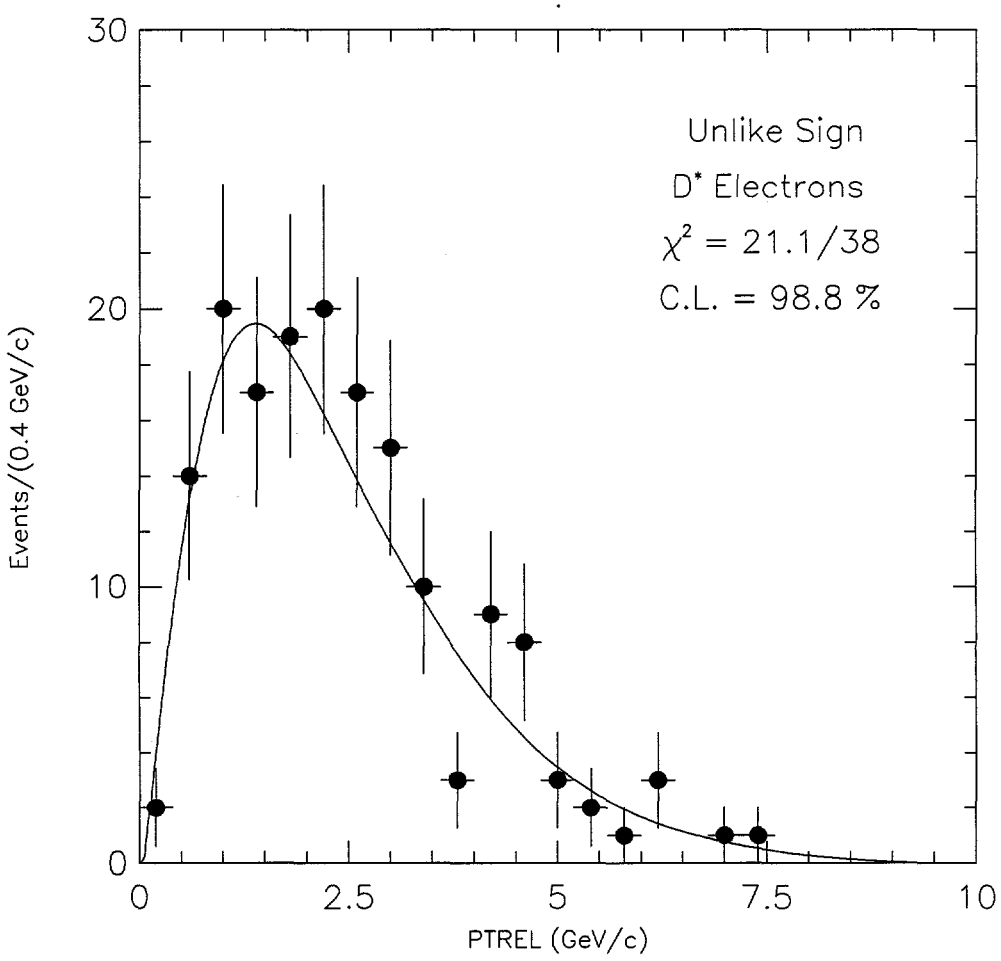

Figure C-4. PTREL plot of the unlike sign Run 1a and 1b e sample. This distribution is fitted to a linear combination of $b\bar{b}$ electron PTREL function, $c\bar{c}$ electron PTREL function and electron PTREL function in the sideband region of MDIF plot. This fit is simultaneously done with the fit on MDIF plot. See also Fig. C-3.

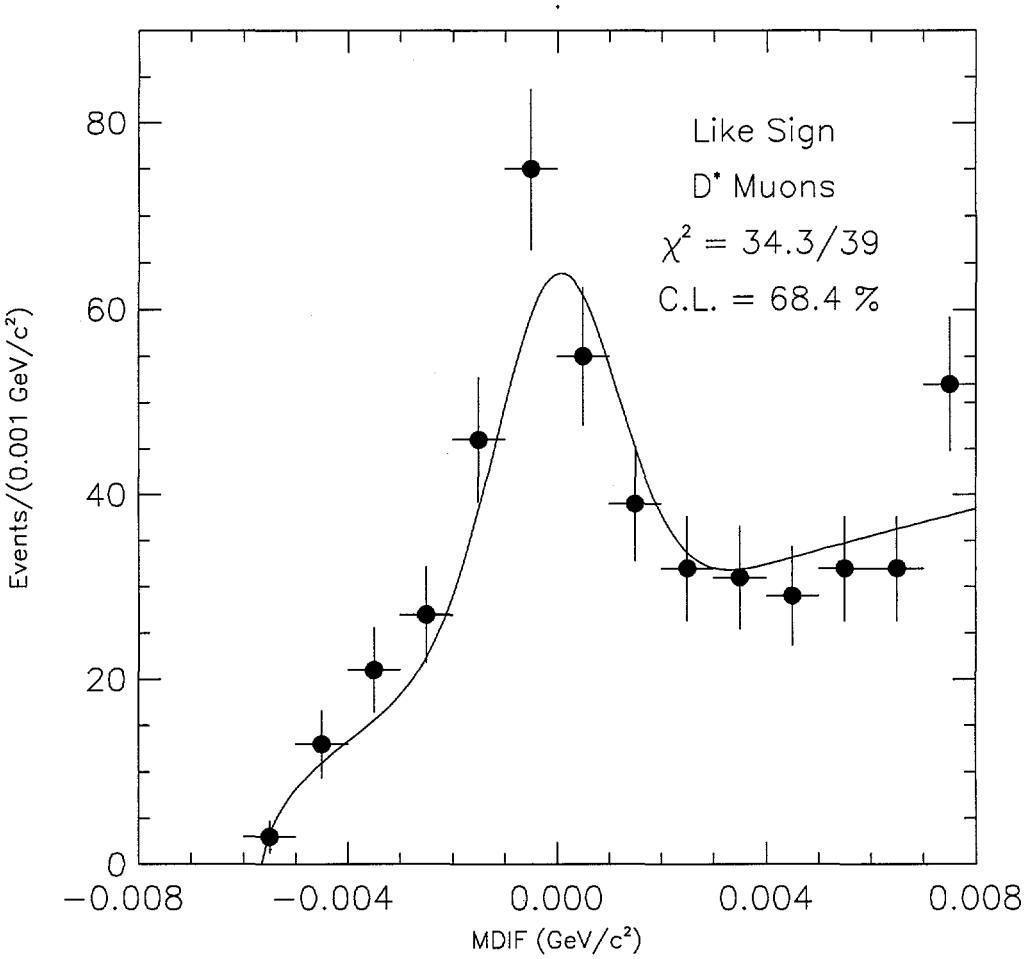

Figure C-5. MDIF Plot of like sign Run 1a and 1b μ sample fitted with Gaussian and Threshold (Power) Function. This fit is simultaneously done with the fit on the LS μ PTREL distribution. See also Fig. C-6.

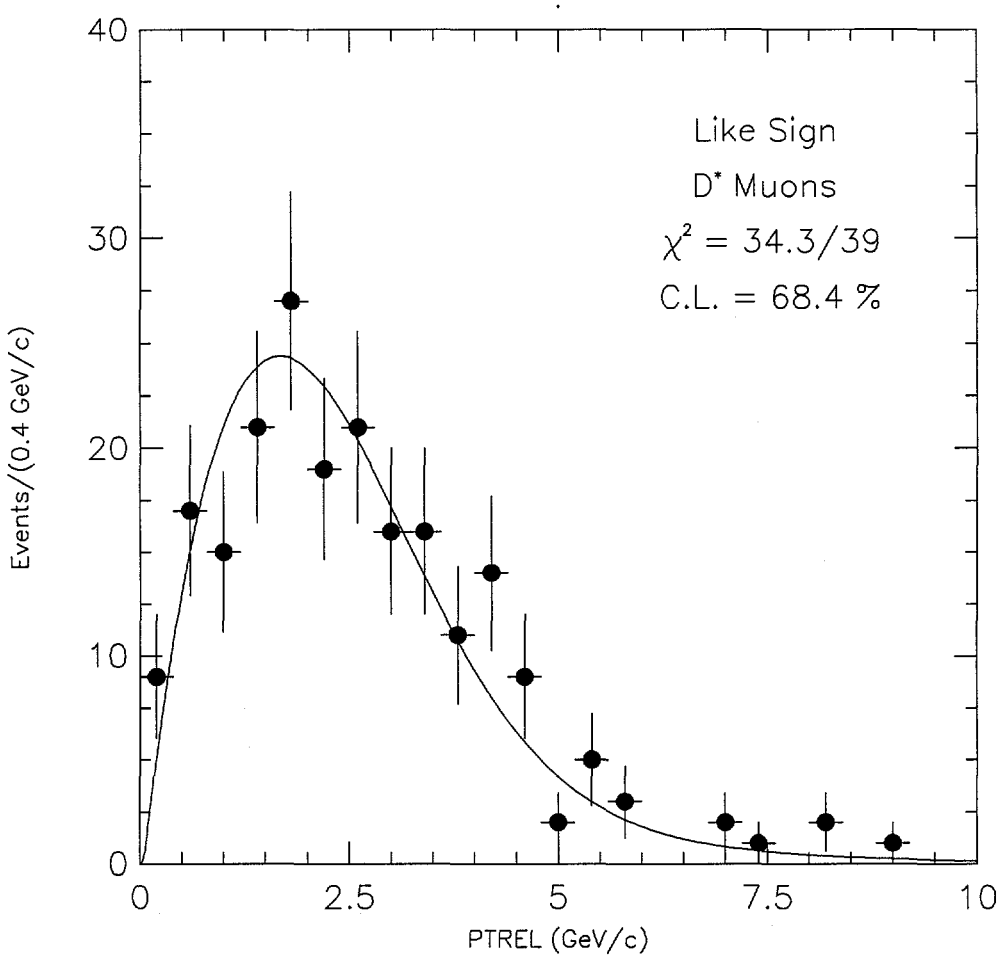

Figure C-6. PTREL Plot of like sign Run 1a and 1b μ sample. This distribution is fitted to a linear combination of $b\bar{b}$ muon PTREL function and muon PTREL function in the sideband region of MDIF plot. This fit is simultaneously done with the fit on MDIF plot. See also Fig. C-5.

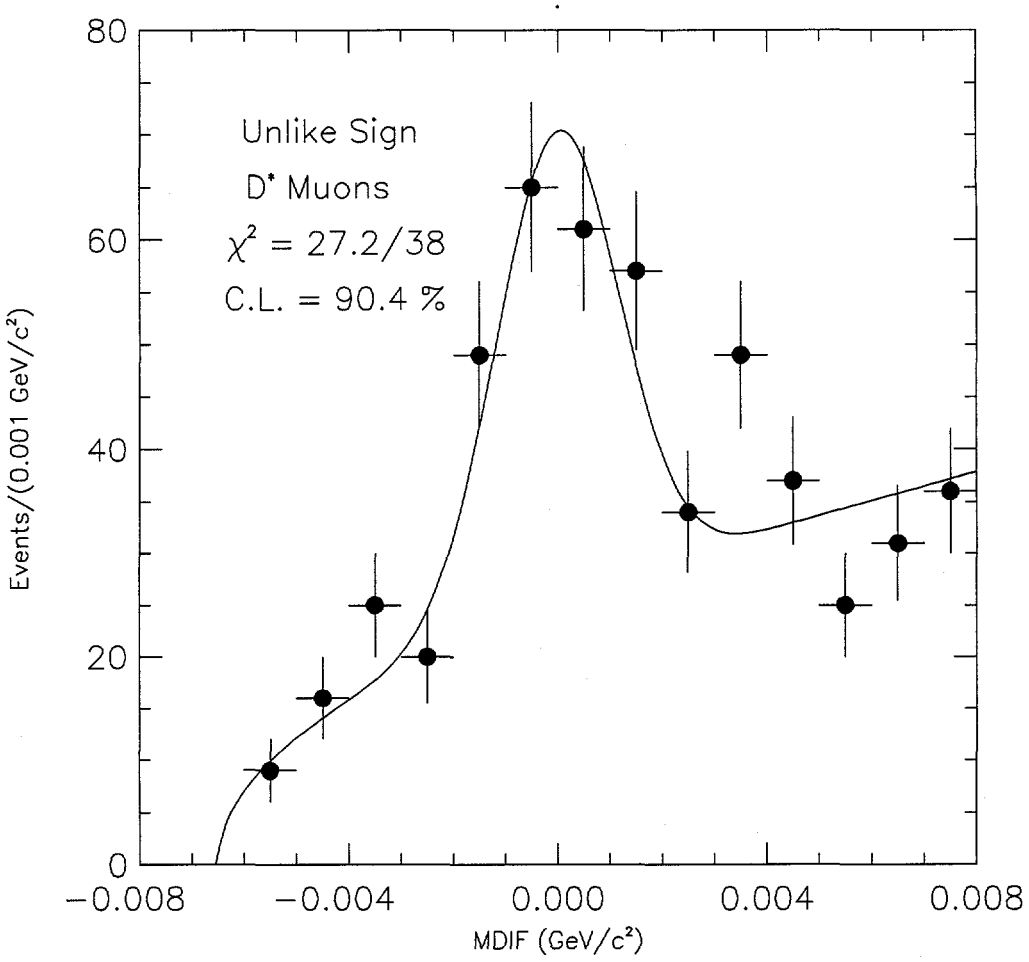

Figure C-7. MDIF Plot of the unlike sign Run 1a and 1b μ sample fitted with a gaussian and threshold (power) function. This fit is simultaneously done with the fit on the unlike sign μ PTREL distribution. The PTREL distribution is fitted to a linear combination of $b\bar{b}$ muon PTREL function, $c\bar{c}$ muon PTREL function and muon PTREL function in the sideband region of MDIF plot. See also Fig. C-8.

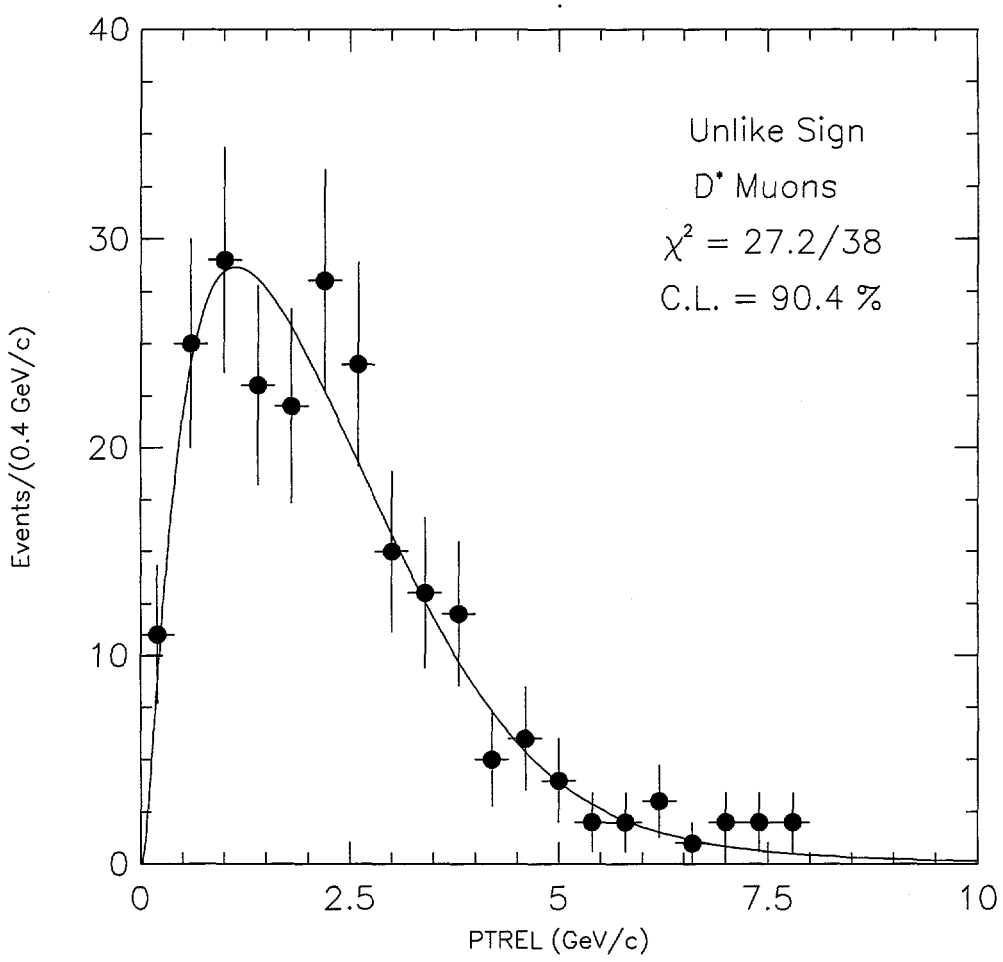

Figure C-8. PTREL Plot of unlike sign Run 1a and 1b μ sample. This distribution is fitted to a linear combination of $b\bar{b}$ muon PTREL function, $c\bar{c}$ muon PTREL function and muon PTREL function in the sideband region of MDIF plot. This fit is simultaneously done with the fit on MDIF plot. See also Fig. C-7.

BIBLIOGRAPHY

[1] F. Abe et al. *Phys. Rev. Lett. 74*, page 2626, 1995.

[2] J. Yoh. *Private communication.*

[3] D.H. Perkins. *Introduction to High Energy Physics.* Addison-Wesley, 1987.

[4] Y. Nambu. *Quarks - Frontiers in Elementary Particle Physics.* World Scientific, 1985.

[5] M. Gell-Mann and A. Pais. *Phys. Rev. 97*, page 1387, 1955.

[6] E.E. Landé et al. *Phys. Rev. 103*, page 1901, 1956.

[7] E.D. Commins. *Weak Interactions of Leptons and Quarks.* Cambridge University Press, 1983.

[8] M.V. Purohit. *Frascati Physics Series 1*, 1993.

[9] L.S. Brown et al. *Phys. Rev. D50*, page 1209, 1994.

[10] M.K. Gaillard and B.W. Lee. *Phys. Rev. D10*, page 897, 1974.

[11] L. Wolfenstein. *Phys. Rev. Lett. 51*, page 1945, 1983.

[12] P.D.B. Collins, A.D. Martin and E.J. Squires. *Particle Physics and Cosmology.* John Wiley, 1989.

[13] Buskulic et al. *Phys. Lett. B313*, page 498, 1993.

[14] Fermilab WWW homepage.

[15] F. Abe et al. The CDF Collaboration. The CDF detector : An Overview. *Nucl. Instr. Meth. A271*, page 378, 1988.

[16] D. Amidei et al. A Two Level Fastbus Trigger System for CDF *Nucl. Instr. Meth. A269*, page 51, 1988.

[17] K. Burkett. *CDF Ace Training material.*

[18] R. Kennedy. *CDF Ace Training Material.*

[19] J. Patrick. *CDF Ace Training Material.*

[20] L. Costrell and W.K. Dawson. FASTBUS for Data Acquisition and Control. IEEE Transactions on Nuclear Science NS30, page 2147, 1983.

[21] CDFNOTE 3600.

[22] CDFNOTE 4123.

[23] P.Singh. *Private communication.*

[24] O.Long *Private communication.*